Politecnico di Torino
Grenoble INP-Phelma
EPFL

Master's degree in Micro and Nanotechnologies
for Integrated Systems

Master's Degree Thesis

Design, fabrication and characterization of a magnesium-based Split Ring Resonator for pH and strain detection

Supervisor

Prof. Matteo COCUZZA

Tutors

Prof. Clémentine BOUTRY

Prof. Jie ZHOU

Prof. Yanki ASLAN

Candidate

Francesco STALLONE

September 2022

Abstract

Bone substitution is the second most frequent tissue transplantation worldwide. However some drawbacks induced by the surgical operations may arise. An inflammation of the tissues surrounding the fracture may take place. This increase in the acidity level in the environment may provoke cells death and subsequent patient pain. Moreover, there is a relation between the biomechanics and biological environment. Depending on the stability of the implant, a faster or slower bone healing will occur, with a trade-off on the mechanical properties of the formed bone.

Hence a study on a biocompatible, biodegradable and wireless pH and strain sensor has been performed in this project. A first focus on the biodegradable materials that may be employed as bone substitutes has been discussed. The choice of magnesium as working material was unavoidable due to its mechanical properties closer to the natural bone ones and its bone growth ability thanks to the release of Mg^{2+} ions. Then a focus on the wireless sensing mechanisms and an overview of antenna's properties, have been performed.

The Additive Manufacturing (AM) of a magnesium-4%zinc alloyed Split Ring Resonator (SRR) for pH and strain sensing was performed, making the sample porous and improving its biological and biomechanical properties. Two different pH sensing devices were fabricated. The first defined as "ion resistive" sensor, is based on a double concentric split ring resonator coated by hydroxyapatite (HAp), and laminated. In this way only the inner ring will be in contact with the liquid environment, degrading once a pH below the 5.5 threshold is reached, thanks to HAp. The second, or "ion sensitive" sensor is based on zinc oxide nanoparticles, that will be deposited in the gap or on the metal lines of a split ring resonator. Depending on the pH level, more or less H^+ ions will tend to bind on this layer, varying the resonance frequency of the device. For the strain sensing, instead, a novel interdigitated structure have been designed and fabricated. Here, depending on the strain applied on the device's substrate, a displacement of the structure will be induced, generating a shift in resonance frequency.

The fabricated devices have been studied and analysed through scanning electron microscope (SEM), energy dispersive X-ray analysis (EDX), scanning laser microscopy (SLM), atomic force microscopy (AFM) and X-ray diffraction analysis (XRD) to characterize their surface and material properties. It was possible to detect a shift of the resonance frequency peak of around 2 GHz for the ion resistive pH sensor, and of around 60 to 90 MHz proportional to the H ions for the pH sensitive sensor. Finally, it was also possible to detect a shift of around 0.5 GHz of the resonance frequency once a displacement on the strain device, was applied.

La substitution osseuse est la deuxième transplantation de tissu la plus fréquente dans le monde et ces dernières années les installations de prothèse osseuse ont considérablement augmenté. Vu l'augmentation du taux d'implantation osseuse, certaines complications liées aux opérations chirurgicales ont augmenté. L'une de ces complications est l'inflammation des tissus entourant la fracture. Ici, une augmentation du niveau d'acidité dans l'environnement provoque la mort des cellules et donc une douleur chez le patient. Il existe une relation entre la biomécanique et l'environnement biologique. Une cicatrisation osseuse plus ou moins rapide se produira selon la stabilité de l'implant, avec un compromis sur les propriétés mécaniques de l'os formé.

Par conséquent, une étude sur un capteur de pH et de contrainte qui soit biocompatible, biodégradable et sans fil a été réalisée dans ce projet. Le premier axe d'intèrêt se porte sur les matériaux biodégradables pouvant être employés comme substituts osseux. Le choix du magnésium comme matériau de travail était incontournable pour sa grande similitude vis-à-vis de l'os naturel par ses propriétés mécaniques et sa capacité de croissance osseuse grâce à la libération d'ions Mg2+. Puis, un accent a èté mis sur les mécanismes de détection sans fil et un aperçu des propriétés de l'antenne.

La fabrication additive (AM) d'un Résonateur à Anneau Fendu (Split Ring Resonator - SRR) en alliage magnésium-4% zinc pour la détection du pH et de la contrainte a été réalisée, rendant l'échantillon poreux et améliorant ses propriétés biologiques et biomécaniques. Deux dispositifs de détection de pH différents ont été fabriqués. Le premier défini comme capteur "résistant aux ions" est basé sur un double Résonateur à Anneau Fendu concentrique recouvert d'hydroxyapatite (HAp) et laminé. Avec cette méthode, seulement la couronne intérieure sera en contact avec le milieu liquide, se dégradant grâce à l'HAp dès qu'un pH inférieur au seuil de 5,5 est atteint. Le second capteur, dit "sensible aux ions” ; est à base de nanoparticules d'oxyde de zinc, qui vont se déposer dans l'entrefer ou sur les lignes métalliques d'un Résonateur à Anneau Fendu. Selon le niveau de pH, plus ou moins d'ions H+ auront tendance à se fixer sur cette couche, faisant varier la fréquence de résonance de l'appareil. Pour la détection de déformation une nouvelle structure interdigitée a été conçue et fabriquée. Ici, en fonction de la contrainte appliquée sur le substrat du dispositif, un déplacement de la structure sera induit, générant un décalage de fréquence de résonance.

Les dispositifs fabriqués ont été étudiés et analysés par le Scanning Electron Microscope (SEM), par Energy Dispersion X-ray analysis (EDX), par Scanning Laser Microscope (SLM), Atomic Force Microscopy (AFM) et X-ray Diffraction Analysis (XRD) pour caractériser les propriétés mécaniques et de surface. On a pu détecter un décalage du pic de fréquence de résonance d'environ 2 GHz pour le capteur de pH résistif aux ions, et d'environ 60 à 90 MHz proportionnel aux ions H pour le capteur sensible au pH. Enfin, il a également été possible de détecter un décalage d'environ 0,5 GHz de la fréquence de résonance lors-qu'un déplacement sur le dispositif de contrainte a été appliqué.

Table of Contents

List of Tables

List of Figures

Acronyms

HAp
Hydroxyapatite

AM
Additive Manufacturing

BC
Blade Cut

SRR
Split Ring Resonator

DSRR
Double Split Ring Resonator

RCS
Radar Cross Section

XRD
X-Ray Diffraction analysis

SEM
Scanning Electron Microscopy

EDX
Energy-dispersive X-ray Spectroscopy

AFM
Atomic Force Microscopy

LSM
Laser Scanning Microscopy

NPs
Nanoparticles

Chapter 1

Introduction

This project is based on the design, fabrication and characterization of a wireless, biodegradable and biocompatible pH and strain sensors for in human monitoring. The scope of this device would be sensing of pH and strain variation induced by the degradation of a bone substitute inside the human body.

Right now, most of the bone grafts are based on biocompatible, yet not biodegradable materials, such as Titanium, which does not allow the bone to form back to its original form, but provide good biomechanical properties, allowing most of the patients to have a normal life after the implant positioning. The other types of bone substitutes will be described in this chapter, giving an overview of the several different possibilities available.

The inflammation issue will be then discussed. Once an external object enters inside the human body, or when an injury occurs, an inflammation may take place, induced by the production of lactic acid in the proximity of the wound, reducing the overall pH in the zone. This increase of acidity would provoke several problems for the human tissues, generating a huge amount of pain for the patient, and the need to substitute the implant as soon as possible.

The other and last key point that will be discussed in this chapter are the mechanical factors. There are some parameters, such as the strain, the motion and the stability of the implant, that have to be correctly matched to the normal condition ones. If a too high strain takes place the bone will not have enough time nor strength to grow making impossible the correct formation of it, while if the motion is too little the bone will tend to be weaker and reduce its density due to the lack of stimulus.

1.1 Bone Substitutes

Bone grafting is one of the most frequent tissue transplantations worldwide, second only to blood transfusions, and are being used especially in oncologic surgery, traumatology, revision prosthetic surgery and spine surgery [1]. In recent years, bone defects, implants and prothesis have become more common. Over two million bone substitution procedures take place every year, allowing more patients to live a normal life after an injury.

A synthetic, inorganic, or biologically organic material that can be inserted for the therapy of a bone deficiency is known as a bone substitute. There are several properties that a bone substitute must have to allow a correct bone healing such has osteoinductivity and osteoconductivity. It has to be sterile and biocompatible, causing no irritation, and reasonably priced, [2]. One of the main problem that may take place when a bone substitutes gets implanted into the human body, is the infection of a foreign material, [3]. For this reason the biocompatibility and the asepticity of the implanted bone is one of the most important criteria that have to be taken into account once deciding a bone substitute. As just stated, there are several challenges that arise once working with in-human bone grafting, and some of them will be here described to allow a further understanding of the needed material properties. Here there will be a description of the main parameters as defined by Albrektsson et al. in [4] and by Hughes et al in [5].

- **Biocompatibility** is the property of a material of being compatible with living matter and tissues. It doesn't have to produce toxic or unwanted response once exposed to biological fluids or tissues. It can also be defined as the ability of an implant to function $in-vivo$ without producing toxic by-products.

- **Biomechanical stability**, it is a material property which relies on its intrinsic Young Modulus and density. The employed material have to match bones' mechanical properties to withstand the human body weight without breaking and without inducing external stress.

- **Osteoinduction** consists in the stimulation of immature cells to develop into pre-osteoblasts, which regularly occurs in fracture healing or bone implants. The injury releases local biochemical and biophysical messengers that guide those cells to work properly. It also refers to the stimulation of osteogenesis through the recruitment of osteogenic cells on the injury site.

- **Osteoconduction** can be defined as the process by which the bone is directed to grow conformal to the biomaterial scaffold surface. It not only depends on the biomaterial employed but also on the previous osteoinduction. A osteoconductive material allows the bone to grow over its surface or through its pores. There is a difference on the amount of bone that grows on similar materials, so the choice of a good biocompatible material is mandatory for the implants.

- **Osteointegration** depends on the two previous phenomena described above. Allows the implant to live longer through the incorporation of a material that it is firmly attached to the surrounding bones. It is a direct anchorage of an implant by the formation of bony tissue around it without the growth of fibrous tissue at the bone–implant interface.

There are other parameters that may be important to have for a bone substitute, that may help the healing process. These are not mandatory parameters, but have been studied and demonstrated that they may affect a faster or a correct bone growth by Hannink et al in [6].

- **Biodegradability**, is a key parameter for a bone substitute only when the resorption rate is similar to the bone formation one. If a material tends to degrade too fast, first it will increase the local ion concentration, creating a non good environment for cell proliferation, then it will not be stiff enough to maintain the two bony sides tied together. Bioresorbability, induces also the possibility to not operate a second time to remove the implant once the bone heals completely, reducing the inferred pain to the patient.

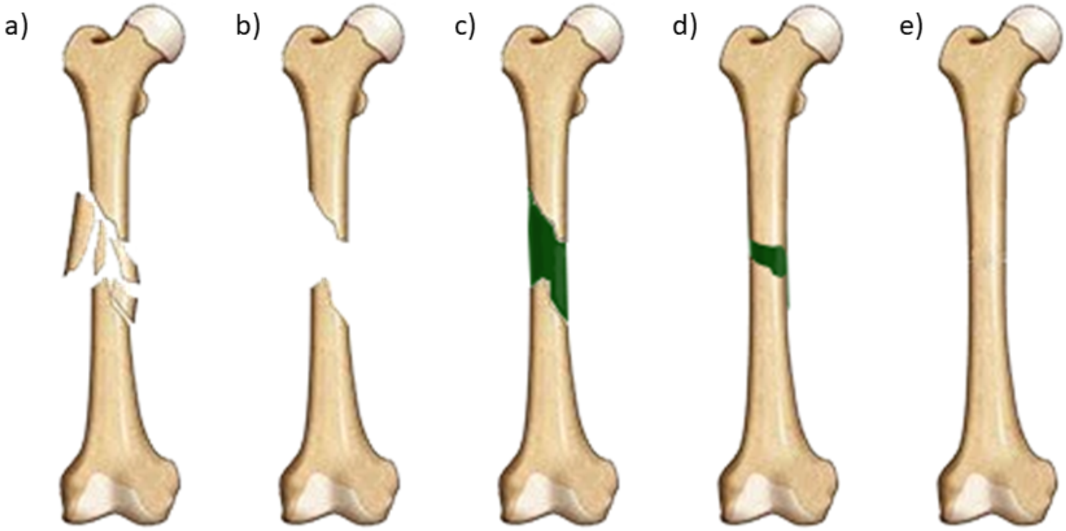

Figure 1.1: Bone healing process with a biodegradable implant.

- **Porosity** is important since it allow migration and proliferation of osteoblasts and mesenchymal cells. A porous surface increases the mechanical interlocking, the adhesion, between the implant and the natural bone, improving the mechanical stability at the interface, [7]. Small pores results in endochondral ossification, where a cartilaginous bone starts forming from cartilage and is more porous, while larger pores size increase the direct osteogenesis, oxygenation and vascularization [6], resulting in intramembranous ossification, without the formation of cartilage resulting in a stiffer bone [8].

Bone grafts, ceramics, polymers, and metals are the main types of bone substitutes that have been used up to this point. In this chapter there will be a focus on each one of them, focusing on the properties of each method, compared also with the natural human bone.

In bone grafts there are three different subsets of bones that can be considered for the scope which will be described in the following, which are based on the use of bones either from the same patient, or from another human donor, or from another species, [9].

- **Autografts**, autologous bone grafting, relies on the employment of bones obtained from the same patient which needs the graft. The bone employed gets harvested from non-essential bone sides, like ribs, and occurs only when there is a lower degree fracture. The advantage of employing an autogenous graft is its osteoinductivity and osteoconductivivty, it also houses growth factors and osteogenic cells with no associated infective risks. The drawback relies on the extrapolation of the autogenous bone, its post-operation complications may cause infection.

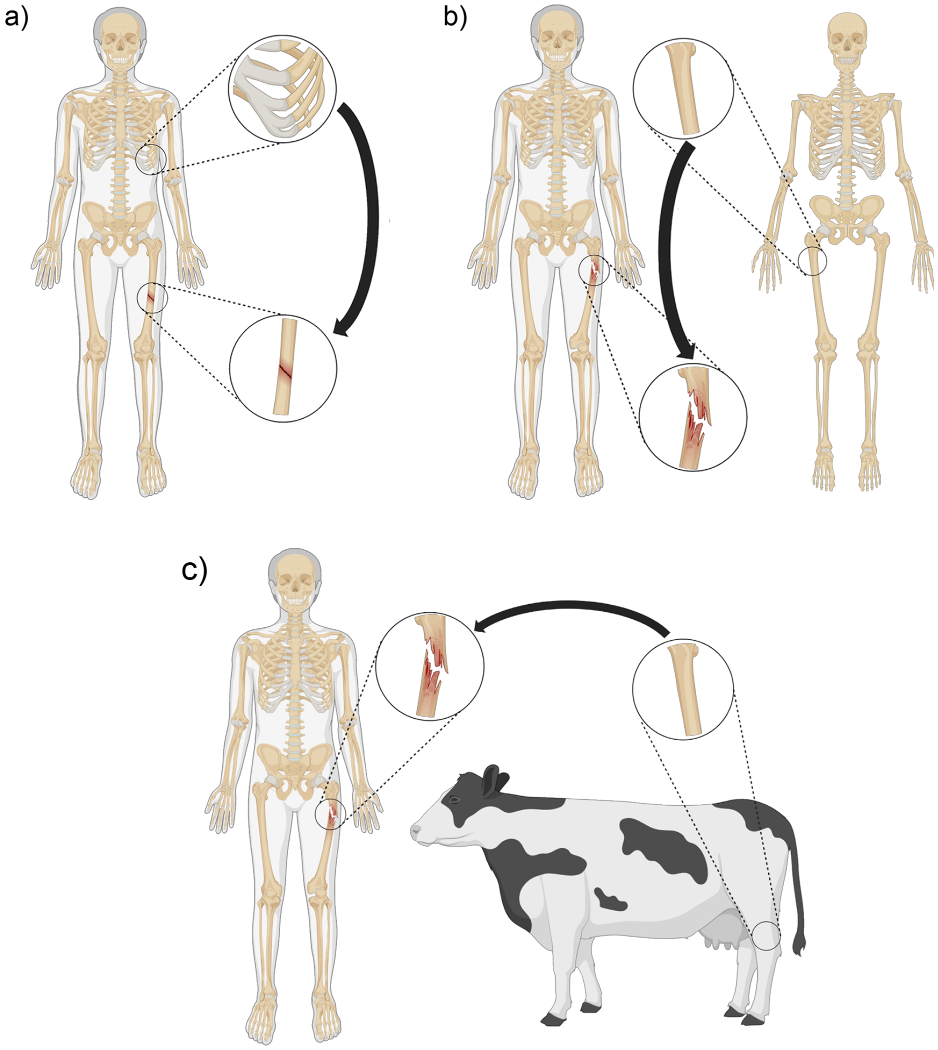

Figure 1.2: The possible type of bone grafting. In *a)* it is reported the autograft, in *b)* it is reported an allograft schematics, while in *c)* there is a schematic of a bovine xenograft.

- **Allografts**, relies on the employment of bones collected from either living or non living human donors, processed by a bone tissue bank. The advantage is that the used grafting bone is extracted from another human being, which reduced the risk of complications on the same patient, while the bone is still osteoconductive. The drawback relies on its little osteoinductivity, the need of sterilization with gamma radiations, effecting its mechanical properties and deactivation of some properties contained in human bones.

- **Xenografts**, rely on the employment of bone substitutes not deriving from human sources, but from other species such as bovine or porcine, which will be freeze dried or deproteinized. They have given acceptable results in dentistry but scarce is orthopaedics.

Then there are the ceramics which are based on several different material that can be employed for the scope of bone substituting. The focus here will be on Calcium based substitutes, and more specifically on Hydroxyapatite and Tricalcium Phosphate, [9]. Usually a $60\% - 40\%$ of respectively HAP and TCP is employed to have a trade-off between degradation and mechanical properties. Further, a composite of HAp with collagen may take place enhancing osteogenesis, osteoinductive and biomimetic capabilities lowering the infection risks, [10]. Collagen ductility boosts HAp's weak fracture toughness, while CaP offers collagen additional stability and impact resistance, [11].

- **HAp**, or hydroxyapatite, $Ca_{10}[(PO_4)_6(OH_2)]$ is the crystalline form of TCP. Once implanted, it degrades slowly and pH dependently, remaining an inert substance inside the human body. Although it is the major constituent of bone and teeth and has strong mechanical qualities, its properties cannot be compared to actual human bone.
- **TCP**, or tricalcium phosphate, is more porous and degrades faster than the HAp, within 6 weeks from its implantation, it has high dissolution rate that accelerates material resorption but poor mechanical properties, especially due to its porosity.

	HAp Bulk	HAp 50% Por.	TCP Bulk	TCP 50% Por.
$E\ (GPa)$	8.4-10.13	1.201-1.271	18.93-23.23	1.528-1.613
$\sigma\ (MPa)$	56.6-85.4	8.75-9.91	275-361	12.4-13.3
$K_{lc}\ (Jcm^{-3})$	0.2624-0.4853	0.0383-0.0462	1.915-2.865	0.0734-0.0816

Table 1.1: Mehcanical properties comparison between HAp and TCP, from [12]

In Table 1.1, there are reported the mechanical properties of HAp and TCP, taken from [12]. The parameter shown are the Young's modulus E in GPa, the compressive yield strength σ in MPa and the fracture toughness K_{lc} expressed in Jcm^{-3}.

Metals are usually employed as bone substitutes due to their fracture toughness and mechanical strength. The most common metals approved by FDA as bone substitutes are Titanium, stainless steel and Cobalt-Chromium alloys which may release some toxic metallic ions during corrosion inducing a chronic local inflammation in the implant site, [13]. They are tough materials and their mechanical properties, in Table 1.2, are not close to the natural bone ones, [14]. The final issue is that a second surgical operation have to taken into account to remove these metals once the tissue has healed enough. Some of these drawbacks can be compensated by employing Magnesium, which is biocompatible, has mechanical properties similar to the natural human bone and is biodegradable allowing the resorption by the body.

	Natural Bone	Magnesium	Ti alloy	Co-Cr alloy	Stainless Steel
$\rho\ (g/cm^3)$	1.8-2.1	1.74-2.0	4.4-4.5	8.3-9.2	7.9-8.1
$E\ (GPa)$	3-20	41-45	110-117	230	189-205
$\sigma\ (MPa)$	130-180	65-100	758-1117	450-1000	170-310
$K_{lc}\ (MPam^{1/2})$	3-6	15-40	55-115	N/A	50-200

Table 1.2: Mehcanical properties of different metal implants and natural bone, [14].

1.2 Inflammations

There will be given an overview on the acidity level that can be induced once an inflammation takes place, and there will be shown the causes that may induce a pH drop once an external implant gets inserted into the human body. The term inflammation refers to a tissue's reaction to a detrimental stimulus, which removes the hazardous event and initiates the healing process.

Two different kinds of inflammations may take place, the acute and the chronic, which will generate different feedback from the healing process of the bone, described by [15]. In the chronic inflammation case, there will be an over production of pro-inflammatory macrophages even during the healing process, increasing even further the acidity level of the overall environment. There will be the need of several more months for the bone healing inducing extreme pain, and cells death due to a huge pH drop.

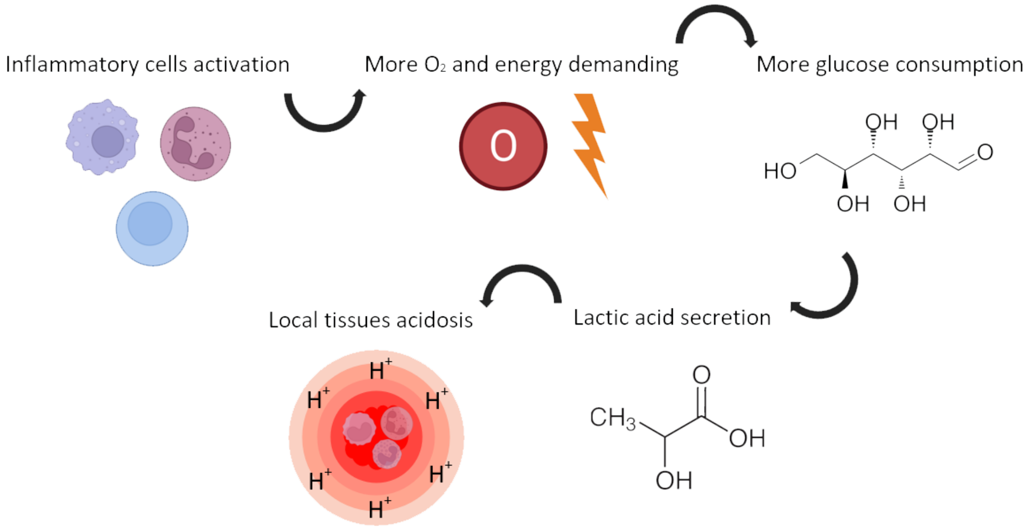

Figure 1.3: The generic steps that occur until the inflammation takes place, from [16].

The main cause that induces an increase of the acidity level is the extracellular acidosis, which is induced by an inflammatory cell, such as T-cells, B-cells, mast cells macrophages, and neutrophils. The relationship between inflammation and pH reduction, is also shown in Figure 1.3, where due to the infiltration and activation of inflammatory cells in the tissues, an increase in of energy and oxygen need takes place, speeding up the breakdown of glucose through glycolysis, and increasing the release of lactic acid. Due to the inflammation pH levels as low as 5 can appear, making the environment extremely acid, inducing serious health hazards, some of the causes also shown by [16], may be depending on cancerous cells, arthritis, or asthma. Some other factors that can lead to a pH drop, as described by Diaz et al. in [17], may include tissue hypoxia, where blood vessels are damaged as a result of leukocyte activity, leading to an accumulation of lactic acid, lowering the pH; an accumulation of short-chain fatty acids induced by the proliferation of bacteria introduced by the external environment, reducing the pH level down to 4. The last cited case may occur one implanting a bone substitute.

It is also very important to define the two different bone healing processes that can take place once a fracture occurs: the direct, or primary healing and the indirect, or secondary healing. Depending on which of the fracture that takes place, a different healing process will get provoked. Bone union depends on the correct delivery of growth factors and nutrients on the fracture site, as also reported by [5]. Some of the most important growth factors are Platelet Derived Growth Factor, or *PDGF*, which recruits inflammatory and progenitors' cells; Bone Morphogenic Proteins, *BMP*, have the role of enhancing the osteoblasts differentiations; and *FGF*, the Fibroblast Growth Factor, which stimulates the proliferation of mesenchymal cells allowing the regrowth of the vascular system and tissues on the injury site.

The **primary bone healing** is he most uncommon process for fracture healing and consists of no displacement of bone fragments in the surrounding of the fracture, the overall bone remains fixed and stable. It has no inflammatory responses and hence a slow healing process, few months to a year for full healing. The **indirect bone healing** is the most common. It occurs on most fractures, usually characterized of six main parts as reported in [18], which are the fracture, the hematoma, the inflammation, the fibrovascular, the bone formation and the remodelling part. Each one of them will be described in the following, giving an overview of what happens once a fracture takes place until the complete bone healing.

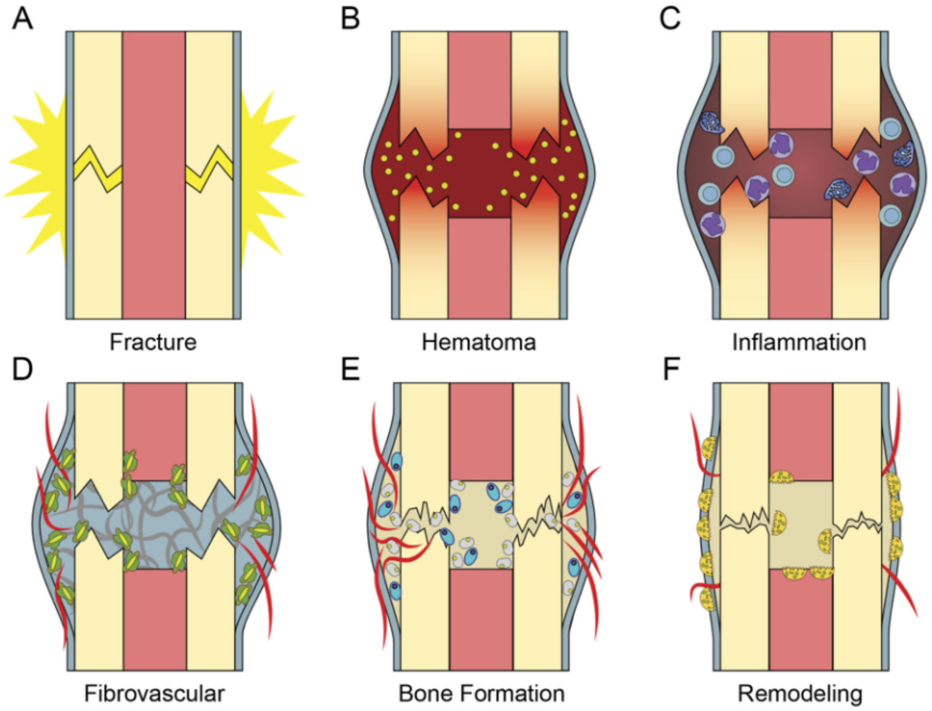

Figure 1.4: The six steps that occurs from the fracture to the bone healing, [18].

In the following a focus on the secondary bone healing will be taken in consideration. The first temporal event that occurs is the *Fracture*, which is characterized by the breaking of a bone. A lack of mechanical stability and a reduction in tissue oxygenation and nutrient delivery result from the destruction of the vascular supply and bone structure in this situation. The disruption of the periosteal cortical and medullary vascular supply would result into an extreme acidosis and cellular necrosis. Already at this stage, some bioactive substances, primarily inflammatory cells, and cytokines, are released at the site of the damage, aiding the normal repair of the bone.

Few minutes after the fracture, a *Hematoma* forms where a blood clot of fibrin forms, achieving haemostasis. The clot is crucial because repair cannot proceed any further without fibrinolysis, which would otherwise result in poor bone healing. Inflammatory cells like neutrophils and macrophages are then gathered by the clot's production of cytokines, which prompts them to travel towards the site of the injury where they primarily function to eliminate the injured and dead tissues. The hematoma phase will allow the connections of the broken bones ends, creating a sort of template that will help the formation of the callus.

Here the *Inflammation* phase will arise, which as stated before may be acute or chronic.

- In **acute inflammation**, microphages, dendritic cells, and other cells will recognize encroaching pathogens and damage-related by-products, producing pro-inflammatory mediators including chemokines, cytokines, and growth factors to enable the infiltration of polymorphonuclear neutrophils, or *PMNs*, that will destroy these invaders. Pro-inflammatory cytokines will now polarize macrophages into the M1 phenotype, which will defend and increase the inflammatory response while drawing in more immune cells.
- In **chronic inflammation** fibrosis, inflammation and repair occurs concurrently, as every cell is present at the damage location at once. Pro-inflammatory cytokines will continue to be produced, polarizing macrophages into the pro-inflammatory M1 phenotype rather than the anti-inflammatory M2 ones, the latter would promote collagen deposition, the restoration of tissue homeostasis and most importantly, healing of the tissues, [15].

Following the *Fibrovascular* phase occurs, where vascular remodelling and gathering of mesenchymal stem cells from the bone marrow, or *MSCs*, will take place. The MSCs will eventually differentiate into osteoblasts, fibroblasts and chondrocytes which will regenerate the fractured bone. During this phase, two distinct processes arise: angiogenesis, new blood vessels are produced from the already existing vasculature, and vasculogenesis, new blood vessels are formed from endothelial progenitor cells, or *EPCs*, within the callus—will be used to construct the network.

Bone formation can now occur, passing by the *Callus* phase. Endochondral ossification generates soft callus first and then hard callus, and intramembranous ossification, generating hard callous directly, are the two types of processes that contribute to callus formation. Either a two-step healing process or immediate bone regeneration will occur depending on whether the *MSCs* differentiate into osteoblasts or chondrocytes. After the calcification of the cartilage the bone formation can be considered finished.

Finally, the last step that takes place is the bone *Remodelling*, where the bone gets restored to its initial structure and mechanical properties. Here, the woven bone, or provisional bone, is replaced by the lamellar bone, which has superior mechanical characteristics than the first. Osteoclasts, which are differentiated by bone marrow macrophages, will aid in the process.

1.3 Mechanical Factors

There are several mechanical factors that have to be taken in consideration while working on the bone union, which are the pressure, the stability, the strain, and the speed. If a too high strain or displacement takes place an inhibition of the bone bridging on the fracture will take place, increasing the time of healing or stopping the bone union. If an absolute fixation occurs, there will be a bridging callus forming, allowing a great bone union, but it will reduce the mechanical properties of the formed bone.

It is important to state that there is a compromise between biological environment and mechanical stability. Hence, depending on the type of fracture that occurs and the goal that wants to be reached, a more or less stabilized fixation will take place. Halvachizadeh et al in [19], have shown how depending on the aimed type of bone healing, primary or secondary bone union, two different implant kind may be employed, reaching a relative or an absolute stability, respectively. Relative stability, allows a little movement of the bone once a force gets applied, creating an indirect bone healing. Usually external fixators are employed since it is possible to modify their flexibility in order to achieve more or less implant stability. While absolute stability, creates a condition of non strain, generating a direct bone healing.

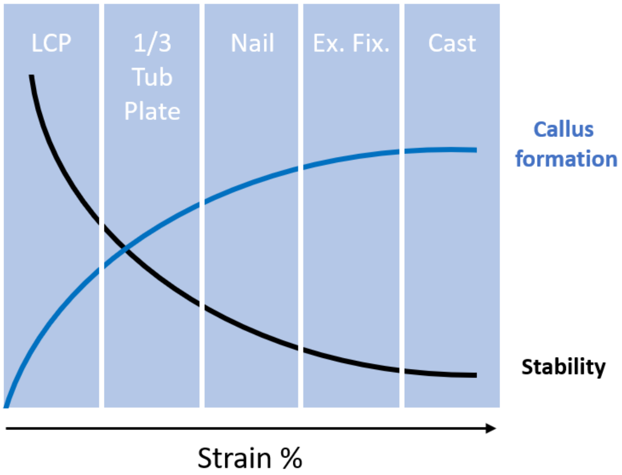

Figure 1.5: Callus formation and bone stability, hence bridging, variation over applied strain and fixation method. LCP, lateral compression plate; Tub Plate, tubular plate; Ex. Fix., external fixator

Once an indirect fracture healing takes place, an acceleration of bone healing is induced by the stimulation of callus formation by interfragmentary movement. Hente et al in [20], have demonstrated how cyclic compressive displacements tends to enhance the callus formation, reducing the bone bridging on a sheep tibial osteotomy model. Perren's theory, [19], shows the difference in strain sensed by the bone cells around the fracture depending on the calcification state of the bone. Mechanical stimuli are needed to form the hard callus and to allow the bone bridging it has to be maintained little. In Figure 1.5 is reported the variation of bone stability and callus formation depending on the applied strain, one fixation method over the others have to be chosen based on the fracture gravity.

Chapter 2

State of the Art

The project's objective is the fabrication of a wireless sensor that has to be inserted into human body, hence a state of the art should be performed on several different sections.

First, a metallic, biocompatible and biodegradable materials material is needed, therefore a study on biodegradable materials will be needed, allowing then the choice of the best suitable material for bone implants. The sensing mechanisms rely on either a pH resistive or a pH sensitive materials. Depending on these two, a different sensing mechanism will be employed for the H ions concentration analysis. Finally, a biodegradable polymer for the sample may be needed, to coat the structures and/or to function as a substrate. Since the strain has to be evaluated an elastomer will be chosen over a stiffer material.

The target device should allow either the pH sensing or the strain sensing once $in - vivo$, hence a study on the sensing mechanisms available in literature will be performed. A specific focus on the currently available biodegradable and wireless sensors will be reported.

Finally since a wireless sensor will be fabricated, a reminder of some of the most important antenna concepts will be mandatory, to ease the understanding of the obtained results. Further, resonating devices will be taken into account, describing their physics, since the sensor will be based on them.

2.1 Materials

In this chapter there will be a discussion concerning the different employable materials for the project goal with a specific focus on those materials that respect all the parameters to allow a fast and correct bone healing. First, there will be shown the several biodegradable materials that can be employed with an emphasis on the biodegradable metals that are indeed needed to have a wireless sensor. Then there will be shown the material chosen for the project, showing the several challenges for some of them and describing the methods to make them more suitable for the final goal.

2.1.1 Biodegradable Materials

An overview of all the biodegradable materials that are already present inside the human body will be taken into account. A focus on their in human percentages will be shown, and a comparison between these materials will be performed, to allow a correct selection. In literature there have been several studies concerning these biodegradable materials that have lead to very interesting results. Tsang et al in [21], have managed to fabricate the first fully biodegradable battery based on magnesium and iron, opening the idea of fully functioning and resorbable in human devices for energy harvesting or sensing shown in Figure 2.1 a). Hwang in Rogers' group, instead, have shown in [22] that is possible to fabricate biocompatible and biodegradable Silicon based CMOS devices shown in Figure 2.1 b), paving the way for fully biodegradable integrated systems.

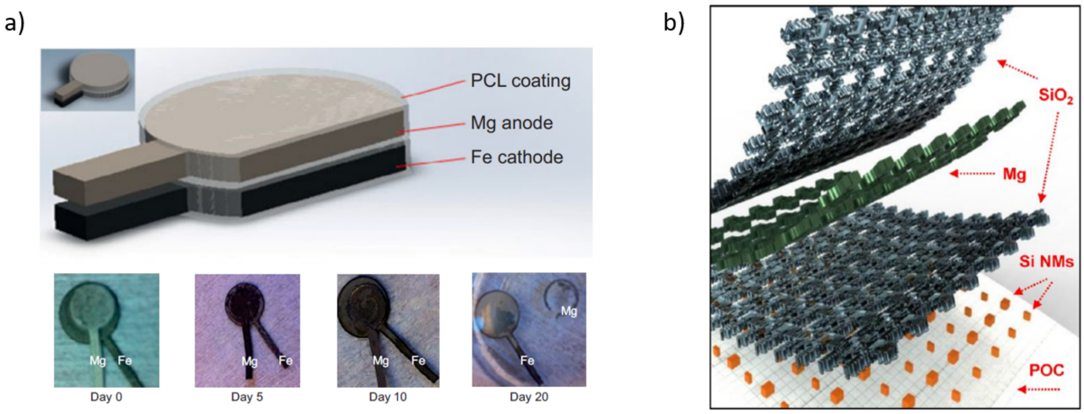

Figure 2.1: In *a)* the biodegradable Mg/Fe battery fabricated by [21]; in *b)* the biodegradable CMOS from [22].

In Figure 2.2, it is shown the list of the several biodegradable materials that are already present inside the human body, making them the most suitable materials for in-human applications. It is also reported the concentration of each one of them, allowing an additional focus on which one of these materials may be fitting best. Obviously this parameter describes the material concentration on the overall human body, a too high local concentration of one of these material would result in an toxic environment.

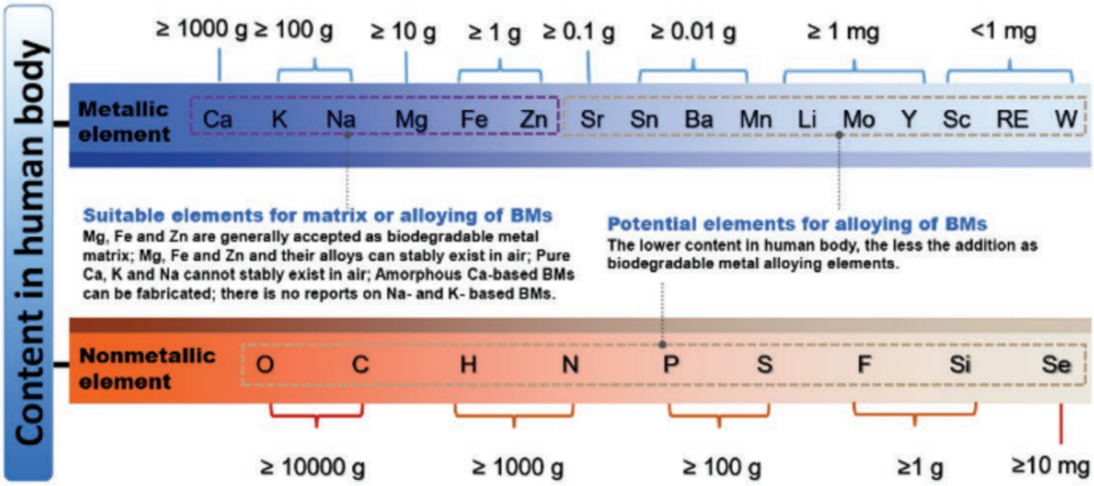

Figure 2.2: List of the biodegradable materials already present in the human body, [23].

From the above shown materials a focus on the most suited metals for the project scope will be taken into account, showing advantages and disadvantages of them.

One of the most present metals in the human body is Magnesium. It has an excellent biocompatibility and a low density and elastic modulus, closer to the natural bone ones. Once inserted in the human body the magnesium based structures will start to degrade due to the presence of Cl^- in the physiological environment. This degradation will induce the releasing of either Mg^{2+} and OH^- ions, inducing an increase of the local pH. The Mg^{2+} ions that will be released are the corrosion product of Mg implants will enhance the bone formation. Hung et al in [24] have shown that these ions will induce an osteogenic effect in the bone marrow, activating the Wnt pathway causing BMSCs to differentiate into the osteoblast lineage.

An issue related to pure magnesium it the formation of hydrogen gas following the relation $Mg + 2H_2O \rightarrow Mg(OH)_2 + H_2$. Around 1l of gas will be formed by 1g of magnesium, [25], which will not be able to leave the human body, creating gas cavities. To reduce its corrosion rate, the gas release and the local pH increase, but also To increase its strength, magnesium is usually alloyed with other biodegradable metals.

Iron has high mechanical properties similar to stainless steel, making it a suitable material for tough applications. The main drawbacks for this material are its ferromagnetic property and slow in vivo dissolution rate. It has been shown that vast quantities of Fe implant were still present 12 months following surgery, and the reactions were comparable to those of permanent bone substitutes, [26]. Ferromagnetism impacts some imaging tools which would limit the monitoring, further, for the project scope, this would limit the electromagnetic properties of the sensing device. By modifying the fabrication process and by alloying it with other biodegradable metals it is possible to accelerate its degradation rate, and reduce a bit the ferromagnetic property of the bulk material, without fully optimizing either of these.

For what concerns Zinc, it shows a good biocompatibility and corrosion rate, lower than magnesium, but really poor mechanical properties, making it not the best bone substitute, [27]. Once alloyed some of the above mentioned obstacles can be compensated, but yet its overall properties are worse than the previous materials.

Tungsten and Molybdenum have also been recently employed for the fabrication of active or passive biodegradable electronic components for biomedical in human applications. Fernandes et al in [28] have described some of the technologies which could pave the way to fully transient biodegradable implantable electronic system with the above mentioned biodegradable metals. But their mechanical properties are still too different from the natural bones ones.

Here, a table containing the mechanical parameters of the cited element will be described, allowing a comparison of the biodegradable materials properties with the natural bone.

	Natural Bone	Mg	Fe	Zn	W	Mo
ρ (g/cm^3)	1.8-2.1	1.74-2.0	7.86-7.88	7.13-7.15	19.25-19.35	10.1-10.3
E (GPa)	3-20	41-45	204-212	90-110	340-405	315-343
σ (MPa)	130-180	65-100	230-345	90-200	1670-3900	380-2100
K_{lc} $(MPam^{1/2})$	3-6	15-40	120-150	35-120	120-150	20-40

Table 2.1: Mehcanical properties of various biodegradable metals, [14] [23] [29].

2.1.2 Material Selection

From the list of biodegradable materials which are also biocompatible reported in Chapter 2.1.1, the choice of the employed materials will here be studied, depending on the material properties. The material selection will rely on metals, polymeric substrate, ion resistive and ion sensitive materials.

- **Metal**

As reported in the previous chapter there are several metals that are already present in the human body and could be employed as the pH and strain sensor material. From the above mentioned list, in Table 2.1 there are the metals parameters with respect to the natural bone. The most suitable material for the project goal would be magnesium. But there are several drawbacks concerning this material, in this sub-chapter some of them will be discussed and partially compensated. As previously mentioned in Chapter 1.1 there are several parameters that have to be taken into account to have a good bone substitute material, it has to be biocompatible, biodegradable and porous. Magnesium is for sure a biocompatible and biodegradable material, as discussed in previous chapter, but in bulk conditions its degradation rate is too fast leading to a too high ion release.

If coated by a protective layer it has been shown that pure magnesium would degrade much slower, allowing it to be fully biocompatible and non toxic once employed as bone substitute. One of the most common coating layers is Hydroxyapatite, which is a calcium-phosphate based ceramic with great adhesion on magnesium, described in the following section. Dong et al in [30]. have shown that an Fluoride and subsequent CaP coating on a bare Mg scaffold would improve its corrosion resistance and its biocompatibility, increasing cell attachment.

Further, if alloyed with another biodegradable metal, it shows lower degradation rate. In Figure 2.3 are reported three graphs depicting the variation of mechanical properties of the magnesium alloy depending on the alloying element weight percentage. Zheng et al in [26] have shown that one of the most suited alloying would be Mg with a 4 wt% of Zn due to the extremely high elongation and tensile strength with a really low degradation rate.

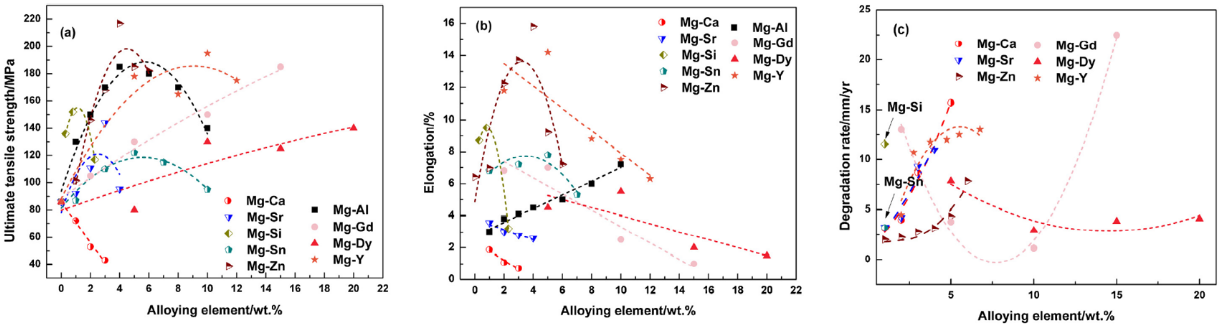

Figure 2.3: Tensile Strength, Elongation and Degradation Rate of magnesium for varying alloying wt %, [26].

Another optimization may be regarding the material porosity since a porous biodegradable implant would ease transport of nutrients and metabolic waste. By manufacturing the magnesium scaffold with some specific techniques, it may be possible to make Mg structurally porous. The most common techniques for this scope are: selective laser melting, SLM, powder bed inkjet 3D printing, fused filament fabrication or solvent cast 3D printing, SC-3DP. Most of these techniques rely on the localized heating of magnesium or magnesium powder to additively manufacture the scaffold, which may be extremely risky due to the low melting point, high vapor pressure and high reflectance of magnesium, which may lead to explosions.

One of the safest way of fabricating this scaffolds is SC-3DP, which consists on the extrusion of a paste made by a polymer and metallic particles, that would later be heated up to allow the polymer removal and sintering of the particles. The advantages of this technique rely on relative low temperature manufacturing and the easy modification of component percentage of the "ink", allowing the fabrication of magnesium alloys adjusting the binder to particles concentration. Dong et al in [30] and [31], was able to fabricate porous scaffolds with pure magnesium and magnesium zinc alloy through the SC-3DP method.

- **Polymeric Substrate**

For what concerns polymers, in recent years there has been a lot of focus on the synthesis of a biocompatible, biodegradable and cost effective polymer for environmental concerns since petroleum based plastics are polluting the environment, [32], but also for biomedical applications, such as tissue engineering or bio-implants, [33].

	PLA	PCL	PGA	PGS	PGSA	POMaC
ρ (g/cm^3)	1.24	1.13	1.61	Low	Low	1.13
E (GPa)	2.5	0.35	6.5	2.4 e^{-4}	3.1 e^{-4}	1.2 e^{-4}
σ (MPa)	50	30	75	0.09	0.12	0.326

Table 2.2: Mehcanical properties of various biodegradable polymers, [34], [35], [36].

In table 2.2 there are shown the several biodegradable polymers that have been synthesized in recent years. Since different methods may be employed to fabricate the final scaffold, the parameters describing these material may vary. In table 2.2, a focus on the 3D printable, for PGS and PGSA, and UV curable, for POMaC, materials have been taken into account. The project goal is the employment of this biopolymer as substrate for the strain sensing device, and as lamination layer, a focus on the elastomeric ones will be taken into account. POMaC has been the chosen material due to its really low young's modulus.

Tran et al in [36], have first synthesize poly(octamethylenemaleate (anhydride) citrate) or POMaC. It is a biodegradable elastomer with tunable properties with two different crosslinking mechanisms, UV polymerization and post-polycondensation with temperature treatment. It is based on non-toxic monomers, has a simple synthesis and its degradable and mechanical properties can be controlled. The UV polymerization technique is the one chosen, and will be described in Chapter 4.6.

- **Ion Resistive Materials**

Ion resistive is a material that starts to degrade only once a certain pH or ion concentration threshold gets reached in the surrounding environment. Two of them will be here described, poly(methacrylic anhydride), or $PMAH$, and Hydroxyapatite, or HAp.

Shi et al in [37], have shown PMAH as a biodegradable polymer coating for drug delivery. It is deposited through initiated chemical vapor deposition,*iCVD*, which avoids the use of solvents, the use of high-energy plasma or temperature that may affect the chemical composition of drugs. The degradation rate of the PMAH relies on the concentration of H^+ ions in the aqueous environment. The higher the pH value the faster the material will degrade releasing more drugs. As shown in Chapter 1.2, the target pH is on the order of 4 to 5, making it fully degrade after 9 to 13 hours.

Hydroxyapatite is a ceramic already cited in Chapter 2.1, is the most present inorganic component of bones. Due to its high biocompatibility and bioactivity is able to accelerate bone growth on implants, hence it is usually employed as a coating materials for bone substitutes, [38] [39], but has bad mechanical properties, [12]. To coat the implant several methods may be employed like the electrochemical deposition and the sol-gel or plasma spraying. Hydroxyapatite can be employed as pH sensitive layer, since it's dissolution is affected by the H^+ ions concentration and its further degradation will take place only once the acidic level of the environment reaches a value of 5.5 pH or lower. The lower the pH level, the higher the H^+ ion concentration the faster the dissolution of the material.

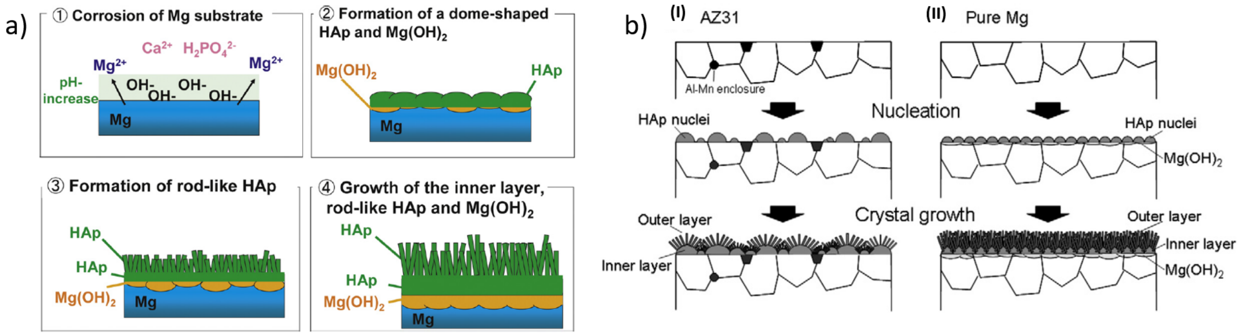

Figure 2.4: In *a)* the HAp formation on pure Mg from [40]; in *b)* HAp formation on a Mg alloy from [41].

This material has a great adhesion on top of magnesium, which as previously reported is the chosen metal for the project goal. In fact, some of the deposition methods have been optimized to allow an HAp coating on top of the biodegradable magnesium such as the hydrothermal method described by Hiromoto in [41] and by Tomozawa in [40]. In Figure 2.4, it is reported the steps that occur for the formation of the HAp crystals on top of the magnesium substrate, and the difference between the pure magnesium and its alloy.

Once the Mg sample gets immersed into water, the reaction reported in Equation2.1 takes place due to the corrosion of the magnesium substrate. The pH increases starting a rapid nucleation of HAp with simultaneous formation of $Mg(OH)_2$ on the Mg surface.

$$Mg \rightarrow Mg_2^+ + 2e^- \quad ; \quad 2H_2O + 2e^- \rightarrow 2OH^- + H_2 \tag{2.1}$$

The continuous supply of Ca_2^+ ions and the difference in solubility will promote the nucleation rather than the $Mg(OH)_2$ formation. This nucleation process will start to create some clusters, allowing the creation of some dome-shaped Hap agglomeration as shown in Figure 2.4 a-2. Once the substrate is fully coated, the degradation of Mg will slow down, hence the pH variation along the surface is stopped. Only now a rod-like hydroxyapatite will start forming from the domes, which orientation is usually normal to the dome surface.

As shown in Figure 2.4 b), the rod-like Hap crystals will tend to interdigitate more if the substrate is a magnesium alloy, due to the formation of domes only on Mg, allowing a better adhesion on top of it, reducing the chance of detaching once immersed into liquids.

- **Ion Sensitive Materials**

The ion sensitive materials will be here discussed. For every potentiometric ionic evaluation an ion-selective membrane is essential for the sensing, it is usually based on metal oxides, polycristalline materials, porous films or highly plasticized polymers, [42]. From the several materials that can be employed as sensing material a focus on the biocompatible and/or biodegradable ones will be shown. There are two main groups of ion selective electrodes based on fixed and mobile ion-exchange sites, [43]. In the first group solid membranes are used such as glass, single crystalline or poly-crystalline materials, a polymer matrix with poly-crystalline materials, or metal oxides. While for the second group liquid membranes may be employed, like PVC membranes containing an active plasticized substance.

The most employed one for pH detection is glass, since it consists of fixed silcate groups $-OSiO_2^- Na^+$, [44]. The sodium ions exchange with the solvated protons in water, making the surface "hydrated". The H^+ ions are free to exchange with sodium ions in the body of the glass, the activity of these ions differs between the hydrate surface and the bulk solution. This difference generates a detectable potential difference between the membrane's surface and the solution. In pH sensitive FETs the materials that are usually employed are silicon based, like SiO_2, Si_3N_4, or metal oxides such as Al_2O_3 and Ta_2O_5. The mechanism that allows the surface charge of oxides is described by the site binding model. Here the SiO_2 case is taken into account, Figure 2.5, where the equilibrium between the Si-OH of the surface and the H^+ ions in the solution is reached. The hydroxyl groups coating the oxide surface accept or give a proton behaving in an amphoteric way.

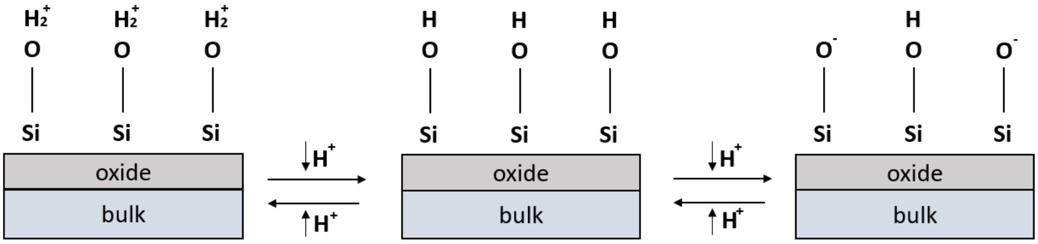

Figure 2.5: Site Binding Model

As metal oxide the one chose was Zinc Oxide due to its high biodegradability and biocompatibility once scaled down in dimensions. Kielbik et al. in [45] have demonstrated the biocompatibility and degradability of ZnO nanoparticles crystallized through the hydrothermal method into live mice tissues. It is also shown that in mice muscle and bones, the Zinc level have not increased. In [46], the same group proved that it is also one of the most promising materials for drug delivery, due to its safety and low toxicity. Zinc Oxide have also been used as an ion sensitive material for pH detection by Li et al. in [47], where an Extended Gate Field Effect Transistor, *EG-FET*, have been fabricated. The device have been characterized and a huge shift in drain current occurs depending on the pH level.

2.2 Sensing Mechanism

In this chapter a discussion about the state of the art of the sensing mechanisms for pH and strain sensor will take place. First a focus on the pH sensors available in literature will be taken in consideration, with a specific focus on the pH sensitive and resistive materials as sensing mechanism, then the several kind of strain sensors will be examined, with a specific emphasis on the wireless and planar ones.

2.2.1 pH Sensing

The pH, or potential of Hydrogen, allows the measure of the acidity, neutrality, or basicity of an aqueous solution depending on the hydrogen ions concentration in the environment. It can be defined with a scale ranging from *0* to *14*, generating three subsets in the following order, acid, neutral and basic. In the following figure, 2.6, it is shown the general scale with an example of solution having a specific pH level dependant on the H^+ concentration.

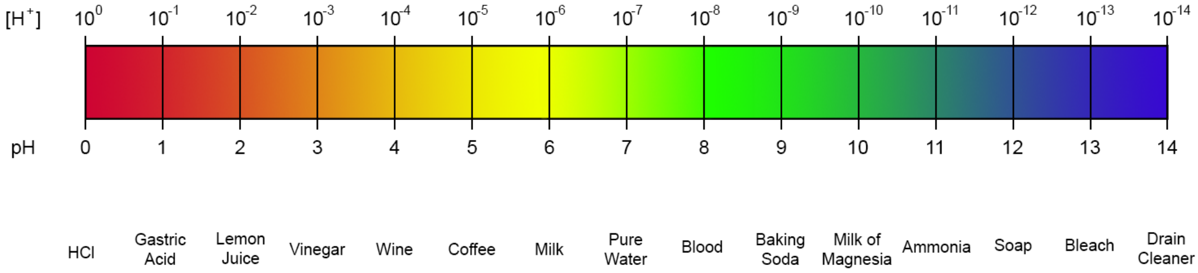

Figure 2.6: The pH bar defining the acidity levels of the solution, in relation to the H^+ concentration.

The pH sensing is really important once taking in consideration bone substitution, as described in Chapter 1.2, since there is a relation between the pH level of the environment and the inflammation state or the bacteriologic infection that may take place during surgery. For this reason, the determination and the constant monitoring of the pH level may allow the prevention of the implant rejection, the pain reduction of the patient and the correct growth of the new bone, while the substitute implant biodegrades.

The pH relies on the concentration of Hydrogen ions inside the solution, which can also be defined as the hydrogen ion activity a_{H^+}.It is possible to define the PH as the logarithm of the reciprocal of a_{H^+}:

$$pH = -\log_{10}(a_{H^+}) = \log_{10}\left(\frac{1}{a_{H^+}}\right) \tag{2.2}$$

The more the H^+ ions, the lower will be the pH level, acid; dually for OH^-, the higher its concentration the higher will be the pH level, making the environment or the solution basic. In literature there are several kinds of pH sensors used to define and evaluate the pH level of the solution in different environment and with different detection techniques. In the following a review on the biodegradable and wireless pH sensing mechanisms that would suit best the project's scope will be performed.

The model that have to be taken in consideration for the ion sensitive materials is based on the site-binding model. The assumption made here is related to the gate oxide surface, where the surface hydroxyl groups can be neutral, protonized or deprotonized, depending on the solution pH hence on the H^+ concentration, as previously described in Chapter 2.1.

- **Wireless Sensors:**

A wireless-based sensing device will be discussed. This sensor is based on a resonating structure with some pH sensitive material on its gap or on its surface. Both cases will be described in the following and will be further studied in the following chapters. Depending on the pH level, more or less H^+ ions will be binding on this structure, changing the local behaviour of the material.

The first one discussed is based on the presence of an ion sensitive material deposited in the gap of the resonating structure. Due to its presence an ion, molecule or protein will bind on its surface allowing a shift of the intrinsic resonance frequency of the device. The sensor described by Reinecke et al in [48], is based on a functionalization of the split which induces a selective molecular binding, causing a change in permittivity and a shift in the split gap capacity. The structure in Figure 2.7 a, shows a split ring resonator with an interdigitated gap, where a deposition of a 5' amino-modified aptamers layer in the gaps of the SRR takes place. In Figure 2.7 b, instead, it is shown how the binding of the *CRP* proteins induces a variation of the resonance frequency of the device, allowing the detection of its concentration.

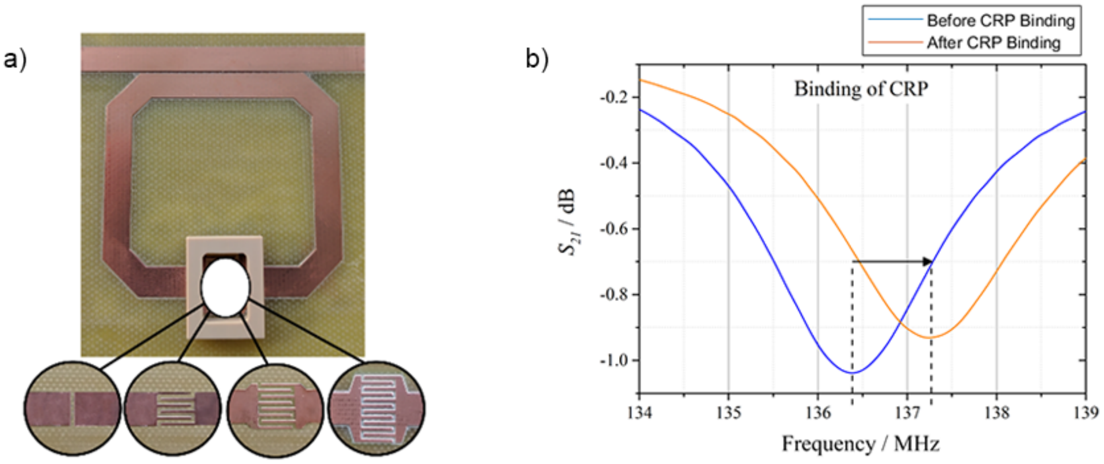

Figure 2.7: Resonating device with an ion sensitive material in its gap structure, *a)*; the variation of resonance frequency depending on the pH of the environment, *b)*, from [48]

The second one is based on an ion sensitive material deposited on top of the resonating device. Its behaviour is similar to the one defined before. The sensitive layer will vary its dielectric properties depending on the amount of the binded ion, molecules, or proteins on top of it, inducing a shift in resonant frequency. The sensor fabricated and described by Arefin et al in [49], shows a micro-scale sensor allowing the detection of pH shifts from *1* to *4* and *10* to *12*. In Figure 2.8 a, it is shown the final device outlook, also on the material point of view. Here the ion sensitive material employed is the Silicon Nitride, Si_3N_4, deposited on top of the interdigitated gold electrodes, allowing the binding of the ions on the surface modifying the overall electromagnetic properties.

It is possible to note that while increasing both H^+ and OH^- concentrations, the resonant frequency will tend to increase, in both cases it is induced by the local electric field around the ions interacting with the applied electric field in the bulk solution. Lower pH, or lower pOH, will induce a decrease of the dielectric constant. This shift in dielectric constant can be measured by looking at the resonating frequency, as shown in Figure 2.8 b, reporting the behaviour of the device.

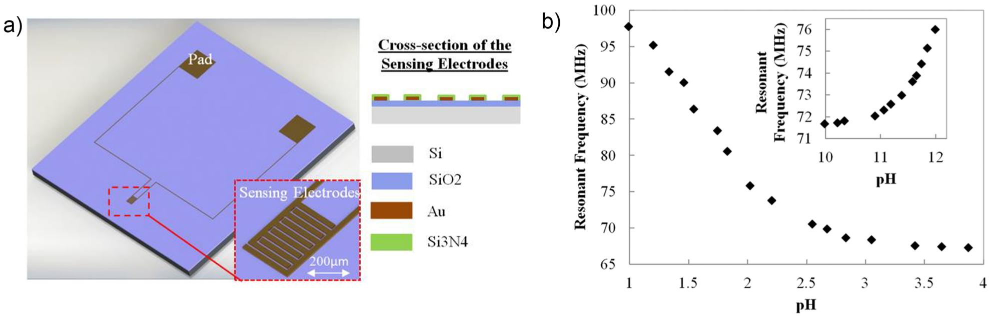

Figure 2.8: Resonating device with an ion sensitive material on its metallic structure, *a)*; the variation of resonance frequency depending on the pH of the environment, *b)*. [49]

- **Biodegradable Sensors:**

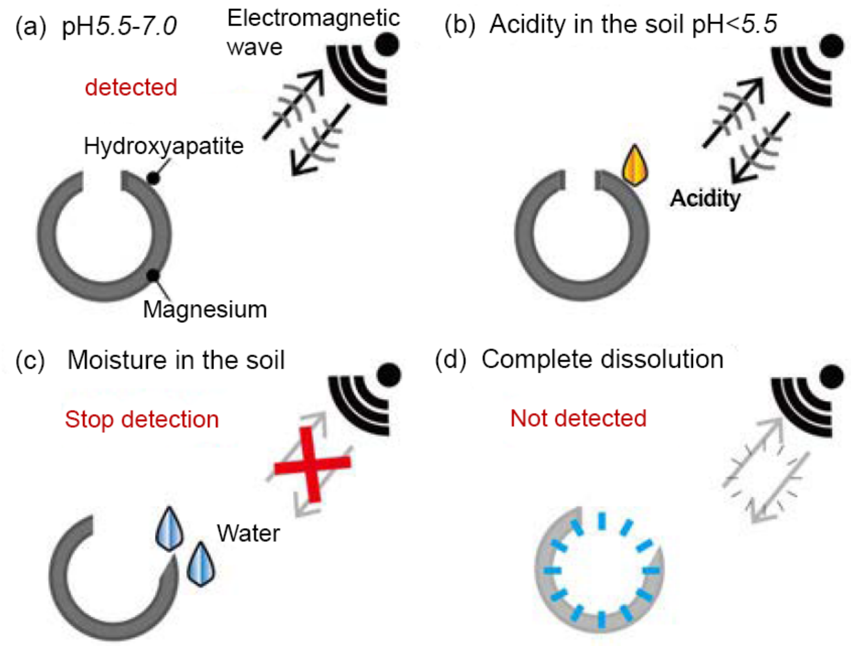

Figure 2.9: Sketch of the biodegradable split ring resonator for soil pH monitoring, [50].

The last sensing mechanism that will be discussed relies on the implementation of a biodegradable yet wireless device. There are few examples of biodegradable and wireless devices, one among the few is the one studied by Boutry et al in [51], where a classical RLC circuit have been fabricated in magnesium, iron and their alloys or conducting polymer composites. The main example taken in consideration for pH sensing is based on ion resistive materials, which tend to degrade only when a certain pH level threshold gets reached. This sub-chapter will be focused on [50]. Hori et al, have shown that it may be possible to have a wireless sensing to detect whether or not the pH of the soil is above or below a certain threshold.

The resonating device is a split ring resonator based on magnesium and coated by a layer of hydroxyapatite which will induce the pH resistance of the sensor. Its functioning can be described as shown in Figure 2.9. The coating will prevent the magnesium based resonating device to be in contact with the liquid environment, allowing it to still resonate at its intrinsic resonance frequency. Once the acidity level in the outer environment reaches the HAp threshold, as shown in Figure 2.9 b to d, the magnesium will be in direct contact with the liquid making it dissolve, hence stopping resonating.

2.2.2 Strain Sensing

The strain is the deformation of a material once a load is applied. It has no unit of measurement since it is defined as the relative length difference. As previously mentioned, the strain is one of the mechanical key factors that will help the bony regeneration once a substitute gets implanted inside the human body. If the bone is subjected to a too low strain, a weakening of the bone and its density may take place, due to the lack of stimulus during remodelling. If the applied strain is too high, then the bone cannot properly proceed to its correct union, making hard the formation of the bone. Hence, a check on the strain that gets induced on the bone substitute is really important. There are several methods to detect the strain induced onto a device by employing different sensing mechanisms such as capacitive, FETs based, or more by using piezoelectric and triboelectric materials, or varying resistive sensors, [52]. In this chapter a state of the art of strain sensors will be considered, with a specific focus on those structures that allow one of the most important parameters for the project's goal which are: biodegradability and wireless sensing.

- **Biodegradable Sensors:**

The fully biodegradable strain sensors can usually be divided into two main subgroups resistive and capacitive. Here a small description of both of them is reported.

The first group are usually based on a conductive polymer composite or *CPC*, described by [53] and [54]. To fabricate these materials, either some conductive fillers are inserted inside the polymeric matrix, or a coating layer of a conductive material occurs on the substrate. This will allow the creation of a material that intrinsically have similar mechanical properties of a polymer and electrical properties of a metal. In Figure 2.10 a, it is shown a sketch of the device fabricated by [53] based on the incapsulation of conductive material inside the polymetric matrix. It is further shown how by increasing the strain applied to the material a lower number of carbon nanotubes, *CNTs*, will be in contact, increasing the overall material resistance, as depicted in Figure 2.10 b.

The one represented in Figure 2.10 c, is instead based on the deposition of candle soot, CS, as conductive layer on top of the stretchable Chitosan and PVA based substrate. Also in this case, as reported in 2.10 d, the strain induced on the sensor will induce an increase of the material resistance proportional to the stress applied on the substrate.

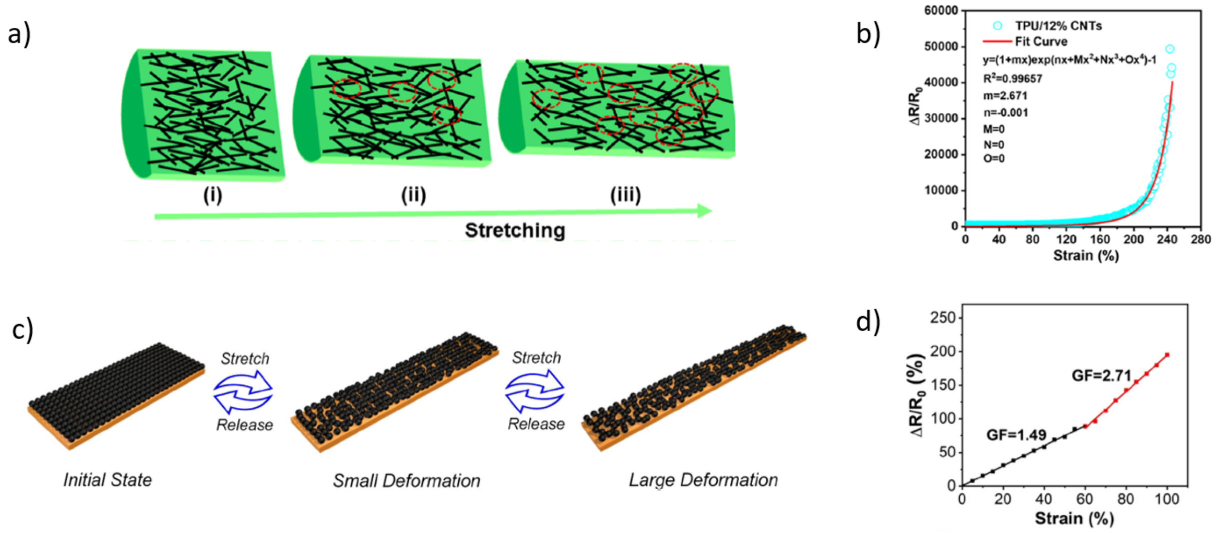

Figure 2.10: Biodegradable strain sensors based on conductive polymer composites. In *a)* and *b)* is shown a sketch of [53] structure and its response, respectively. In *c)* and *d)* it is depicted the structure of [54] and its resistance to strain dependence, respectively.

The second group is employing a capacitive shift to sense the applied strain. Here, the strain applied on the two sides of the sensor usually induces a displacement and a variation of the system capacitance, which can further be sensed. In Figure 2.11 a, will be shown the capacitive strain sensing devices described by Boutry et al, in [55].

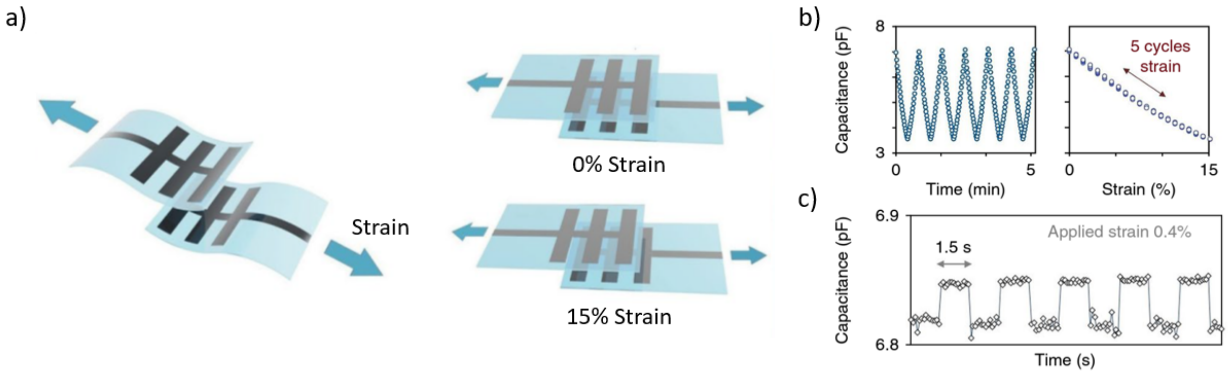

Figure 2.11: Biodegradable strain sensors based on capacitance shift. In *a)* is reported the device structure with and without application of strain, taken from [55]. In *b)* and *c)* is reported the capacitive behaviour once five loading-unloading (0% to 15% strain) cycles have been applied, and the smallest detectable strain, respectively.

This device is based on a non planar sensing mechanism, each one of the two sides of the membrane, have to be clamped to the two parts of a tendon to detect its strain. It relies on $100nm$ of magnesium deposited on top of a $50\mu m$ PLLA substrate. Once the strain is applied on the sensor the two substrate will shift one with respect to the other varying the overall capacitance measured by the device.

As shown in Figure 2.11 b and c, a variation of the strain applied on the sensing device will induce a shift of the capacitance between the two interdigitated metal layers. The loading and unloading of the strain on the device do not induce a huge shift on the initial capacitance value once resting. Further, it has been reported that the lowest strain that can be sensed is on the order of 0.4%, inducing a shift of capacitance of few tens of pico-Farads.

- **Wireless Sensors:**

Then a focus on the wireless strain sensing mechanism will be taken in consideration. This method relies on the employment of resonating devices which thanks to the strain induced on the substrate, a resonance frequency peak variation will take place. To increase the strain sensing, a piezoelectric material may be employed, to enhance the dependence of the strain applied on the frequency shift.

First a discussion about a classical resonating device without the employment of piezoelectric materials, as the one described by Melik et al in [56], will be reported. Here a nested split ring resonating device has been fabricated as strain sensing device.

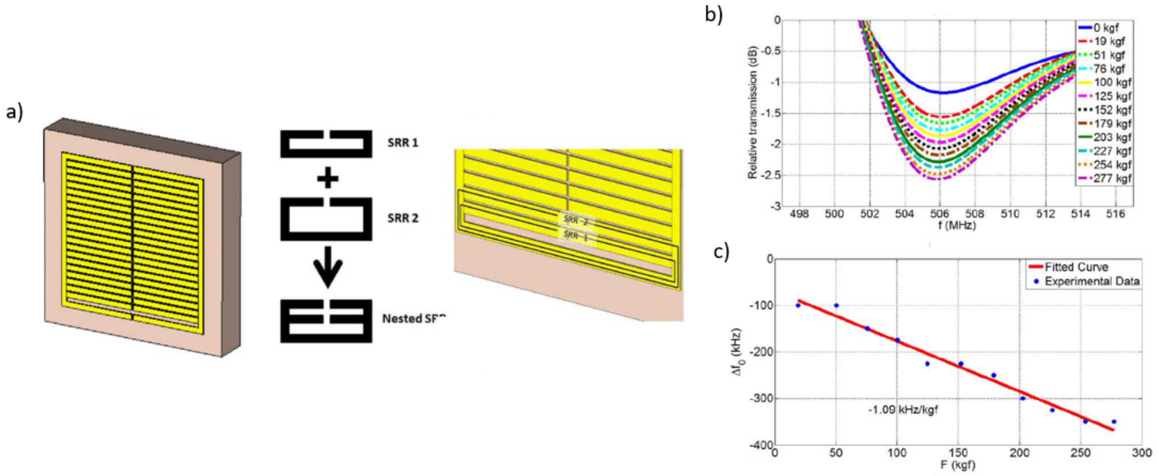

Figure 2.12: Wireless strain sensors fabricated by [56]. In *a)* is reported the device structure. In *b)* and *c)* is reported the resonance peak shift once a force of 0 to 277 kgf gets applied, and its normalized value variation, respectively.

The device shown in the previous figure, is a gold nested split ring resonator deposited on top of a silicon substrate. To increase the capacitance value of the interdigitated resonator, hence reducing the resonating frequency of the device, a dielectric layer made of silicon nitride, Si_3N_4 have been deposited in between the gap of the device. Once a force gets applied on the polyimide substrate, onto which the resonating devices have been fixed, it is possible to characterize a shift in resonance frequency quasi-linearly proportional to the applied force, inducing a variation of around a kHz per kgf of applied force, as reported in Figure 2.12 c.

In Figure 2.13 a, is shown the wireless strain sensor fabricated by Li et al in [57] which employs a PZE material on top of the resonating structure. Here an interdigitated resonating device made of 18 μm of copper have been deposited on top of a polyimide flexible substrate. Then, 390 nm of Aluminum Nitride, AlN, have been deposited on top of the copper device, which thanks to its piezoelectric nature will induce an higher strain sensing ability. The importance of employing a piezoelectric material such as AlN relies on its crystalline structure. Once a strain is applied, its lattice will deform causing positive and negative charges to stop overlapping. Here the electric dipole moment per unit volume is non zero, so the crystal shows polarity on its outside shell, as stated in [57].

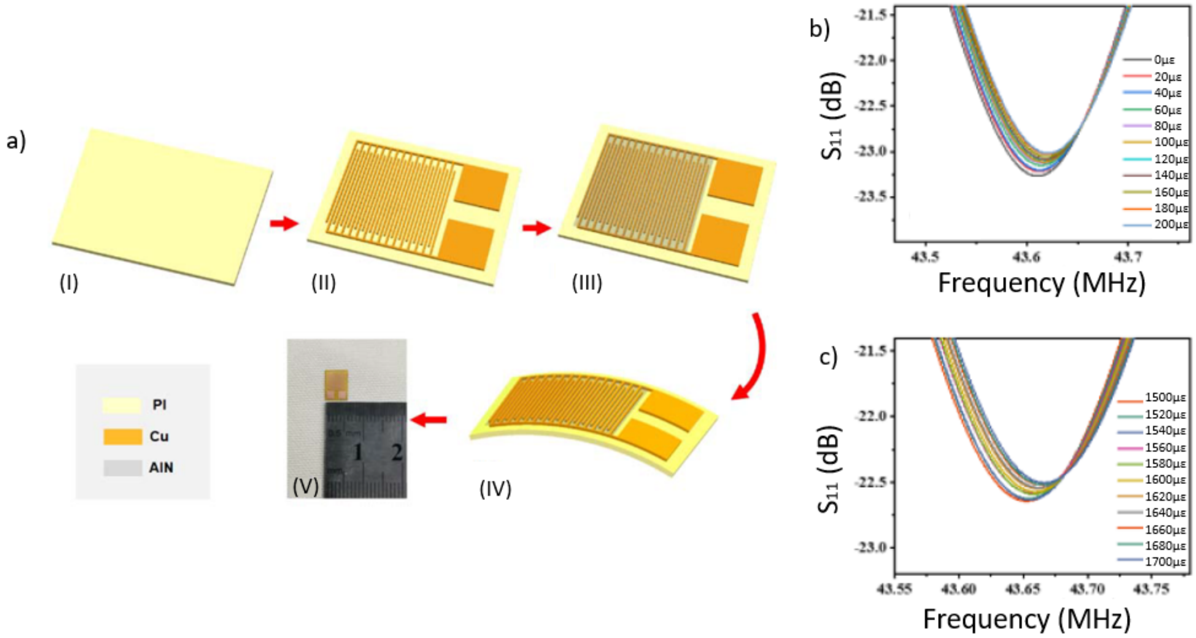

Figure 2.13: Wireless strain sensors fabricated by [57]. In *a)* is reported the device structure and its fabrication processes. In *b)* and *c)* is reported the resonance peak shift once a strain of 0 to 200 $\mu\epsilon$ and a strain of 1500 to 1700 $\mu\epsilon$ gets applied, respectively.

In Figure 2.13 b and c, there are reported the frequency shift of this device that are induced by the strain applied on the polyimide substrate in different ranges. It can be seen how the shift evaluated is on the order of few tens of kHz, making its detection possible once employing a perfectly matching antenna on top of the resonating device. The resonance frequency increases from 43.7089 MHz to 43.735 MHz for a strain that goes from 0 to 3000 $\mu\epsilon$.

2.3 Antenna

The final device will be based on the creation of a passive and wireless sensor, to allow the pH and strain detection after the bone substitution. For this reason, it is important to have an overview of some of the most important antenna and resonators concepts, allowing the reader to follow and understand the design process of the final device.

Several subchapters will be here taken in discussion, starting from the different antenna regions of emission and detection, then focus on the main properties of the different fields' region. Finally, there will be an explanation of the different parameters that characterize the antenna, with a focus on those that allow the detection of resonating structures in different antenna regions. Finally, an overview of RLC resonating structure, with an emphasis on their properties and parameters will be shown, describing in a more particular way the classical split ring, SRR, and the double split ring, DSRR, resonating structures.

2.3.1 Antenna Regions

An antenna is a radiating and receiving element, which converts electromagnetic waves into alternating current and vice-versa. By supposing that the emitted signal travels in free space, without finding any obstacles, it will progress into several regions, the reactive near-field region, the radiating near-field, or Fresnel, region, and the far-field or Fraunhofer region, [58]. The boundaries of every emission zone will be dependent on the wavelength of emission and on the dimensions of the emitting antenna, on its largest dimension. The amplitude pattern of the antenna emission changes shape depending on the region into which it gets analysed, since there is a variation of the field phase and magnitude.

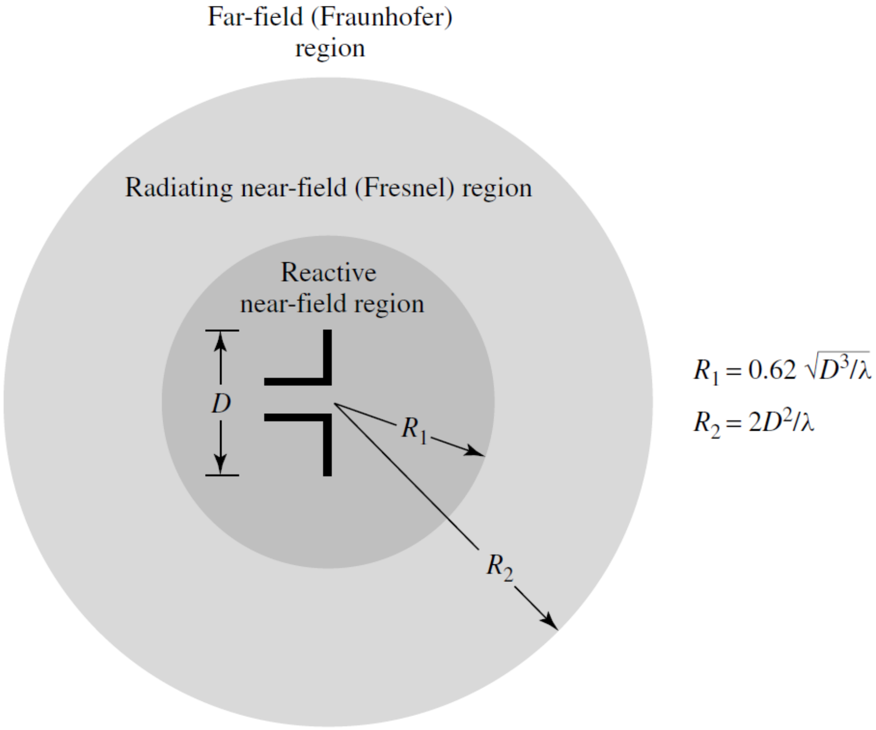

Figure 2.14: Field regions and their characteristic distance from the radiating element, [59]

The *Reactive near-field* region is that space zone directly surrounding the antenna, the inner boundary is the antenna itself, while the outer one can be described by:

$$0 < r < 0.32 \cdot \sqrt{D^3/\lambda} \tag{2.3}$$

For very short dipoles, the outer boundary can be approximated to $\lambda/2\pi$ from the antenna. To propagate the wave, the E-field and the H-field have to be orthogonal and in phase. In this region the two fields are out of phase of 90°, hence this zone is called "reactive". No radiation pattern emitted by the antenna are observable, there is a high content of non-propagating stored energy near the antenna. The field pattern is more spread out and uniform.

The *Radiating near field* or *Fresnel* region, is the zone in between the reactive near field and the far field ones, hence the observation distance will be equal to:

$$0.32 \cdot \sqrt{D^3/\lambda} < r < 2 \cdot D^2/\lambda \tag{2.4}$$

Here radiation fields predominates, and there is a beginning of transition of the E-field and H-field from reactive to radiating fields, but still not completely transitioned, not fully perpendicular to each other, and the field radiation pattern is a function of the radial distance. Here the pattern starts to smooth out, and some lobes will start to form.

In the *Far-Field* or the *Fraunhofer* region the angular field distribution is independent on the distance from the antenna, in any point more distant than $2 \cdot D^2/\lambda$ will be validated the far field condition. The boundaries of this region hence are:

$$2 \cdot D^2/\lambda < r < \infty \tag{2.5}$$

In this zone the E-field and the H-field are mutually orthogonal each other and to the propagation direction, E and H are only function of z, the propagation direction, and time. The emitted wave can be considered as a plane wave, since the spherically radiated wave appears locally planar if observed by a very distant point. The pattern is completely formed, there will be minor or secondary lobes and one or more major, or primary, lobes.

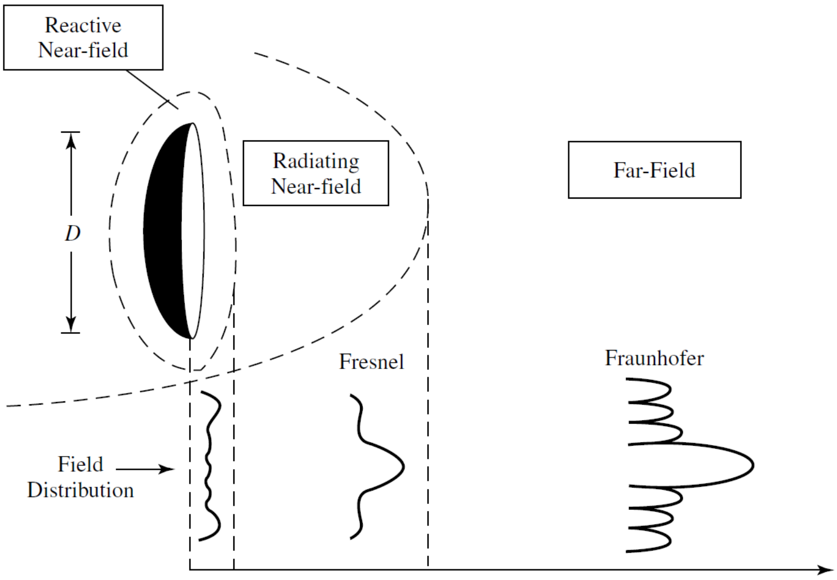

Figure 2.15: The difference between the reactive-, radiating- and far- field regions, from [60]

A plane wave can be considered as a transverse electromagnetic wave, TEM, which varies only in one spatial dimension. A TEM wave has electric and magnetic fields perpendicular to one another and to the direction of propagation, z, forming a right-handed triad. A plane wave magnitude, phase and orientation must depend only on the direction of propagation, since there is a constrained variation of the E- and H- fields only on the propagation direction z. If the E field propagates along the x axis and the H field along the y axis, the relations that will describe them, will be a function only on the propagation direction along z, [61].

$$\bar{E} = E_0 e^{-j2z} \hat{a_x} \tag{2.6}$$

$$\bar{H} = H_0 e^{j2z} \hat{a_y} \tag{2.7}$$

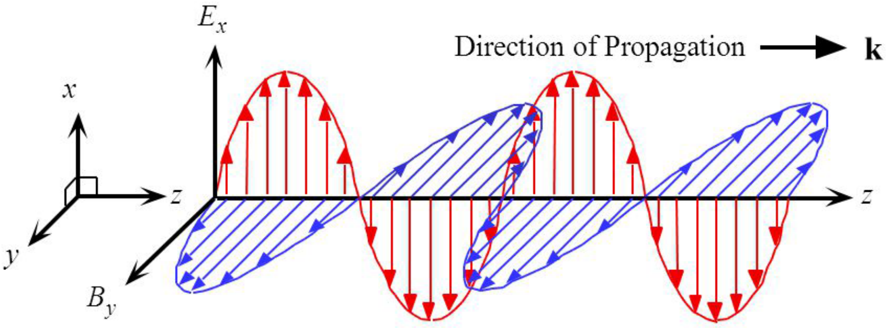

Figure 2.16: A plane wave with the electric field and magnetic field components along the x and y axis, respectively, while the direction of propagation is along the z axis, [62]

The Poynting vector direction, the cross product of the E and H field and corresponds to the directional power flow, is in the propagation direction of the wave. Its definition and its absolute value are reported in Equation (2.8). The ratio of the magnitudes of the E and H vectors is the same and constant for any given instant of time.

$$ExH = E_x(z,t)H_y(z,t)u_z = P(z,t)u_z \quad ; \quad S = |E||H| = |E|^2/\eta = \eta|H|^2 \tag{2.8}$$

η is the intrinsic impedance of the medium where the wave travels. It can be defined as the square root of the ratio of the magnetic permeability and the dielectric permittivity, [63].

2.3.2 Antenna Parameters

In this sub chapter there will be a discussion about some of the antenna parameters that will be important for the detection of the sensing structure. A small focus on the gain, directivity, incident and scattered power of a generic antenna will be taken in consideration, to allow a better understanding of the characterization method of the resonating structures.

Then an emphasis on the far field and near field parameters will be taken in consideration. Depending on the zone into which the observable object is placed, different parameters will allow its detection. Depending on near field or far field, the S_{11} or the “Scattering Reflection Coefficient” or the RCS or the “Radar Cross Section”, will give informations about the device.

First some of the fundamental antenna parameters will be shown and discussed, that will be needed for the definition of the two above near field and far field detection parameters. It is important to define the radiation pattern of an antenna at first, which is a representation of the radiation properties of the antenna in space coordinates.

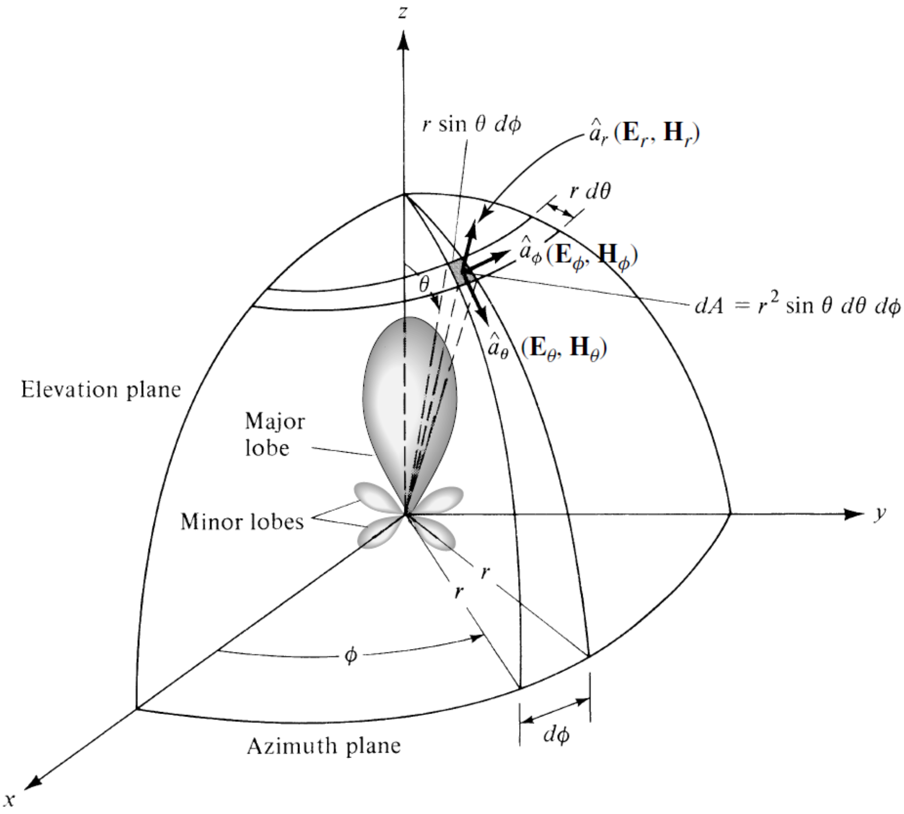

Figure 2.17: Antenna spherical coordinates, and definition of solid angle Ω, [59]

Some parameters that characterize the antenna's radiation pattern are, [59]:

- **Solid Angle** is described in steradians (sr), which can be defined as the solid angle with a vertex at the centre of a sphere of radius r that is subtended by a spherical surface area of a square with each side of length R. The angular measurement of a spherical surface will be equal to $\Omega = 4\pi R^2/R^2 = 4\pi$:

$$d\Omega = \frac{dA}{R^2} = \sin\theta d\theta d\phi \tag{2.9}$$

- **Radiation Energy**, which is the radiated power from an antenna per solid angle:

$$U(\theta,\Phi) = r^2 W_{rad} = \tfrac{r^2}{2\eta}|E(r,\theta,\Phi)^2| \quad ; \quad P_{rad} = \oint_\Omega U\, d\Omega = \int_0^{2\pi}\int_0^{2\pi} U \sin\theta\, d\theta\, d\Phi \tag{2.10}$$

with U the radiation intensity, W_{rad} the radiation density and P_{rad} the total radiated power, which is the integral of the radiation intensity over the entire solid angle. If isotropic source, U will be independent on the angles θ and Φ, hence:

$$P_{rad} = 4\pi U_0 \quad ; \quad U_0 = P_{rad}/(4\pi) \tag{2.11}$$

- **Directivity**, or directive gain, is the ratio of the radiation intensity in a certain direction from the antenna to the radiation intensity averaged over all directions. If the direction is not specified, then the direction of maximum radiation is described in Equation (2.12):

$$D = U/U_0 = (4\pi \cdot U)/P_{rad} \quad ; \quad D_{max} = D_0 = U|_{max}/U_0 = (4\pi \cdot U_{max})/P_{rad} \tag{2.12}$$

  With U_{max} and U_0 as the maximum and the isotropic source radiation intensity.

- **Antenna Radiation Efficiency** considers losses at the input terminal and within the antenna, the overall efficiency is usually written as:

$$e_0 = e_r e_c e_d = e_r e_{cd} \tag{2.13}$$

  With e_0 as the total efficiency, e_r as the reflection mismatch efficiency, e_c as the conduction efficiency and e_d as the dielectric efficiency.

- **Gain** is the ratio of the intensity in a given direction over the radiation intensity that would be obtained if the power accepted by the antenna was radiated isotropically:

$$G = 4\pi \frac{U(\theta, \Phi)}{P_{in}} \tag{2.14}$$

  Where P_{in} is the total input accepted power, can be defined by $P_{rad} = e_{cd} P_{in}$, hence:

$$G(\theta, \Phi) = e_{cd} D(\theta . \Phi) \tag{2.15}$$

- **Effective Area** gives information about how much power is captured from a plane wave delivered from an antenna. It is the ratio of the available power at the terminals of a receiving antenna over the flux density of a plane wave incident on the antenna. The ratio between the gain and the effective area is constant for every antenna emitting at the same wavelength, it is one of the key parameters of an antenna.

$$G/A_e = 4\pi/\lambda^2 \quad ; \quad A_e = \tfrac{\lambda^2}{4\pi} G = \tfrac{\lambda^2}{4\pi} D_0 \tag{2.16}$$

After this overview on the classical parameters that define an antenna and its properties, it is possible to focus on those parameters that will really be needed for the project goal, which are the RCS and the S_{11}.

The **Radar Cross Section** is used to evaluate the strength of the scattered fields, to evaluate the power of reflection of the structure, the bigger the resonating structure is, the easier will be the detection of it [59][64]. The RCS is employed to characterize the scattering properties of a target in the far field region, since it relies on the plane wave condition of the impinging signal. It is function of the polarization of the incident wave, the angle of observation, the geometry and properties of the target and the operation frequency.

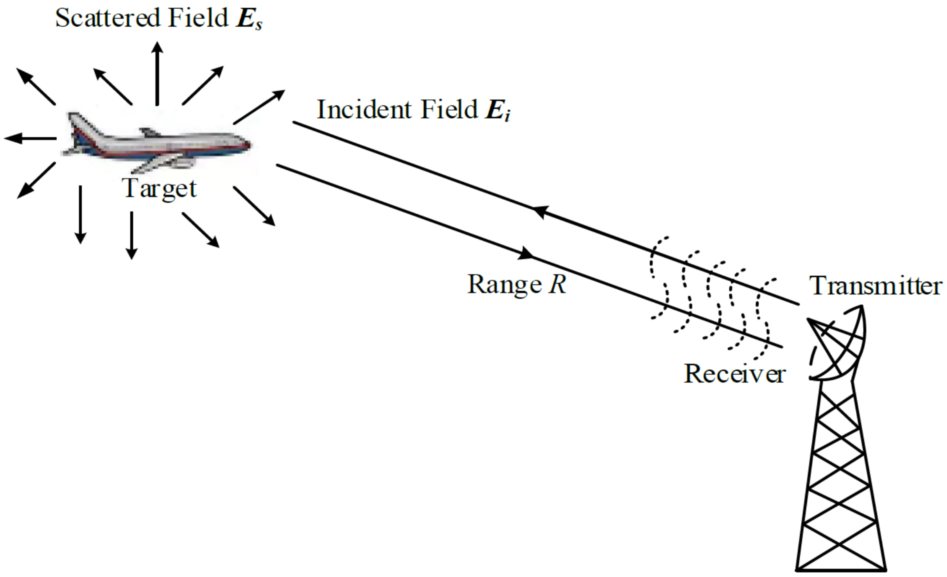

Figure 2.18: Sketch depicting the radar cross section behaviour, [65]

This parameter is defined in dB_{sm}, decibel relative to square meters, as:

$$dB_{sm} = 10 \cdot log_{10}\left(\frac{\sigma}{1} \cdot \frac{[m^2]}{[m^2]}\right) \tag{2.17}$$

The RCS defined in Equation (2.19), is the area, σ, intercepting some incident power which will get isotropically scattered, in every direction, producing in the receiver a power density W_s equal to that scattered by the actual target.

$$W_s = \lim_{R\to\infty}\left[\frac{\sigma \cdot W_i}{4\pi R^2}\right] \tag{2.18}$$

Here $4\pi R^2$ is the surface of the radiation sphere, the target is supposed to be at very large distance R from the radiating element, W_i is the incident field power density, $P_i = \sigma \cdot W_i$ is the intercepted power. By isolating the Radar Cross Section from the previous formula:

$$\sigma = \lim_{R\to\infty}\left[4\pi R^2 \cdot \frac{W_s}{W_i}\right] \tag{2.19}$$

The plane wave approximation have been taken in consideration since supposed to be working at very large observation distances, considering the impinging spherical wave on the target samples as a plane wave. Is possible to define the power density of a plane wave as the square of the absolute electric field value over the wave impedance, shown in Equation (2.20), to derive a more compact way to describe the radar cross section parameter.

$$W_{i,s} = \frac{|\vec{E_{i,s}}|^2}{R} \tag{2.20}$$

This definition works for both the incident and the scattered power density, by considering their own electric field component. Hence this would lead to the following formulation of the RCS parameter, σ, as reported in Equation (2.21).

$$\sigma = \lim_{R\to\infty} \left[4\pi R^2 \cdot \frac{|\vec{E}_s|}{|\vec{E}_i|} \right] \tag{2.21}$$

In the case into which the target material corresponds to an isotropic scatterer, $\sigma = A$. If instead a flat target is considered perpendicular to the incidence field direction creating a non-isotropic scattering, the projected surface will be equal to the area of the plate, and the intercepted power will be equal to the incident power density times the area. Here a directed reflection pattern will take place, making the RCS dependent on the directivity of the reflected field. Directivity can be evaluated from the Equation (2.16) and can also be defined as the radiated power density over the average irradiated power density:

$$D = 4\pi \frac{A_e}{\lambda^2} = \frac{W_s}{W_i/(4\pi R^2)} \tag{2.22}$$

From the above definitions it is possible to gather the Radar Cross Section of the plate:

$$\sigma = 4\pi R^2 \frac{W_s}{W_i} = D \cdot A_e = 4\pi \frac{{A_e}^2}{\lambda^2} \tag{2.23}$$

Considering the case of a Monostatic antenna, where the same antenna works as emitter and as receiver, it is possible to define the radar equation as follows:

$$\tfrac{P_r}{P_t} = \sigma G^2 \lambda^2 \cdot (4\pi)^{-3} \cdot R^{-4} \quad ; \quad \sigma = [(4\pi)^3 P_r \cdot (P_t G^2 \lambda^2)^{-1}] \cdot R^4 \tag{2.24}$$

With R the distance between the monostatic antenna and the resonating structure; P_t and P_r are respectively the total radiated and received power; G is the gain of the antenna.

The **Scattering Reflection Coefficient**, or S_{11}, will be the last parameter discussed. It shows the detectability of a resonating structure in the near field regime. The scattering matrix gives a description of the internal network seen at its ports, [66]. In the microwave world it relates the voltage wave incident on the ports to those reflected from the structure.

$$\begin{bmatrix} V_1^- \\ \vdots \\ V_N^- \end{bmatrix} = \begin{bmatrix} S_{11} & \cdots & S_{1N} \\ \vdots & \ddots & \vdots \\ S_{N1} & \cdots & S_{NN} \end{bmatrix} \begin{bmatrix} V_1^+ \\ \vdots \\ V_N^+ \end{bmatrix} \tag{2.25}$$

A generic element of the scattering matrix can be determined by considering that all the ports except the j-th one are terminated in matched loads to avoid internal reflections. So, to gather the scattering matrix S_{ij}, a voltage V_j^+ should drive the port j, and from the port i, V_i^-, will be measured. It can be defined as follows:

$$S_{ij} = \frac{V_i^-}{V_j^+}\bigg|_{V_k^+ = 0 for k \neq j} \tag{2.26}$$

The S_{ii} is the reflection coefficient seen by looking into port i when all other ports are terminated in matched loads, while the S_{ij} is the transmission coefficient from port j to port i when all other ports are terminated in matched loads. A two-ports network will be studied, a focus on the reflection and transmission coefficient of the resonating structure will occur. The resonating structure will be considered as a black box, its properties are unknown until a signal gets sent and then recorded from outside.

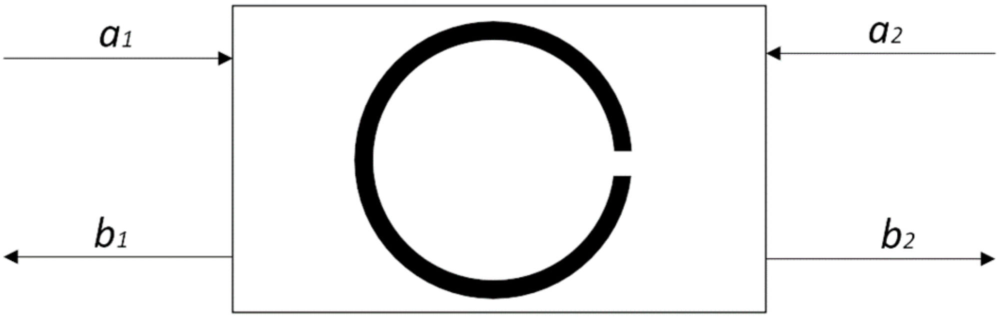

Figure 2.19: Sketch of a generic two-port system to describe the scattering parameters.

In Figure 2.19, the two-port system is depicted, showing how by studying the input and output of each one of the two port, it is possible to gather information about the reflection and the transmission coefficient.

$$\begin{bmatrix} b_1 \\ b_2 \end{bmatrix} = \begin{bmatrix} S_{11} & S_{12} \\ S_{21} & S_{22} \end{bmatrix} \begin{bmatrix} a_1 \\ a_2 \end{bmatrix} \tag{2.27}$$

Here the four scattering parameters describe the forward and backward reflection, respectively S_{11} and S_{22}, and transmission, respectively S_{21} and S_{12}, coefficients. Each one of them will give a different information about the resonating device, allowing hence the complete characterization of it. The scattering matrix in the two ports network are shown in the following matrix. Here it has been taken in consideration the normalized voltage waves. $|a|^2$ and $|b|^2$ represent the power of the forward and reverse wave and are defined as follows:

$$a(x) = v^{+}(x)/\sqrt{Z_0} \quad ; \quad a(x) = v^{-}(x)/\sqrt{Z_0} \tag{2.28}$$

$$S_{11} = a_1/b_1 = R \quad ; \quad S_{12} = a_1/b_2 = T \tag{2.29}$$

By defining $[Z]$, as the impedence matrix relating the voltage and the current matrices in a multi-port network, $[V] = [Z][I]$, described by its real, Z_r, and immaginary, Z_{im}, part, it is possible also to define the Scattering matrix as reported in Equation (2.30).

$$[S] = \{[1] - [y]\}\{[1] + [y]\}^{-1} \quad ; \quad [y] = [Z_r]^{1/2}[Y][Z_r]^{1/2} \tag{2.30}$$

2.3.3 Resonating Elements

Before entering in the details of the split ring resonators and the parameters that characterize them, an overview of the generic resonating structure will be described. The RLC resonators and their behaviour will be shown, then a focus of some of the SRR structure will be taken in consideration, with a specific focus on the single and on the double split ring resonators, having care to demonstrate and show the equation that describe them at best.

- **RLC Resonators**

This type of devices consists on a resistance, R, an inductance, L, and a capacitance, C in series or in parallel. In Figure 2.20, it is shown the two classical circuits that describe them.

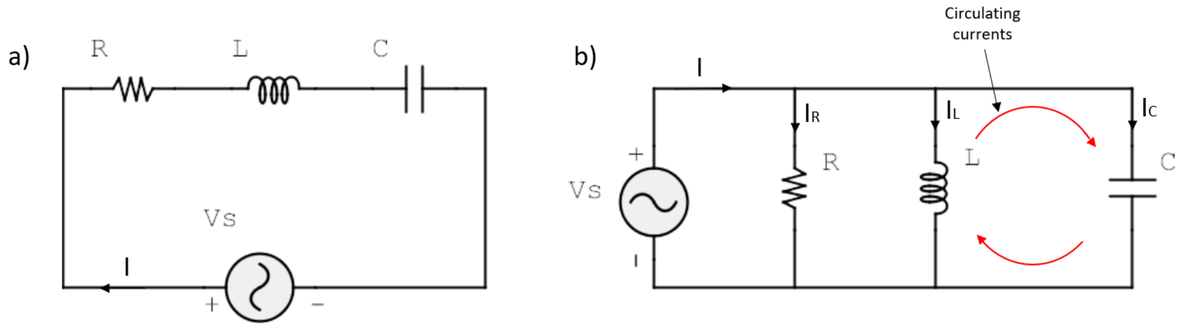

Figure 2.20: The series and parallel RLC circuits, respectively in *a)* and *b)*

It is important to define at first the inductive and capacitive reactances and susceptance, as the impedance and admittance. In the series circuit senario, reported in Figure 2.20 a the reactances and the impedances will be describing the system as follows:

$$X_L = 2\pi f L \quad ; \quad X_C = \tfrac{1}{2\pi f C} \quad ; \quad Z = \sqrt{R^2 + X^2} = R + jX \tag{2.31}$$

There is a point in which the two inductances will be equal and opposite each-other, making the overall impedance equal to the resistance of the circuit, allowing to reach minimum inductance level of the system. The LC will be considered as a short circuit, making the overall circuit completely real.

$$X_L = X_C \Rightarrow 2\pi f L = \frac{1}{2\pi f C} \tag{2.32}$$

Allowing hence the evaluation of the resonance frequency f_r as follows:

$$f_r = \frac{1}{2\pi\sqrt{LC}} \tag{2.33}$$

In the case in which there is a parallel RLC circuit, as shown in Figure 2.20, the susceptances and the admittance will be considered to describe the system, and will be reported here:

$$B_L = \tfrac{1}{2\pi f L} \quad B_C = 2\pi f C \quad ; \quad ; \quad Y = 1/Z = \sqrt{G^2 + B^2} \tag{2.34}$$

At the resonance frequency the circulating current between the inductor and the capacitor will be high, inducing oscillations of energy. The admittance describing the circuit, reported in Equation (2.35), will be minimum once the resonance frequency occurs and the X_L becomes equal and opposite to X_C, as previously shown in Equation (2.33). Hence, the impedance hits its maximum value once resonance occurs $Z = R_{MAX}$.

$$Y = G + B_L + B_C = \frac{1}{R} + \frac{1}{2\pi f L} + 2\pi f C \tag{2.35}$$

The other parameters that will describe the circuit are: the quality factor, Q that indicates the sharpness of the peak, and shows the maximum stored energy in the system, reactance, over the dissipated one, resistance, during the oscillation cycle and is reported in Equation (2.36) for both series and parallel circuit, respectively; and the bandwidth of the system defined as $BW = f_r/Q$, which describes the range of frequencies where at least one-half of the maximum power gets provided.

$$Q = \frac{X_{L/C}}{R} = \frac{1}{R}\sqrt{\frac{L}{C}} \quad ; \quad Q = R\sqrt{\frac{C}{L}} \tag{2.36}$$

- **Single Split Ring Resonator**

First a focus on the inductance will take place, by considering a square like conductor, with a gap. Then by considering the theory behind a circular SRR, the capacitive behaviour of the resonating device will be extended to the square like SRR.

From Grover's book [67], the equivalent inductance of a rectangular conductor having a rectangular section is equal to Equation (2.37), with a and b the two sides of the rectangle, d as the diagonal of the rectangle, w and h as the two sides of the rectangular conductor section.

$$L = 4\left[(a+b)\cdot ln\left(\frac{2ab}{w+h}\right) - a\cdot ln(a+d) - b\cdot ln(b+d) - \frac{a+b}{2} + 2d + 0.477(w+h)\right] \tag{2.37}$$

By considering the shape as a square, $a = b = l$, the previous equation will be:

$$L = 4\left[2l\cdot ln\left(\frac{2l^2}{w+h}\right) - 2l\cdot ln(l(1+\sqrt{2}) - l + 2l\sqrt{2} + 0.477(w+h))\right] \tag{2.38}$$

The inductance considered so far is normalized over μ_0/π, and its measurement unit is in m. To have it described in H,it is possible just to multiply the previous formula by the normalizing factor. By doing so it is possible to gather the relation that describes the inductance of a square conductance with a rectangular section. By further taking care of the slit in the square SRR, a weighting factor has to be taken in consideration. This weighting factor, ρ_e, considers the gap over the overall structure, and can be so defined:

$$\rho_e = 1 - \frac{g}{4l} \tag{2.39}$$

The final inductance is reported in Equation (2.40), is the same reported by Vallecchi, [68].

$$L = \rho_e\frac{\mu_0}{\pi}\left[2l\cdot ln\left(\frac{2l^2}{w+h}\right) - 2l\cdot ln(l(1+\sqrt{2}) - l + 2l\sqrt{2} + 0.477(w+h))\right] \tag{2.40}$$

For what concerns the overall structure's capacitance, it can be considered as the sum of two capacitances: the gap and the surface ones, which will be described in the following. Here a study contemplating a circular SRR will be taken in consideration at first.

The gap capacitance, if the distance between the two resonating side is narrow enough, can be considered as the parallel between two sub-capacitances. The parallel plate capacitor formed by the gap, and the correction term due to the fringing fields of the metallic plates, defined as fringe capacitance. By considering w and h as the width of the wire and the thickness of it, respectively, it is possible to describe it as follows:

$$C_{gap} = C_{pp} + C_{fringe} = \epsilon_0 \left[\frac{(h+g)(w+g)}{g} \right] \tag{2.41}$$

The other term that will characterize the overall capacitance of the structure is the surface capacitance which rise by considering that in vicinity of the small gap, the SRR will look like two planes, assumed infinitely long and thin, creating a 2D electrostatic problem. In Figure 2.21 b, it is reported the surface capacitance electrostatic theory described by [69].

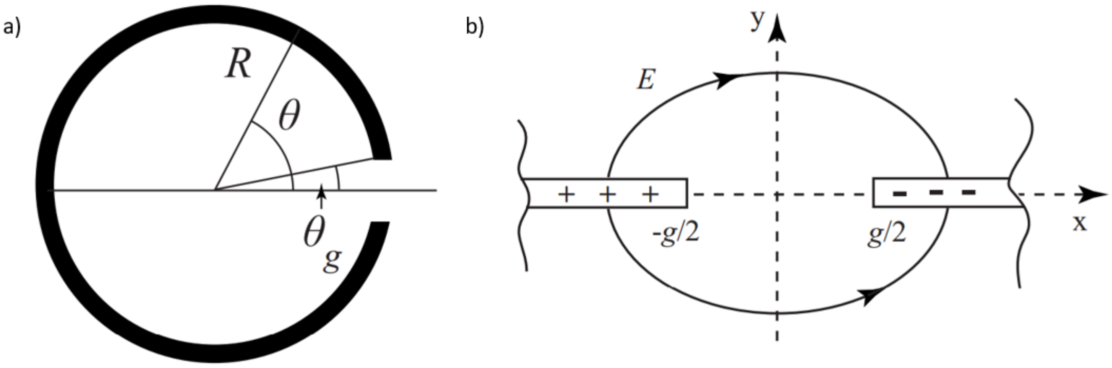

Figure 2.21: In *a)* the top view of the single SRR, in *b)* view of the split ring narrow gap, that acts like two semi-planes, [69]

$$C_{surf}^{puh} = \int_{\theta_g}^{\pi} \frac{\sigma(\theta)R}{V(\theta)} d\theta \tag{2.42}$$

Where, σ is the surface charge, V is the voltage in between two symmetric points on the SRR surface, R is the radius of the SRR, θ_g is the gap angle depicted in Figure 2.21 a.

By taking into account the following formulas demonstrated by [70], considering them applicable also to the above chosen structure, and by considering the θ_g angle small enough to have a $\cot(\theta_g/2)$ big, allowing to neglect the θ at the denominator, the per unit height surface capacitance, can be defined as follow:

$$\sigma(\theta) = \epsilon_0 V_0 \cdot (\pi R)^{-1} \cot\left(\tfrac{\theta}{2}\right) \quad ; \quad V(\theta) = (V_0/\pi) \cdot (\pi - \theta) \tag{2.43}$$

$$C_{surf}^{puh} = \frac{2\epsilon_0}{\pi} log \frac{4R}{g} \tag{2.44}$$

The overall surface capacitance can be further described by integrating Equation (2.44), and can be written as:

$$C_{surf} = (h+w) \frac{2\epsilon_0}{\pi} log \frac{4R}{g} \tag{2.45}$$

By considering the surface capacitance and the gap capacitance to be in parallel, the total capacitance will be the sum of the two, shown in Equation (2.46).

$$C_{tot} = C_{gap} + C_{surf} \tag{2.46}$$

- **Double Split Ring Resonator**

Knowing the singular inductance for the single square SRR, reported in 2.40, it is possible to evaluate the mutual inductance between the two rings of a square split ring resonating device. Grover in [67] defines the mutual inductance between two equal parallel squares as:

$$M = 8\left[l \cdot log\left(\frac{l+\sqrt{l^2+g^2}}{l+\sqrt{2l^2+g^2}} \cdot \frac{\sqrt{l^2+g^2}}{g}\right)\right] + 8\left[\sqrt{2l^2+g^2} - 2\sqrt{l^2+g^2} + g\right] \tag{2.47}$$

Where l is the length of the common parallel inductor side, g is the distance between the two metallic lines. It is the sum of several inductances of parallel sides.

To study the capacitances instead, in Figure 2.22, is reported the structure that will be taken into account for the DSRR frequency analysis. Here two capacitances arises, which are: C_s the gap and surface capacitance, previously defined, and C_m which is the mutual capacitance that relate the two rings, as described by Sauviac et al in [71].

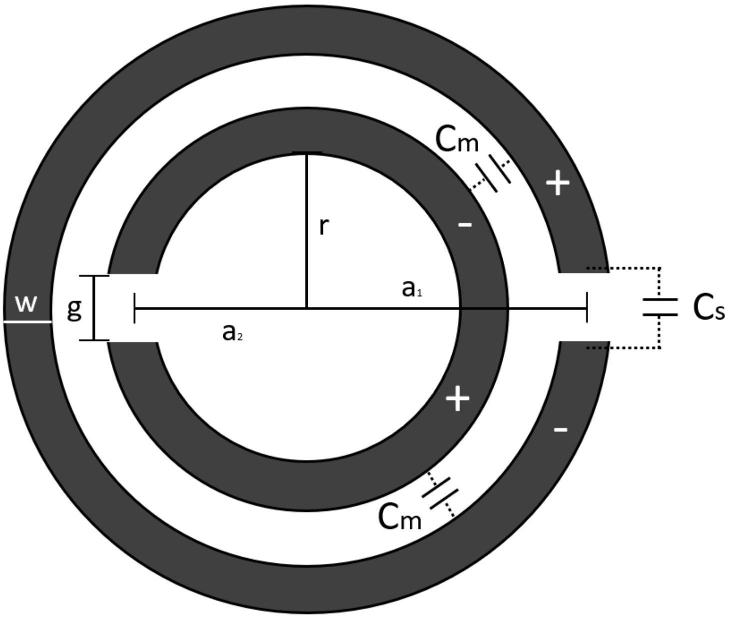

Figure 2.22: Circular DSRR, to study the capacitance effect on the resonating device.

There will be two capacitances in the system that rely on the two different rings:

$$C_1 = C_{S1} + C_m/2 \quad ; \quad C_2 = C_{S2} + C_m/2 \tag{2.48}$$

The mutual capacitance can be considered as the product of the effective length of the two metal lines, L_{eff}, and the capacitance per unit length of two parallel metal lines separated by a gap g is C_0, and is reported in Equation (2.49).

$$C_m = C_0 \cdot L_{eff} \tag{2.49}$$

The two parameters above mentioned have to be determined. First, Gardiol in [72], have shown that the equation that describes at best the C_0 is the following:

$$C_0 = \frac{2}{\pi}\epsilon_r\epsilon_0 \cdot arccosh\left(\frac{2w}{g}\right) \tag{2.50}$$

For the evaluation of L_{eff}, several approximations have to be taken into account, since it relies on the length where the charge +Q and the charge -Q are uniformly distributed along the two perfect halves of the inner circular SRR, and are dual to the charges of the outer circular SRR. To allow an easy evaluation of this parameter, it is possible to consider the two semi-loops as equivalent parallel metal lines separated by a gap g. The averaged radius and the final value of L_{eff} are reported in Equation (2.51), if the charges in both wires is uniformly distributed.

$$a = (a_1 + a_2)/2 = \left(r + c + \tfrac{d}{2}\right) \quad ; \quad L_{eff} = \pi \cdot a \tag{2.51}$$

If instead a non-uniformity of charges is considered, employing King's theory described in [73] and [74] , by doing the Fourier expansion of the current induced by the impinging magnetic field, and by considering the expansion of the induced charges per unit angle, it is possible to consider that the distribution of the charges can be considered as sinusoidal, reported in Equation (2.52).

$$\tau(\Phi) = \tau_{max} sin(\Phi + \Phi_0) \tag{2.52}$$

Here $\tau_{max} = \sqrt{\tau_1^2 + \tau_2^2}$, and it can be considered that in the loop range $\Phi_0 < \Phi < \pi$ there are the charges $+Q$, while in the range $\pi + \Phi_0 < \Phi < \Phi_0$ there are the charges $-Q$. This will lead the effective length to be equal to $L_{eff} = 2a$.

The resulting mutual capacitance can be written as reported in Equation (2.53), where in the first relation is reported the uniformity approximation, and in the second the non uniformity one.

$$C_m = 2a\epsilon_r\epsilon_0 \cdot arccosh\left(\tfrac{2w}{g}\right) \quad ; \quad C_m = \tfrac{a}{\pi}\epsilon_r\epsilon_0 \cdot arccosh\left(\tfrac{2w}{g}\right) \tag{2.53}$$

Chapter 3

Methodology

In this chapter there will be shown the methodology employed to reach the final desired design of both pH and strain sensing device. Four subchapter will follow, that will give an overview of the design steps performed until the final device gets chosen and simulated. In Chapter 5.2 there will be shown the simulation results, that will be further discussed in Chapter 6. As mentioned in Chapter 2.2.1, there are two very intriguing and yet suitable pH sensing structure, which rely on the employment of an ion sensitive material, such as silicon nitride or metal oxides; and the use of a pH resistive material, such as hydroxyapatite, whose degradation will take place only once a certain H^+ ion concentration threshold gets reached. Further both these two methods may employ biocompatible and biodegradable materials, which would suit best in the final project goal. Both these methods will be here shown and discussed in this chapter.

Then a discussion about the strain sensing devices based on resonating structures will hence be reported. Already in previous chapter several solutions have been shown, and to suit with the project goal the sensing device will have to be, both biodegradable and wireless, allowing a detection of any kind of strain that may take place in the acting plane along one axis rather than another. Hence it will consist on an interdigitated split ring resonator, which depending on the stress that they are subjected to, will produce a different frequency response in the electromagnetic spectrum. In the following a discussion on the different parameters taken in consideration for this sensing device will be hence described.

Finally, a small overview on the simulations performed to test the behaviour of the device once inserted into the human body will be shown, making possible to gather important information on the capability of the far field antenna to get resonating information of the implanted device. To test the in human behaviour Voxel data plugin from CST Microwave Studio have been employed, which consists on importing some materials that perfectly mimic the human body in the electromagnetic point of view.

Several dimension challenges have been taken into account concerning the minimum and the maximum width and thickness of the device, depending on the fabrication method employed and its intrinsic limitations will be discussed in the Results chapter. Small features were hard to reproduce, hence the sensing device will have in general a resonating frequency in the order of few GHz.

3.1 pH Detection Resonators

In this subchapter there will be the description of the several steps that have been performed in order to arrive to the final sensing device for pH detection. It is important that the device meant to be fabricated is biocompatible and biodegradable, allowing the sensor to not get rejected but absorbed by the human body, avoiding a second operation to remove it. Another key aspect for the desired sensor, would be its ability to be sensed wirelessly, making possible the study of its pH value once inserted into the human body, without any external wiring.

As previously shown in Chapter 2.2.1, several different methods may be employed to detect the pH variation inside a solution, some of them rely on the employment of an Ion Sensitive material, which allows the H^+ ions to bind on its surface dangling bonds, others on Ion Resistive materials, where they start to degrade only when a certain pH threshold gets reached. Both detection mechanisms are really interesting for the project goal, and both of them have been studied.

3.1.1 Ion Resistive pH Sensor:

Here as shown by Hori et al in [50], it is possible to create a pH sensor that fully degrades only when a certain pH threshold gets reached. A similar procedure may be employed in this project to have a resonating device working until a pH of 5.5 arise.

To allow the detection of the sensor even once this pH level gets reached, it is possible to employ a double split ring resonator, consisting of two concentric rings. The first method to characterize the pH variation may be the employment of different Hydroxyapatite thicknesses. It may be possible to study the dependence between the surrounding pH and the hydroxyapatite coating degradation rate, allowing to detect a shifting peak, induced by the degradation of one layer over the other. In Figure 3.1, it is shown the idea behind this sensing method. The problem here is the inability to check the exact thickness of the layer, since in literature there is no relation between the processing time and the HAp deposition rate, nor the degradation rate with respect to the environmental pH level, for these reasons it will not be studied.

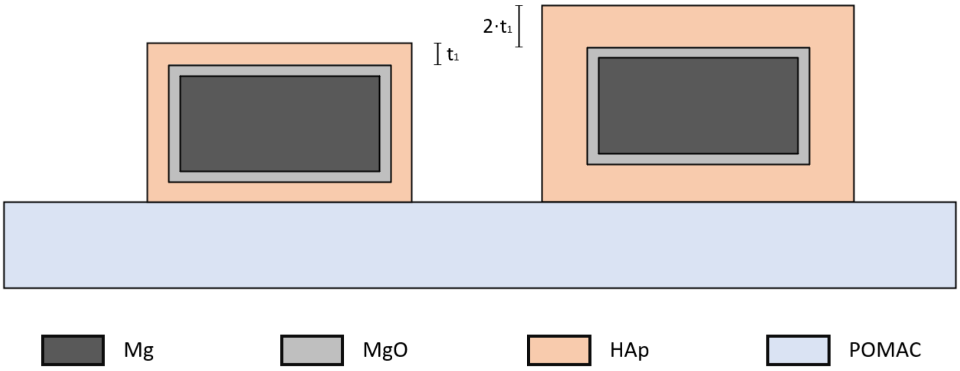

Figure 3.1: pH sensing mechanism dependant on the thickness of the deposited HAp layer, study of the degradation speed dependant on the pH level.

Another way is to have only one ring in direct contact with the liquid environment, degrading if the acidity threshold gets reached, while the other ring remains intact. For this scope a lamination layer may be employed to protect one layer, but also to know exactly when the second ring will be in direct contact with the external surroundings. This is the chosen method depicted and briefly discussed in Chapter 3.4, in Figure 3.7.

Finally, two different materials may be employed to perform this study, which will be pure magnesium for a fast prototyping and a porous Mg-Zn alloy for several reasons already discussed in Chapter 2.1. Some of the most important reasons are the better adhesion and uniformity of the Hydroxyapatite coating, and the porosity which enhances the bone formation. The two different materials' resonating devices will have different parameters and different thicknesses, that will be simulated to characterize more precise results.

3.1.2 Ion Sensitive pH Sensor:

As previously shown in Chapter 2.1, from the list of ion sensitive materials the one that shows the best and most suited parameters for this study is the nano-particellar zinc-oxide. As also shown in Chapter 2.2.1, there are two ways for which these pH sensors may work depending on the position onto which the ion sensitive material gets deposited, either in the gap of the SRR device or on the surface of the latter.

For this reason, a split ring resonator have been simulated and then fabricated to check the properties of ZnO. Further, since the biodegradable ZnO is in the nano-particellar form, a SRR with an height of hundred of nanometers will be fabricated through e-beam evaporation PVD. Both methods have been employed and two different subsets of resonating devices have been simulated and then fabricated. In Figure 3.2, is shown the structure that have been proposed for the pH study by employing a biodegradable and fully biocompatible ion sensitive material.

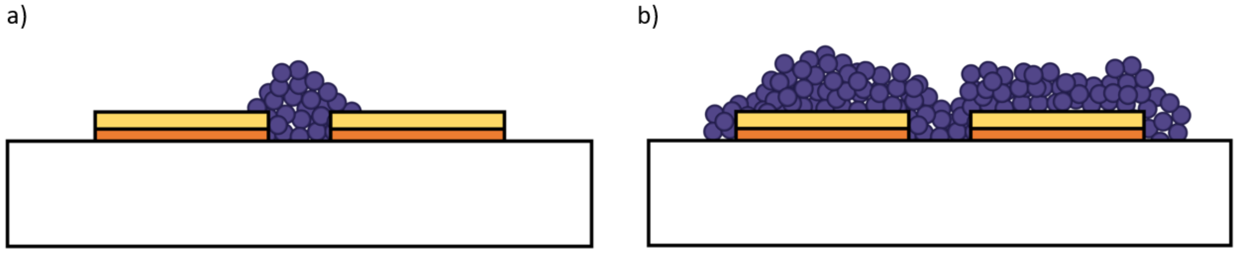

Figure 3.2: Spark ablated ZnO NPs only in the gap and on the overall of the split ring resonating device, respectively in *a)* and *b)*.

The desired structure will be classical split ring resonating devices, but since also the deposition of ZnO only in the gap will be studied, also a "Long-gap" resonator have been studied and reported to increase the dependency of the H^+ ions on the structure overall capacitance.

In Chapter 3.4 will be shown the final described structures, its simulation will be reported then in the results section. In Chapter 5.3.5, instead, will be shown the final fabricated device.

3.2 Strain Detection Resonators

Here there will be shown the basic steps that have been performed in order to get to the final strain sensing device. Initially a double gap split ring resonator, was simulated and tested, such as the one reported in Figure 3.3 a,expecting that the strain induced along the x axis of its substrate would cause a regardable resonance frequency shift. By several simulations, applying displacement between the two rings of the DG SRR, the resonating frequency would remain quite similar to the initial one, making impossible the strain detection.

Most of the cases in literature reports an interdigitated structure, to increase the overall system capacitance variation, that would be induced once a displacement occurs, for this reason a shape like the one reported in Figure 3.3 b, was simulated. Here a huge core will be the considered as a quasi-interdigitated structure around the C like ring. Once a displacement occurs, the overall capacitance vary due to a variation of the gap distance between the big flat sides of the resonating structure. Through simulation this structure was already giving great results, but still resonating at pretty high frequency, around 10 GHz.

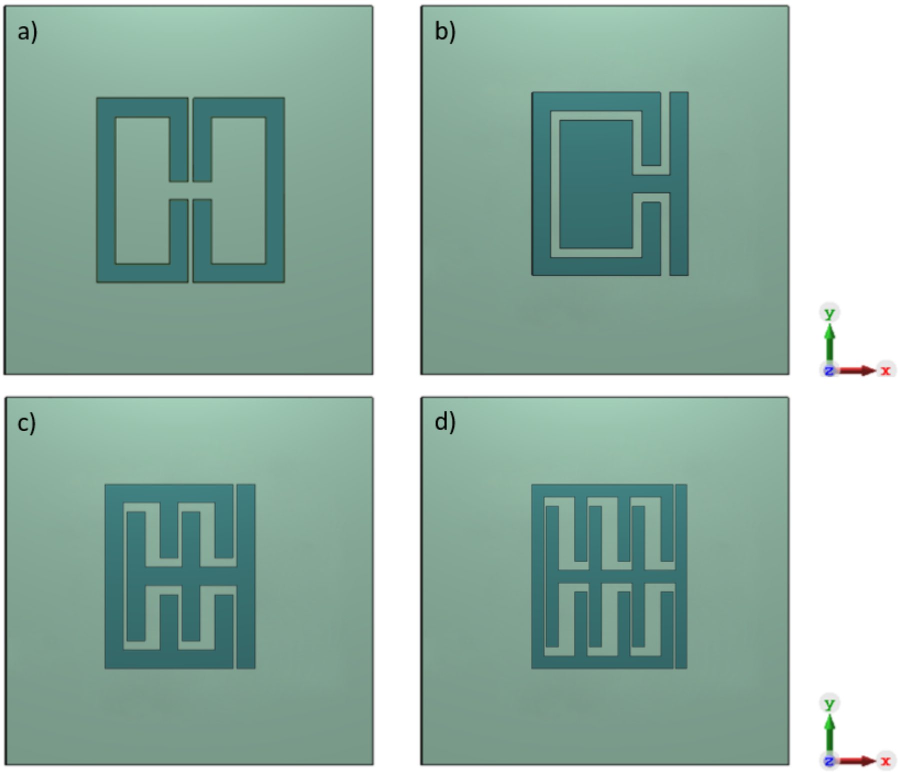

Figure 3.3: Test of the designed strain sensor, in *a)* there is the double gap SRR; in *b)*, in *c)* and in *d)* are reported the single, two the three slit interdigitated structures, respectively.

To reduce the overall resonance frequency of the device a more interdigitated structure have been studied and simulated. The structure in Figure 3.3 c, even though is not the one with lowest resonance frequency, is the one chosen for this project only for fabrication reasons, since it would be easier to be fabricated through the two different fabrication methods that will be described in the following chapters. The other structure reported in 3.3 d gave the best resonating results, allowing the overall resonance frequency of the order of 5 GHz, but it would have been harder to reproduce.

3.3 In-Human Simulations

In this chapter a small discussion about the properties of the human tissues will be described. On the software employed for the simulation, CST Microwave Studio, there is already present the Voxel plug-in data, which has human like tissues and is possible to simulate the overall human body. In Figure 3.4, it is reported the whole human body that can be imported.

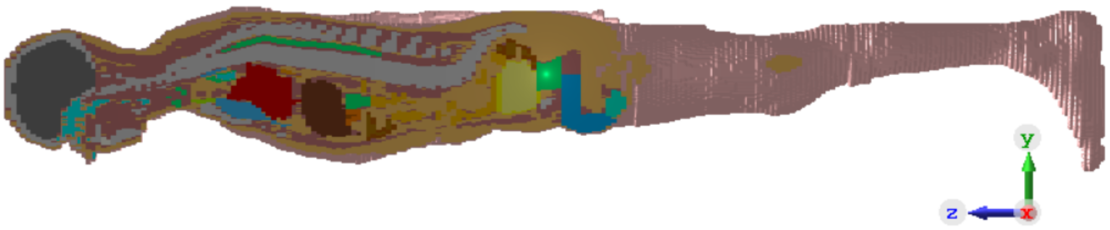

Figure 3.4: Cross-section view of the Voxel human "Gustav" data.

It is important to note that the human tissues absorbance, transmission and reflectance of electromagnetic waves varies on frequency. The amount of wave that will not be able to reach the target first and get scattered back to the monostatic antenna, tends to increase by increasing the resonance frequency of the device. For this reason the resonance frequency of the device has to be optimized to be as small as possible, to allow the resonator to work in the sub tens of GHz, or even better in the sub GHz range.

In Figure 3.5 a, Yessar et al in [75] show how much the human tissues will affect the penetration distance of the electromagnetic wave, showing the importance also of reducing as much as possible the working frequency. In Figure 3.5 b, instead, is reported another key aspect which rely on the so called *skin effect*, where at higher frequency the EM wave will tend to travel less inside the human tissue and will tend to propagate on its surface, making harder the detection of the implanted device.

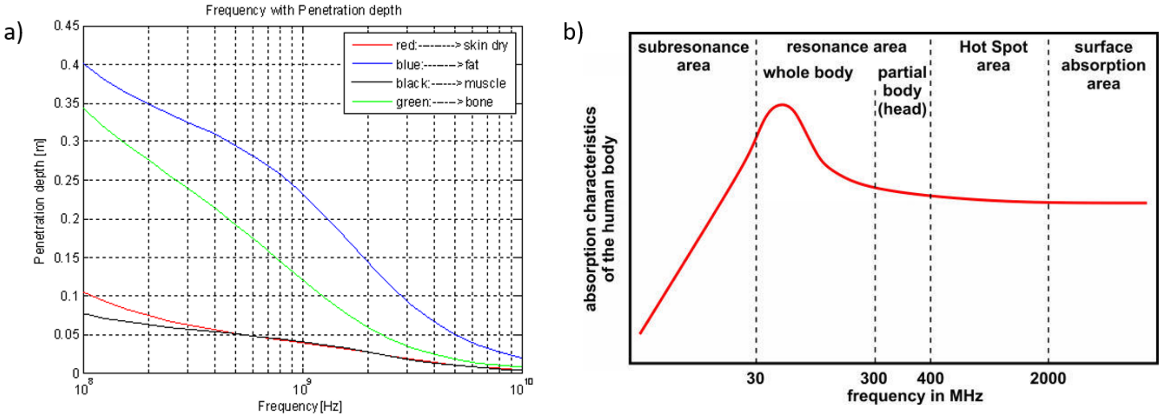

Figure 3.5: In *a)* the relation to the penetration depth and the frequency of the impinging wave, from [75]. In *b)* the absorption characteristic of the human body, from [76].

3.4 Final Design

To sum up all the steps previously discussed about the optimization of the sensing resonator and its device, a brief conclusion of this chapter will take place.

First will be shown the final structure of the pH sensing device to be employed with a pH resistive material. In this case as previously stated in Chapter 2.2.1, only when the pH level drops below the HAp threshold, the resonating device will start to degrade.

To allow the detection of the pH level with this method, a double split ring resonator, or *DSRR*, has been employed. Due to fabrication limitation, the final shape that will be composing the double split ring resonator will be the square one. In Figure 3.6 a it is reported the structure that has been simulated through CST Microwave Studio and subsequently fabricated in magnesium. In Chapter 5.2, there will be shown the resonant frequency of the devices, and how it varies once it gets inserted into a polymer like substrate, shown in 3.6 b.

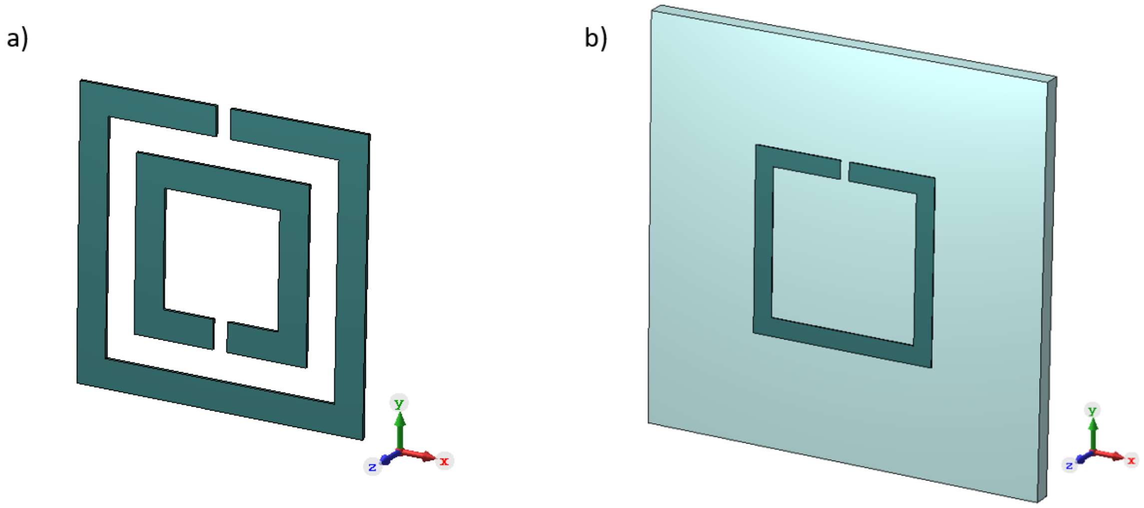

Figure 3.6: Structure of the simulated DSRR before, *a)*, and after POMAC coating, *b)*

Further to allow only one resonator to be in contact with the environmental pH, a coating of a biodegradable polymer would have been employed. Thanks to that only the inner ring will be in close contact with the solution and react, while the outer one will continue its operation, until the polymer gets degraded and becomes itself the sensing device. In the following figure it is shown the idea behind the device fabricated, with the lamination layers made of *POMaC*, employed as biodegradable polymer.

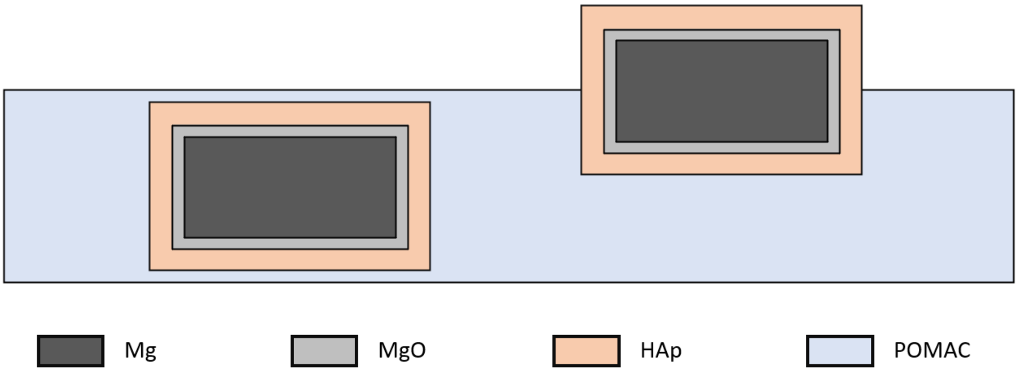

Figure 3.7: Sketch of the concept idea behind the final pH sensor structure.

Now a focus on the second detection method based on Zinc oxide as biodegradable pH sensitive material will be reported. To allow its study a Chromium/Gold and Tantalum/Platinum deposition will be performed in Chapter 4.2. Then a deposition of zinc nanoparticles will be performed which will induce a shift of resonance due to its relative dielectric constant. The structure simulated and fabricated to allow this study are reported in the following. In Figure 3.8 a, is shown a simple split ring resonator device, while in Figure 3.8 b, it is reported the final structure, consisting of a "long-gap", making it more sensitive to variation of gap capacitance.

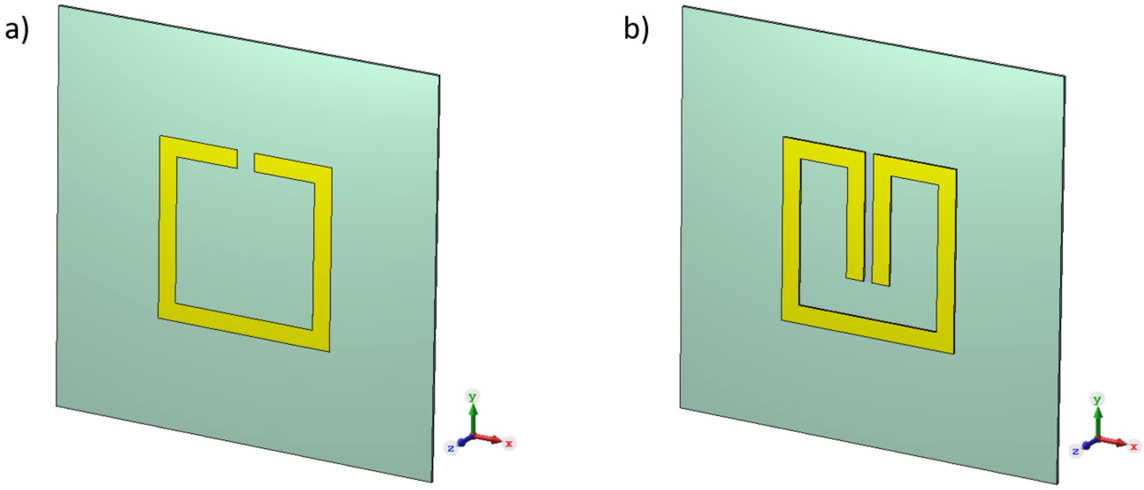

Figure 3.8: Structure of the simulated golden Split Ring Resonator for ZnO pH sensitivity.

Both these structure will be studied in the following chapters, with a more specific focus on the "long-gap" structure. Further two different studies will be performed depending on the deposition of the zinc nanoparticles either on the overall structure or only on the gap of the resonating device.

For what concerns the Strain sensing device, the structure decided to study is reported in the following figure. Once a stress gets applied along the positive x-axis the left structure will be shifted more than the bulkier right one, inducing hence a displacement between the two structures. This shift, will provoke a variation of the resonance frequency of the determined structure. In Chapter 5.2, there are shown the results of the above mentioned structure once a displacement takes place, and further a COMSOL simulation to show how much displacement the structure is going to be subjected.

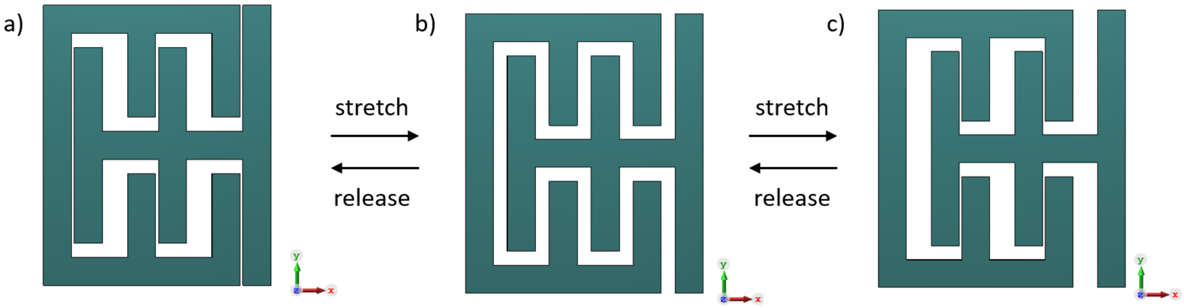

Figure 3.9: Simulated structure of the strain sensor, variation of resonance peak due to the displacement induced by the stress.

Finally, for the in-human study, thanks to the VOXEL human tissues data, already present in CST, it has been possible to simulate how the structure was meant to behave once inserted in the human body. In the following there will be reported a figure showing how the final structure looks like. Since the structure was meant to be studied in the far field regime, the resonance frequency peaks were hard to be detected due to the huge amount of noise. Therefore, to reduce the weight of the simulation it has been reported only the behaviour of the resonating device under a layer of human muscle, to asses its detectability.

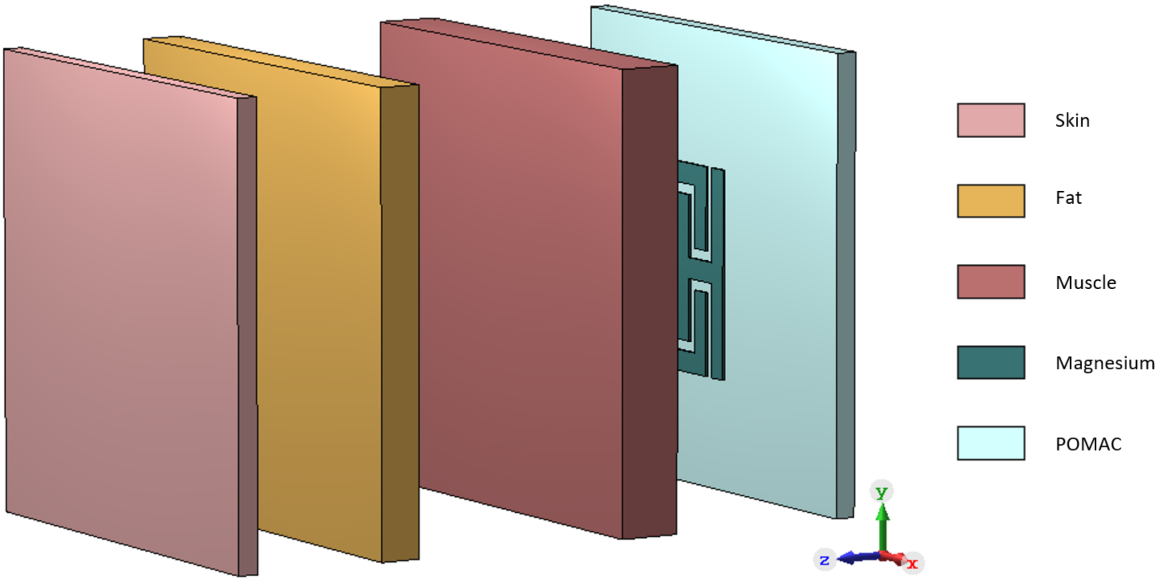

Figure 3.10: VOXEL human tissues on top of the resonating device.

Chapter 4

Fabrication

In the project excursus, several different fabrication methods have been performed, to initially fabricate the first prototypes and subsequently manufacture the final structures.

The first method here reported is based on blade cut samples from pure Mg foils through the "Silhouette Cameo 4". This method was meant to prototype the first Mg based resonator, and to test the several coating techniques employed. The main drawback concerning this method, that will be further discussed in this chapter, was regarding the material employed, pure Mg has several drawbacks once tested $in - vivo$.

The second one is concerning the fabrication through electron beam evaporation of metals through the "CHA Smart Solutions". The main goal was again the prototyping for the proof of concept for the pH sensor with an ion sensitive layer, ZnO, in between the gap or on the whole structure. It is expected a direct shift of the resonance peak dependant on the concentration of H^+ ions in the environment, which would bind on its surface.

Then, the 3D extrusion print of Mg-Zn lines to fabricate Split Ring Resonators will be described. Here a Mg alloy ink have to be prepared by mixing the pre-alloyed powder with a polymeric binder. After the preparation of the paste, the latter will be extruded through the GeSim bio scaffolder 3.2. Finally, a heating process through tube furnace takes place. The heating process has two main intentions, first the debinding, the removal, of the polymeric material from the 3D printed sample, and the sintering of the structure, which would later be discussed in this chapter.

An overview on the hydroxyapatite coating will be described, focusing on the two different approaches employed during the thesis work. This is the most important “fabrication” step since it allows the magnesium-based structure to degrade slow enough to allow the sensing *in vivo*. Then ZnO nanoparticles deposition through spark ablation will be discussed to show how they are formed and the overall "printing" process will be taken into account. Finally the POMaC synthesis will be briefly discussed, since it will be employed as an elastomeric material for the coating of the magnesium based structures previously fabricated.

4.1 Blade Cutter

The first employed method described will be the "Silhouette Cameo 4". It consists of a blade cutter with several different tips that will be chosen depending on the material that has to be cut through, and is reported in Figure 4.1.

Figure 4.1: Blade cutter Silouhette Cameo 4, [77]

The blade cutter have been employed to cut through magnesium foils to allow the reproduction of the resonating devices previously described. Since Mg is a temperature-wise delicate material, the blade cutter was one of the few available methods for shape reproduction. For instance, a laser cutter may have induced explosions due to the low melting temperature and high evaporation rate of magnesium.

Several steps were employed to accomplish the cutting of the magnesium foils. The most important one was relying on the choice of the right blade to allow a correct shape reproduction and the complete demolding of from the foil. Thanks to the "Silhouette" software it is possible either to design the shape that has to be cut through the material, by shape forming, or by import an external file, the latter usually were leading to a better shape reproduction. Then the material properties have to be changed since the material chosen was not already present in the software. Here several trials were necessary to make possible the cut of the magnesium foils. The main parameters that can be modified are:

- The blade depth, which consists on how much of the blade will try to penetrate inside the material, if this parameter is too high, it will induce some damages on the mat employed as substrate, and ruin the foil.
- The speed and the number of passes, which dictates the quality of the cut depending on how fast and on how many cutting passes will take place.
- The force that will be applied from the blade on the material which would help the cut but also introduce some external stress. If not perfectly optimized, it may lead to some damages on both the blade and the material.

Finally, it is important to mention that even though the cutting process was reliable, sometimes the blade were not completely cutting through the foil on the angles of the structures. It may be induced by the not unique cut line that the blade performs to dice the final shape, leaving some connection points uncut. To allow the complete demolding of the structure from the foil a surgical bistoury was employed to apply pressure on the edges, hence some imperfections in the cut will be induced. These will not induce any important variations in the electromagnetic study but may affect the well-being of the hydroxyapatite coating on the pure magnesium samples.

4.2 E-Beam Evaporation

This fabrication process has been employed to have some fast prototyping of split ring resonators to allow the study of the spark ablated zinc oxide nanoparticles dielectric and their ion sensitivity properties. This method was mandatory since a relatively low thickness of the resonating device was needed since the maximum thickness of zinc oxide nanoparticles that could be obtained in were of the order of few hundreds of nanometres.

Since the resonating device were meant to be reproduced on top of small substrates, and since no masks were present, a fully photoresist based lithographic step was not performed, hence a stencil mask was employed. This method relies on the deposition of polyimide on top of a glassy substrate that would later get cut, making only the wanted shape to be exposed to the deposition. The final step is the removal of the polyimide layer either by manually stripping, or by immersing it into an acetone ultrasonic bath for a couple of days. In Figure 4.2, it is shown a sketch of the processes performed to gather the final resonating devices.

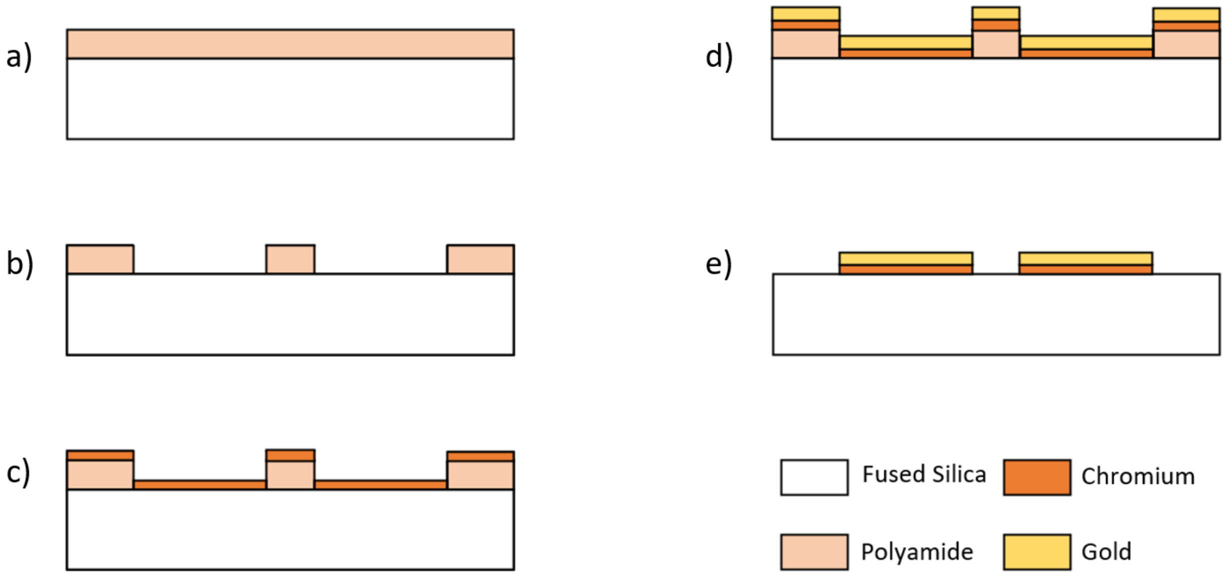

Figure 4.2: Stencil mask process for SRR fabrication. The process consists of deposition of polyimide *a)*, then the patterning, *b)*, through Cameo4. In *c)* and *d)* there are the two deposition steps of Chromium and Gold, and finally in *e)* the stripping of the polyimide mask.

The machine employed for the evaporation is the CHA Smart Source Solution, which is based on the electron beam evaporation. In few words, an electron beam gets produced on the bottom of the crucibles and gets turned thanks to magnets. This curved beam, will then collide with the material inside the crucibles heating it up to its melting point. At its melting temperature, T_m, some of the target material's native ions will be floating in the chamber and eventually deposit on the substrate. Thanks to a piezoelectric material, it is possible to characterize live the thickness of the deposited layer, allowing the machine to have a feedback loop.

The fused silica samples will get patterned through polyamide that gets deposited and patterned through the employment of the previously mentioned Silhouette Cameo blade cutter. This process will allow the reproduction of square like split ring resonator holes on polyamide layer. They get cleaned into an isopropanol and deionized water baths, then dried with a nitrogen gun. Now the samples can be taped on top of a silicon wafer before getting plasma treated. This treatment into a Tepla 300 plasma processor, was needed to remove any excess of carbon present on top of the glass substrates. These wafers will be positioned inside the CHA Solution, to have the metal deposition. The general process consists on the deposition of five to ten nanometres of an adhering layer, such as Chromium or Tantalum in this case, which will allow a better deposition of the top taller layers, fifty to one-hundred-fifty nanometres which will be the final metallic structure, like Gold or Platinum.

Two different material combination have been studied, which are here reported, describing also the thicknesses employed for each layer of the stack.

The first one is the Tantalum/Platinum split ring resonator, which was fabricated through the deposition of five nanometres of Tantalum and fifty nanometres of Platinum. The thicknesses were maintained low since the materials used are quite expensive but also due to the extremely high melting temperature of Tantalum, $\sim 3020°C$, and of Platinum, $\sim 1768°C$, which would lead to a significant temperature rise inside the chamber.

The second material combination was the Chromium/Gold set, manufactured by depositing ten nanometres of Chromium as adhesion layer, and one hundred to one hundred fifty nanometres of Gold. For this set, two different thicknesses were performed to test how the coverage of ZnO nanoparticles would affect the resonance frequency.

Both Platinum and Gold have been chosen since they are not oxidizable into water at ambient conditions allowing a good study for the properties of the zinc oxide as ion sensitive layer. In this same chapter, there will be described the process of spark ablation that will allow the deposition of zinc nanoparticles on the split ring resonator and/or in the gap of the SRR, that would later be annealed to allow its oxidation.

4.3 Additive Manufacturing of Mg-Zn alloy

The creation of the resonating devices with this method has been performed in the 3ME, Mechanical, Maritime and Materials Engineering, department. Here additive manufacturing of Mg-Zn scaffold was performed to realize the resonators designed in Chapter 3. As previously stated, the additive manufacturing of magnesium-based alloys, has been really challenging for several reasons due to its ease to oxidation and its high vapor pressure. One of the methods that has encountered more success for the fabrication of magnesium-based scaffold has been the Solvent-Cast 3D printing which will be here discussed.

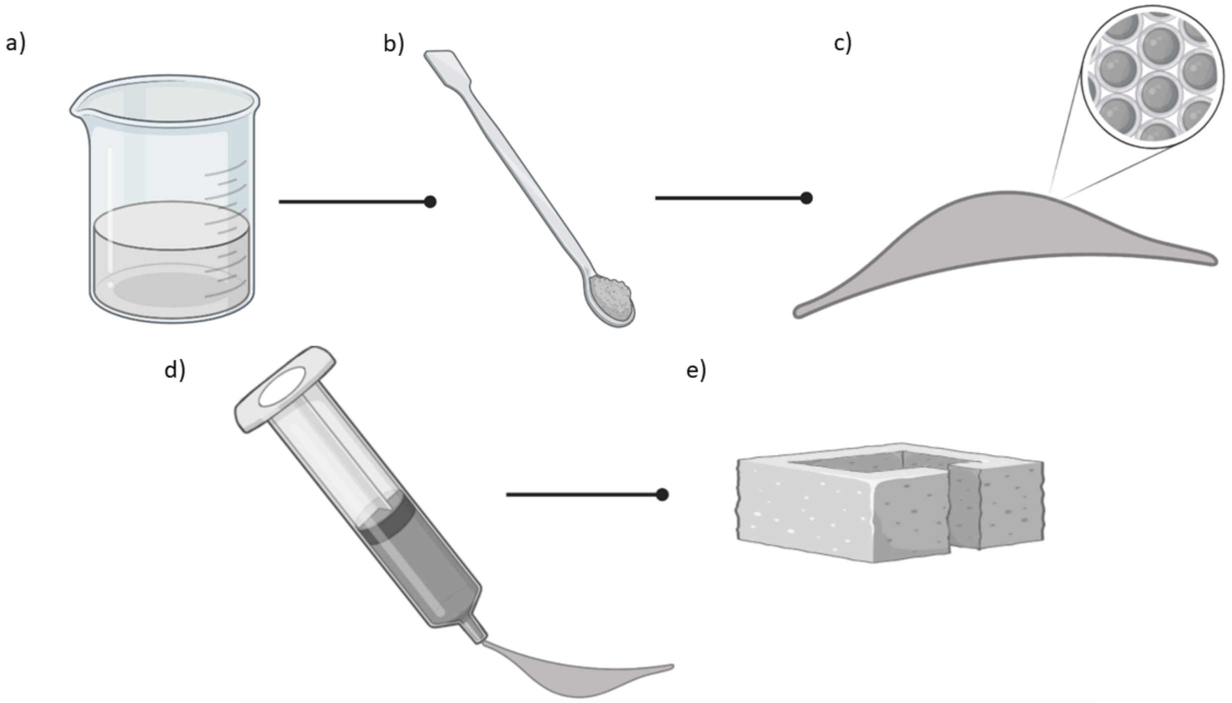

Figure 4.3: Mixing of MgZn powder inside a PIB solution, *a)* and *b)* to obtain a paste of MgZn microparticles coated by PIB connected each other, *c)*. This paste will be "printed" through pneumatic microextrusion, *d)* and will be sintered to obtain the final device *e)*.

The overall process for the fabrication of the resonating device is reported in Figure 4.3. In a nutshell, the Mg-Zn powder gets mixed with a polymer, the binder, to prevent its oxidation once in contact with oxygen molecules. It will also act as a glue to bind all the magnesium microparticles together allowing the powder to remain in place, Figure 4.3[a to c]. Then the extrusion of the paste, through the employment of a GeSim bio-scaffolder, allows the reproduction of the needed shapes, Figure 4.3[d and e]. Finally, the debinding and sintering process can take place, a mandatory step to remove all the binder and then to melt and sinter the powder, creating a conducting path between the different particles.

The method employed to sinter the device is based on the employment of a tube furnace, which relies on the heating up of the samples while a constant flux of argon drugs out the evaporated binder. Another method, described by Lee et al in [78], is based on a chemical room temperature sintering. It consists on the employment of an acid to dissolve the binder, assisting the release and the capturing of the Mg or Zn ions from the microparticles, inducing a conducting path. This method was not performed due to a lack of time.

4.3.1 Ink Preparation

The main equipment employed for the paste preparation were a fume-hood, for the preparation of the PIB solution and the paste, and a glove-box, for the mixing of the Mg-Zn powder with the binder. First, PIB solution was made by mixing polyisobutylene with a molecular weight of 500'000 with hexane as solvent until the right viscosity gets reached. Then this solution get stored into the fridge to increase its shelf-life.

The paste is a solution composed of a weight ratio of 2.8:7.2 of binder and Mg-Zn microparticles. The first step is the weighting of the PIB into a beaker, under the fume-hood to reduce its exposure to the outer environment and the evaporation of the n-Hexane. It is important to note that the n-Hexane will evaporate at room temperature and ambient condition, it is extremely toxic if swallowed or if enters airways, causing damages to organs and to nervous system if prolonged exposure.

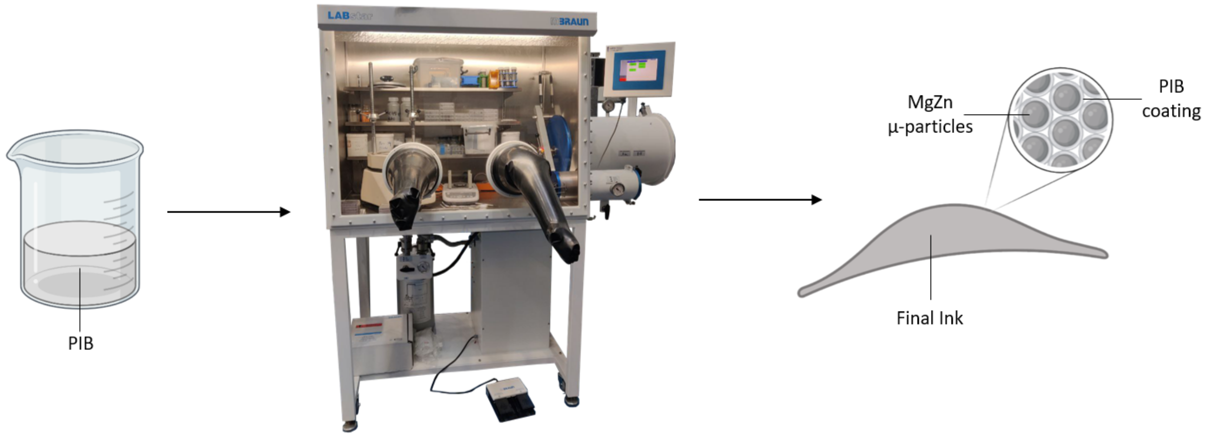

Figure 4.4: From PIB solution, to the LabStar glovebox, where mixing occurs due to the low oxygen presence, to the final printable ink.

After the weighting step, the beaker gets sealed and introduced into a BRAUN Lab Star glovebox, reported in Figure 4.4, to add the Mg-Zn powder. The sealed beaker gets inserted in the loading chamber of the glovebox, then some vacuum and Argon filling steps will take place several times to allow the removal of most oxygen particles. The glovebox pressure is below $5mbar$, with as low as possible oxygen molecules ($< 10ppm$) and water particles ($< 1ppm$) in the environment, to reduce the reactivity of the magnesium powder. The presence of them will induce a faster oxidation of the Mg and Zn particles, loosing its ability to sinter.

By employing a KERN PFB weighting scale, the Mg + 4% Zn alloy gets weighted, added to the binder and fully mixed to create a paste. Once taken out of the glovebox, the loading chamber gets pressurized and vacuumed to further remove the presence of oxygen inside the tray for the future users. The final step is the addition of n-Hexane since part of it have been evaporated, changing the composition of the overall paste. By knowing the expected weight, it is possible to get how much of the n-Hexane has been evaporated from the beginning of the process. The same quantity plus a small percentage of the solvent gets added, that will evaporate during the mixing step. Then, the paste is inserted into a large syringe to allow the printing through the Bio-Scaffolder 3.2. It is important that the syringe is filled without any air gap in between the paste to allow an overall reliable printing of the structures.

4.3.2 Extrusion

The syringe filled with the paste gets inserted in the GeSim Bio Scaffolder 3.2, in Figure 4.5 a, which is based on the pneumatic micro-extrusion printing. Figure 4.5 b, shows the different type of microextrusion printing. A perfectly tuneable Nitrogen flow pushes, from the back, the ink, allowing a constant extrusion speed of the material from the syringe nozzle.

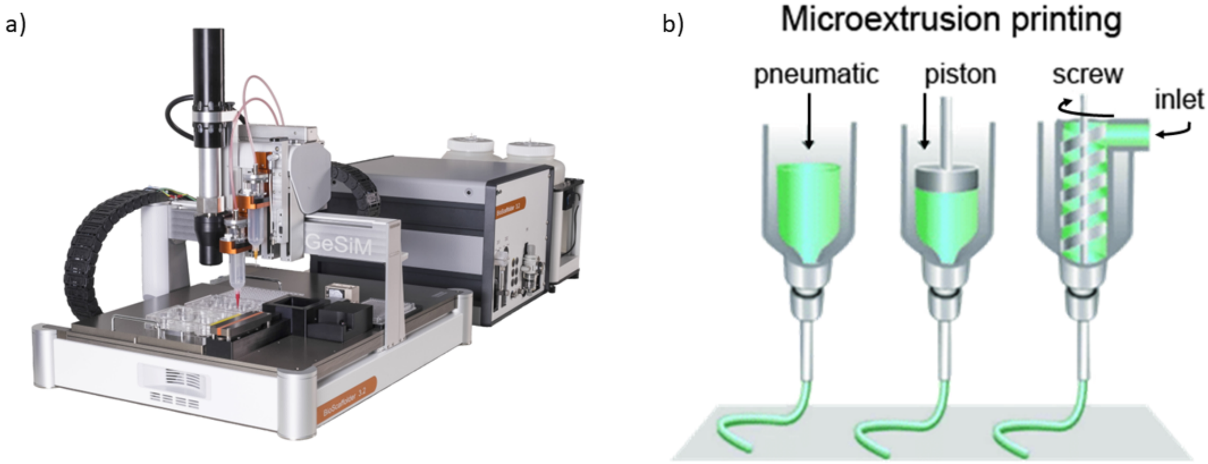

Figure 4.5: Gesim Bioscaffolder 3.2, used for the ink extrusion, is reported in *a)*, [79]; the different type of micro-extrusion printing are reported in *b)*, [80].

After the ventilation system has been turned on, the syringe with the ink gets inserted in the machine. A tube will be fixed in the back of the syringe, allowing the Nitrogen flux to constantly extrude the ink. Glass slides will be positioned on the printing plate, initialized on the machine to make it understand where to print. After the calibration of the tip along the z-axis, an high pressure is forced to the back of the syringe for two main reasons: first since the first time the paste will face stronger forces opposing its extrusion, like stiction, surface tension or friction; and second since closer to the tip most of the solvent will be evaporated and the paste will be less viscous. Before the real printing can take place, the optimization of the parameters will take place. The *Extrusion Pressure*, is the pressure that applied on the syringe back to have the coming out of the ink, it usually ranges from 115 to 140 kPa for the 580μm nozzle. The *Syringe Speed* is dependent on the extrusion pressure, and is the speed at which the syringe will move, usually in the range of 2.0 to 3.5 mm/sec. The *Strand Width* consists on the width of the nozzle selected, the 580 μm and the 410 μm nozzle tips. The *Start Break* is the time before the syringe starts to move, while the pressure is applied. It is important to have the a good adhesion of the paste on top of the substrate, set to 0.8 sec. And finally the *Strand Distance* which is the distance between two printed lines, but since the goal of the project is to create structures as uniform as possible, to reduce parasitic capacitances, its value will be set as 0.200 mm.

After choosing and optimizing each one of these parameters, depending on the viscosity of the paste, the real printing can occur. Here an ".stl" file can be imported, previously designed on SolidEdge, and the printing can start. After the printing ends, several minutes have to pass before demolding the samples from the glass slides to allow all the n-Hexane solvent to evaporate, both for health protection and to make the printed samples stiffer.

4.3.3 Sintering

To obtain the final conductive structure a sintering process is needed. Two different furnaces will be employed and in the results section the outcome of both will be discussed. Part of the thesis project was on the optimization of the sintering process for both machines.

This high temperature sintering step is mandatory for two main reasons, to remove the binder from the extruded samples and to make the creation of a conductive path between the different particles. It will remove the PIB from the structures, leaving only the magnesium-zinc alloy which will be slightly melt down to bind between each other, creating a conductive path. Not only the temperature, the pressure and the gas flux will affect the sintering process, but also the crucible material, where the magnesium samples will be placed, has a role in this step. The magnesium-zinc alloy samples will be placed on top of a Boerum Nitride, BN, crucible before sintering, which is non reactive to oxygen and to the samples taken in consideration.

- **Xerion X.RETORT Furnace**

The first furnace used for sintering is the Xerion X. Retort and is reported in the Figure 4.6 a. The cooling system of this furnace is based on a water flux on the front door, which ease the opening of the door after the heating process. To avoid a huge amount of binder to reach the furnace door, some metallic rings are inserted between the chamber and the door.

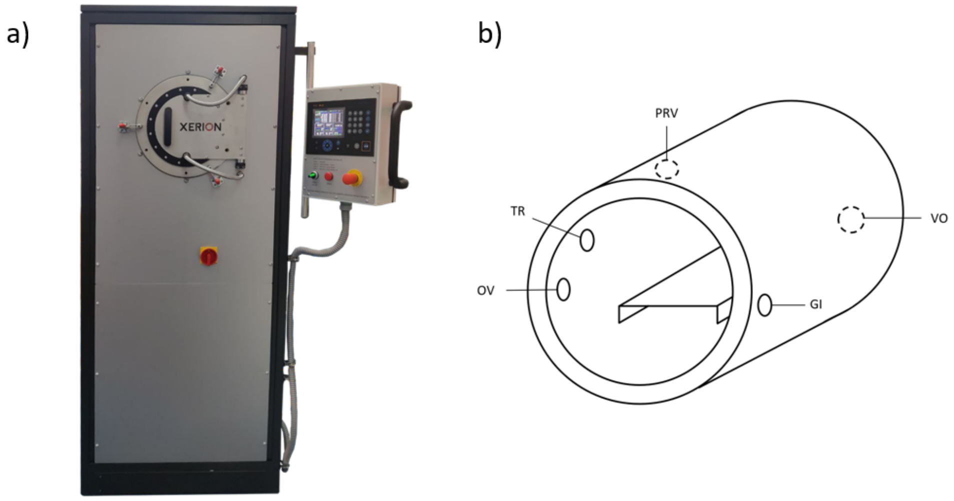

Figure 4.6: *a)* Xerion X.RETORT furnace overview, *b)* X.RETORT sketch

From the schematic shown in Figure 4.6 b, several inlets and outlets are depicted. *GI* is the Gas Inlet, from which the selected gas, in this case Argon, will enter and fill the chamber; *VO* is the Vacuum Outlet, where the vacuum will be activated drugging out also the binder that gets removed from the samples. *PRV* is the Pressure Release Valve, that opens only once the chamber pressure overcomes the 1150mbar threshold; *TR* is the Temperature Recording, where the temperature gets measured; finally *OV* is the Overflow Valve, that opens only when a pressure above 30mbar is reached in the chamber. In the Vacuum Outlet there is a cold trap to catch all the binder residues that gets drugged out from the samples, hence a flux has to be created from the Gas Inlet to this outlet. Other paths have to be avoided due to the absence of cold traps which will induce the binder to stick on the pipes of the machine, blocking the correct functioning of the furnace.

The process used for this machine is here described. The crucible is inserted into the chamber, close to the Gas Inlet, to allow the sample inside the flux that will be generated, as previously mentioned. The metallic multi-ring structure is inserted in the furnace and the front door gets closed through vacuum sealers.

First a run to check the correct functionality of the machine takes place, which consists on the use of every machine adds on, heating, vacuum, and gas insertion of Argon and Argon + Hydrogen. Several runs have been performed during the project time period, to characterize the most suited process, that have not resulted in a perfectly sintered sample.

First, flushing step takes place, to remove all the air present in the chamber. To perform it four steps of vacuuming, until $10_{-3} mbar$ are reached, and Argon filling, with $75l$, will take place. Then the temperature will start to rise up until 420°C while filling the chamber with Ar. While further increasing the temperature of 15°C per step, vacuuming and argon filling will take place until the overall internal temperature reaches 540°C. At this point, it is supposed that most of the binder has left the chamber, hence no more vacuum will be activated. The chamber gets filled with argon, and a temperature of 630°C gets reached and maintained constant for one hour to perform the sintering.

- **Carbolite Gero Tube Furnace STF 16/180**

The second optimized furnace is the Carbolite Gero STF 16/180, reported in Figure 4.7. It consists of four heating elements in series inserted into an insulating material, to reduce the heat dissipation. In the center of this insulating material, a hole will host the ceramic tube onto which the samples will be loaded on a Boerum Nitride boat, that will be pushed up to the middle of the machine. At the two edges of the machine two ceramic insulating shields will be added to avoid further heating dissipation.

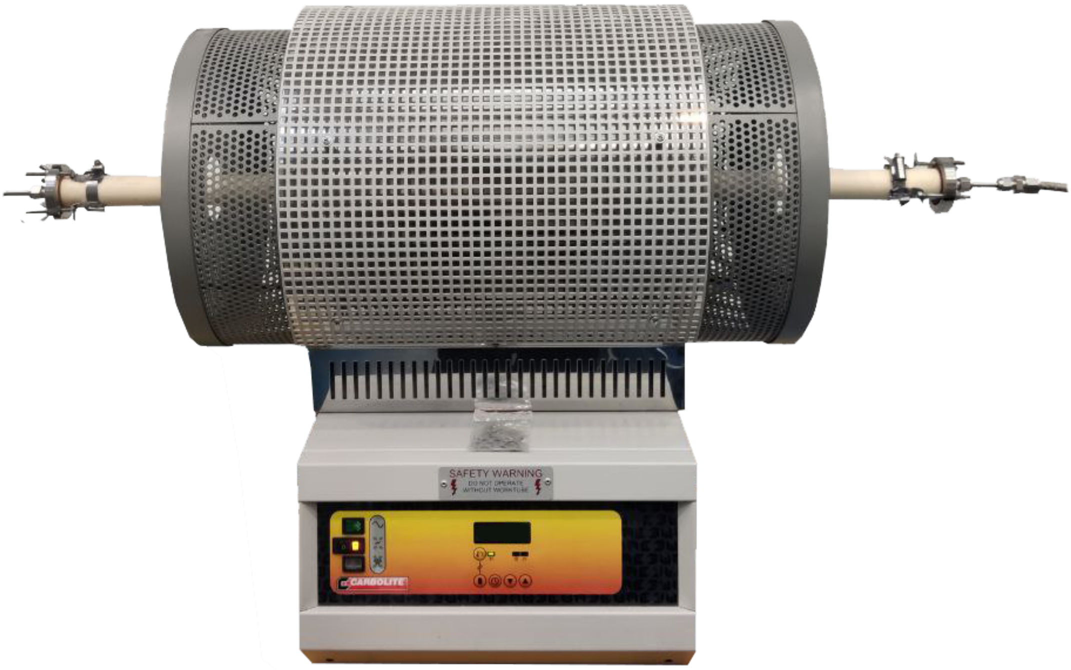

Figure 4.7: Carbolite Gero Tube Furnace STF 16/180

On the left of the furnace a flux of argon will be entering the tube, drugging out the binder, released by the manufactured samples, to the outlet of the tube, on the right of the furnace. Here a cold trap is present to "catch" all the remaining carbon and binder, before entering in the exhaust pipelines. A thermocouple is placed close to the center of the chamber, below the tube. During the project period, the machine broke down several times, and the position of the thermocouple has changed time by time. An optimization and calibration of the measured temperature with respect to the real in-situ temperature was then performed several times.

The process to sinter the magnesium-zinc alloy samples with this machine is here reported.

	Heating Rate (C/min)	Max Temperature (c)	Hold Time (h:m)
Value	5	625	01:00

Table 4.1: Carbolite Process for AM MgZn samples sintering

The good samples and a dummy, used as first on the left to "catch" the argon impurities, are placed on the BN boat, inserted in the tube and pushed to the center of the machine, which is the most thermally efficient region of the furnace. After adding the two insulating ceramic shields on both sides of the tube, and after screwing up the metallic enclosures on both ends, a constant flux of argon will be flushing inside the tube-chamber to remove all the oxygen inside the chamber. As previously mentioned, the presence of oxygen inside the chamber would induce and excessive oxidation of the magnesium-zinc particles, inducing a non correct connection between them.

After one hour of argon flushing, with an heating rate of 5°C/min, 625°C will be reached, and will be set constant for one hour, to have the correct sintering of the extruded structures. If the set temperature is too high, an overmelting may take place, inducing bubbles all over the structures, while if it is too low, it will not "melt" the powder, preventing the creation of a conductive path. Then there is the ramp down of temperature, from the set 625C down to room temperature, and only at this point it is possible to take out the samples.

It is important to note that in the overall process, the Argon flux was maintained constant to allow a correct debinding and the correct sintering of the structures.

4.4 Hydroxyapatite Coating

One of the most important steps to fabricate the final device is the Hydroxyapatite coating of the magnesium samples. In Chapter 2.1, have been shown and discussed its properties and its importance for this study, but its importance can be summed up in the following points.

First it will allow the magnesium alloy resonating structure to not dissolve into neutral pH environment, making possible the in human detection once no inflammation occurs. Second, and most important, the HAp coating decreases the magnesium and zinc degradation of the sintered material, which will further allow the sample to be biocompatible and not toxic.

Two methods have been employed to coat the samples, both rely on the hydrothermal deposition of Calcium Phosphate, CaP, on top of the Mg and Mg-Zn based samples, which is based on the immersion of these samples into a water based solution. The difference relies on the surface treatment in Hydrofluoric acid, HF, for the first method employed to remove the native oxide layer on top of the magnesium based sample. Both methods will be described.

- **Surface Treatment Method**

Here a surface modification takes place to allow a better adhesion of the hydroxyapatite coating on top of the samples surface, as have been demonstrated to be functioning by Dong et al, in [30], for pure magnesium additively manufactured scaffolds. First an alkali-heat pre-treatment takes place, here the samples are added in a 5 molar NaOH solution at 80°C for 24 hours, then cleaned with distilled water and isopropanol. Only now the fluoride conversion treatment can take place. The shapes were immersed in a 40% Hydrofluoric acid, HF, at room temperature for 66 hours, then rinsed in distilled water and isopropanol. Once the surface modification has finished, the hydrothermal deposition can occur, to coat the magnesium zinc samples with CaP. The samples were immersed in a mixture of $Na_2HPO_4 \cdot 12H_2O$ $(9.41g \cdot L^{-1})$ and $Ca(NO_3)_2$ $(26.20g \cdot L^{-1})$ at 70°C for 24 hours, then rinsed in distilled water.

This process has been tested only once for two main reasons, the time needed for one run was taking one week and the overall results after this first run, brought the samples to collapse on themselves. For this reason, it will not be described and its results will not be shown in the results section.

- **Hydrothermal Method**

This method consists on the immersion of the pure magnesium, or the magnesium zinc alloy, samples inside a bath solution of 250 $mmol/l$ of Ca-EDTA and 250 $mmol/l$ of potassium dihydrogen phosphate. In the following the method employed will be described in details, according to what stated by Hori et al in [50] and Hiromoto et al in [41].

The chemicals employed are, Ca-EDTA, Ethylenediaminetetraacetic acid calcium disodium salt hydrate, with the chemical composition: $Ca(O_2CCH_2)_2NCH_2CH_2N(CH_2CO_2Na)_2$, sodium hydroxyde, $NaOH$,and Potassium Dihydrogen Phosphate, KH_2PO_4.

To produce 200 ml of solution, 9.357 grams of Ca-EDTA and 3.4 grams of KH_2PO_4, have been first weighted in two separate beakers and subsequently solved in 100 ml of water each. Then the two solutions get mixed together and stirred well before adding some pallets of sodium hydroxide, NaOH, which is needed to adjust the final solution pH to 8.9. Here either a pH meter or a litmus paper is employed to characterize the overall pH of the solution.

After all the NaOH pallets got dissolved the magnesium-based samples will be immersed in the solution. Here a magnetic stirrer is inserted inside the flask to allow a constant stirring during the overall process. The outlets of the flasks are sealed by rubber lids, to reduce the solvent evaporation. The central aperture will be sealed by a hollow lid to allow a thermocouple to get inside the solution and give a feedback loop to the Joan-lab machine showed in Figure 4.8.

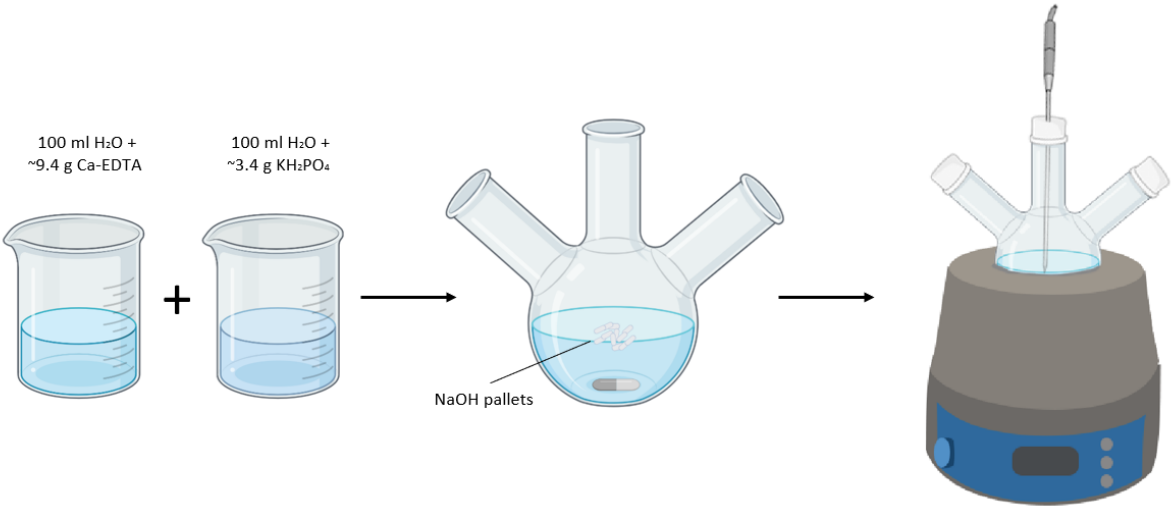

Figure 4.8: Schematics of the Hydroxyapatite coating process.

The heating process can now take place, a slow heating rate is applied to reduce the overheating effect which may lead to evaporation of the solvent of the mixture. After reaching 95°C, both the temperature and the stirring speed are kept constant. For the first run, one sample was taken out of the solution every hour to allow a qualitative evaluation of the HAp coating uniformity depending on the sample's immersion time. It has been seen that after six hours the coating resulted more uniform and conformal on the overall structure.

In the result section, Chapter 5.3.4, the coating will be shown for both the pure magnesium and the additive manufactured magnesium-zinc samples, showing the uniformity of the coating on both samples type.

4.5 Zinc Oxide Spark Ablation

The material that will be employed as ion-sensitive material for the pH detection will be nano-particellar Zinc Oxide, and two different structures will be fabricated as previously described in Chapter 3.1. The machine employed for this scope is shown in Figure 4.9 a, and has been mounted and optimized by the group of Sten Vollebregt at TUDelft. The working principle, described by Pfeiffer et al in [81], is based on the spark ablation of zinc nanoparticles. Sparks gets produced between the two metal electrodes, forming a plasma generating a local temperature higher than 20'000 K. This makes the electrode's material to locally reach melting point creating a vapor plume that gets cooled down by adiabatic expansion and by an inert gas that moves the atoms in order to form clusters, particles, aggregates or agglomerates, as shown in Figure 4.9 b.

The inert gas chosen for this study was Ar with 7ppm of H with a flow rate of 1.5 l/min. Even if with H, the gas is more reactive at high temperatures and lowers the deposition rate of zinc, it reduces the zinc electrodes' oxidation.

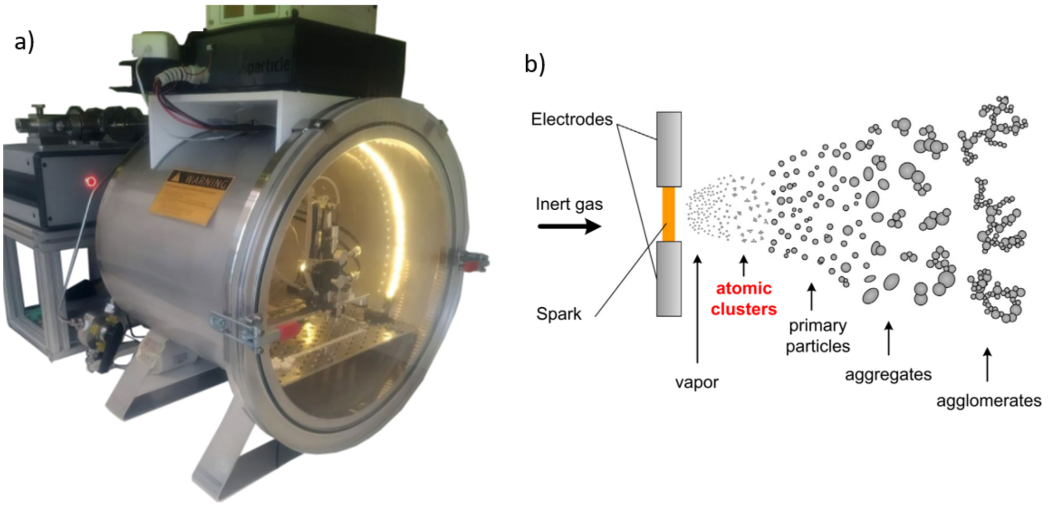

Figure 4.9: In *a)* the spark ablation machine used for the study, in *b)* a sketch of the functioning of the machine from [81].

First the zinc electrodes are put in place, then the gold based split ring resonators are cleaned in acetone and IPA, dried and taped on the machine plate. After closing the chamber door, the operation may take place only once the applied vacuum reaches a value lower than $100 mtor$. By moving the nozzle a rough alignment of the printing spot to the sample surface is carried out, then a z calibration will be performed by choosing the printing distance between the nozzle and the surface, by adjusting the camera focus on the substrate. The x-y alignment will then be performed to print on the target spot by producing a zinc dot through spark and by evaluating the distance between the printed and the targeted position. The spark will get generated with a power of 1kV per 3 mA to have a controllable deposition rate. To allow the printing of the zinc lines, a code containing how much the nozzle has to move along the x and y direction, in mm, and the printing speed, set at 8 mm/min, was written.

After the printing finishes, it is possible to take out the samples and anneal them into the Carbolite AAF 11/7 ceramic oven, at 600°C for 5 hours with a nitrogen flow rate of 0.5 l/min to prevent the detachment of zinc from the substrate before its oxidation.

4.6 POMAC Synthesis

In this sub-chapter the synthesis of POMaC will be described since a biocompatible yet biodegradable material would be needed for the lamination of the resonating structures as previously shown and mentioned in Chapter 3.4. An overview of its synthesis process is reported in Figure 4.10, and will be here discussed.

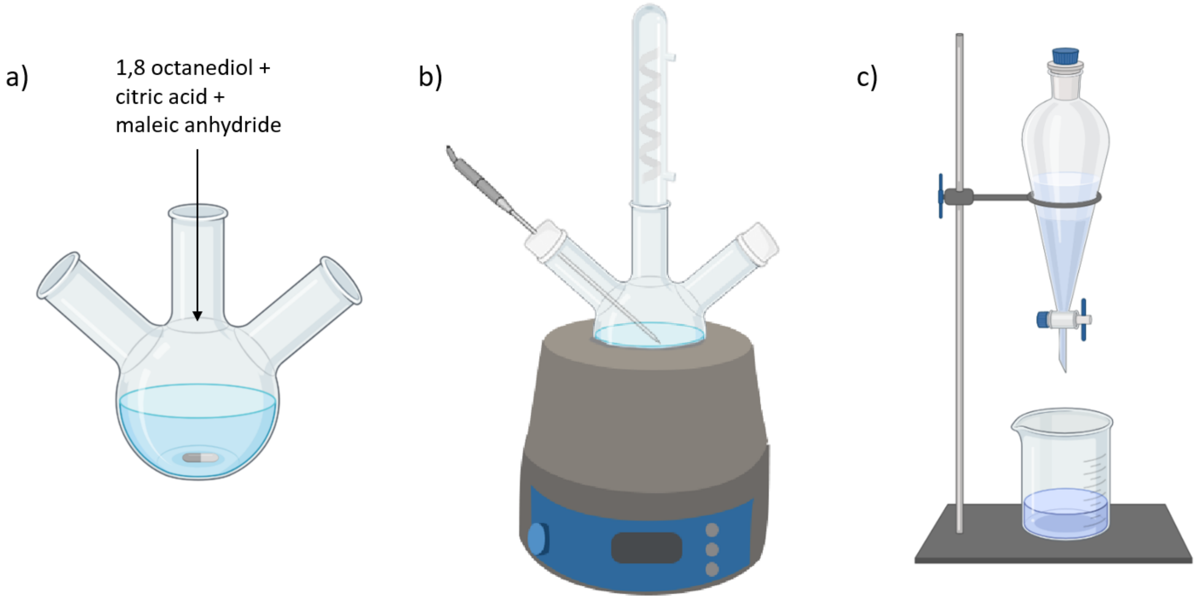

Figure 4.10: Schematic of the POMaC synthesis process.

To synthesise the POMaC several steps has been performed, following [36] and [82]. First, a molar ration of 5:1:4 of 1,8 octanediol, citric acid and maleic anhydride, will be mixed together into a three neck round flask, as shown in Figure 4.10 a. Then the flask will be positioned inside the JOAN-Lab heater, closing each neck by putting a thermocouple on one side, a N_2 flux on the other and a cooling water tube on the middle one, as shown in 4.10 b.

The temperature of 140°C has to be reached and maintained constant for three hours. To avoid overheating, and the evaporation of the solvent, a gradual increase of temperature will take place. Then, the solution will be cooled down before casting some 1,4 dioxane solvent inside it, with a ratio of 1ml of solvent every 1g of solution. After the solution gets well mixed, it can be poured into a separatory funnel, as shown in Figure 4.10 c, on top of a beaker filled with 2l of deionized water. The pure "pre-POMaC" will stay at the bottom of the beaker due to its high density, hence the water can be casted away to have the final solution.

To have the final POMaC solution, the "pre-POMaC" will be mixed with PEDGM porogen with a 2:3 weight ratio, and a 5% weigth/volume of photoinitiator. After mixing the final POMaC solution is ready to be casted into a PDMS, or though PLA, mould that have been previously sylanized to allow an easier demoulding.

The final step is the UV curing, that is performed with a Philips UV lamp. The samples that will be fabricated are $800\mu m$ thick, and to have a complete crosslinking of the material, an UV exposure of 20 minutes on both sides have been performed, in order to obtain the final structure.

Chapter 5

Results

Here the results will be described showing all the outcomes obtained from the study. It will be described at first the simulation results, that have been previously described in Chapter 3. These will be needed to understand and compare the real characterized results to the simulated ones.

Then for each fabrication method employed an overview of their material properties will be reported, with microscope images of the samples, mechanical, and electrical properties. Starting from the Mg foils cut through the employment of the Silhouette CAMEO blade cutter, to the gold evaporation with the polyamide mask, to the additively manufactured and subsequently sintered samples. An emphasis on the hydroxyapatite coating, and on the deposited ZnO nanoparticles will take place for both the magnesium-based samples.

After the material focus of the resonating device, a focus on their electromagnetic properties can take place, the characterization has been performed by employing an horn antenna that will be depicted and described in the following.

Finally, there will be shown the results of the biocompatibility and degradability tests, showing the importance of the Hap coating on these fully biodegradable resonating devices, and after how much time the device will disappear once implanted in the human body.

Before entering into details of the study a small chapter concerning the different characterization equipment will be discussed to ease the understanding of the results shown in the latter.

5.1 Characterization Methods

In this chapter there will be a short overview of the several machines employed for the characterization of the fabricated devices.

- **Fabrication Characterization**

Several equipment have been implemented for characterizing the fabricated samples mentioned before. The Philips SEM XL30 SFEG have been used for the picture extrapolation, while the JEOL JSM-IT100 InTouchScope SEM have been employed for the Energy Dispersive X-ray Analysis. An NT-MDT NTEGRA II modular AFM machine have been used to perform the Atomic Force Microscopy for the Zinc Oxide nanoparticles surface roughness. The dimensions of the e-beam evaporated SRR were confirmed by employing a stylus profilometer, the BRUKER Dektak 150. To perform the X-Ray Diffraction Analysis, the Bruker D8 Discover diffractometer and the Eiger-2 500k 2D-detector was used. A Keyence VK-X250, was utilized for Scanning Laser Microscopy, to characterize the surface and its roughness of the AM MgZn fabricated samples. For the conductivity characterization a Keithley SourceMeter 2634B have been used with some Mueller Electric Crocodile Clip of few mm in size.

- **Electromagnetic Characterization**

To perform this test an Ultra-Wide Band horn antenna produced by Geo Zondas, with a broadband emission range that goes from 1GHz to 26GHz has been employed to characterize the resonance of the split ring resonators in the far field condition present in the MS3 department. A Keysight P9374A Network Analyzer has been employed to gather the results shown in the Chapter 5.4. In Figure 5.1 a, is reported an image of the setup used, to reduce the noise provoked by the environment, several absorbing materials have been employed on the bottom and on all sides of the sensor. A variation of the distance "*d*" between the SRR and the antenna have been performed to test how the device would behave in the different field conditions.

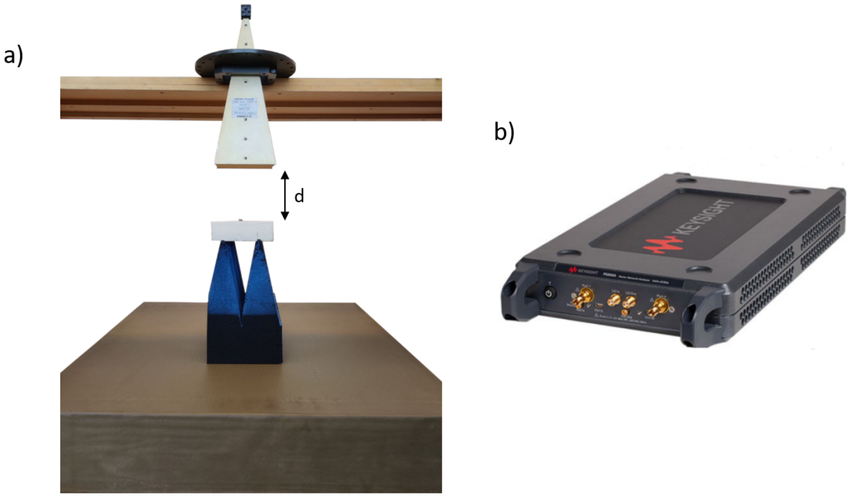

Figure 5.1: In *a)* is reported the antenna setup employed to characterize the samples, in *b)* is shown the Keysight P9374A Network Analyzer, to extrapolate the antenna's data.

5.2 Simulation Results

Here the different simulation results will be depicted, showing the outcomes for each structure described in Chapter 3.4. For each one of them a comparison with the different employed thicknesses will be taken in consideration, which rely on the fabrication method employed.

5.2.1 Ion Resistive pH Detection

The detection method described in this chapter rely on the Ion Resistive material. As previously described in Chapter 3.1, the idea behind this consists on the employment of a material that degrades only when in the liquid environment a certain pH threshold gets reached. The final design chosen is reported in the following figure, and in Table 5.1 are reported its characteristic dimensions, for the final structure laminated into POMAC.

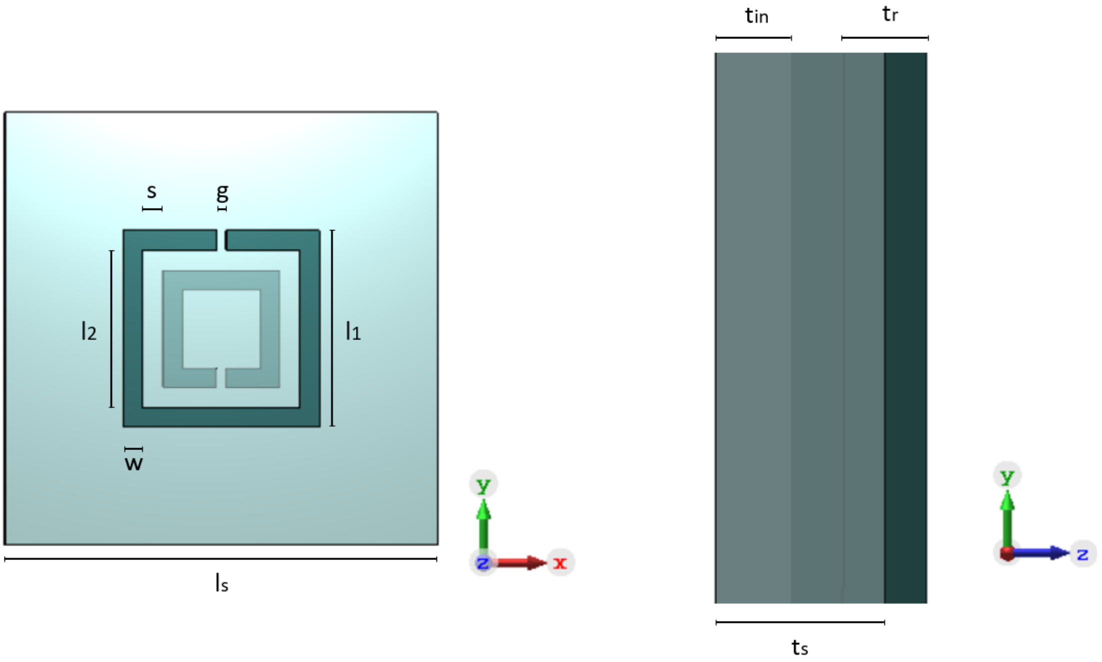

Figure 5.2: Chosen and simulated ion resistive pH sensing structure.

	l_s	l_1	l_2	w	g	s	t_s	t_r	t_{in}
Value	22	10	8	1	0.5	1	1	0.5	0.4

Table 5.1: Double split ring resonator pH sensor dimensions, in mm.

The chosen structure has been simulated from two different magnesium thicknesses since they will be fabricated through two different processes. The simulated thicknesses are $t_r = 500\mu m$ for the additively manufactured samples and $t_r = 100\mu m$ for the blade cut samples.

In the following, Figure 5.3 and Figure 5.4, there are reported the resonance frequency for the above shown structure with and without the POMAC lamination for the two different thicknesses.

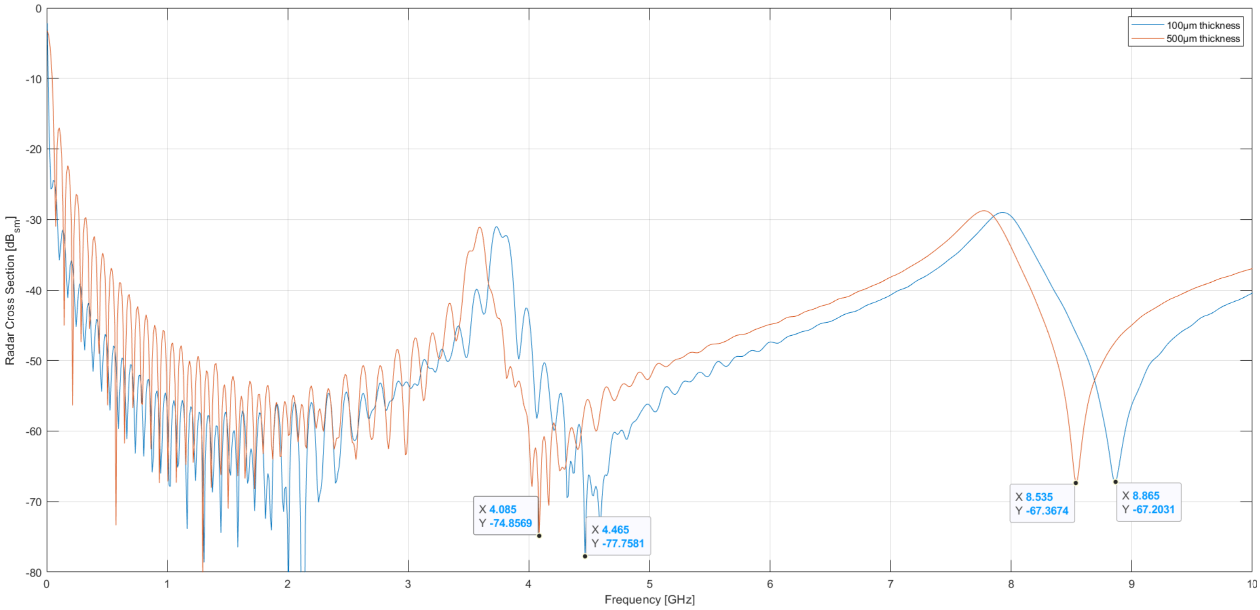

Figure 5.3: Resonance peaks of a double split ring resonator without substrate.

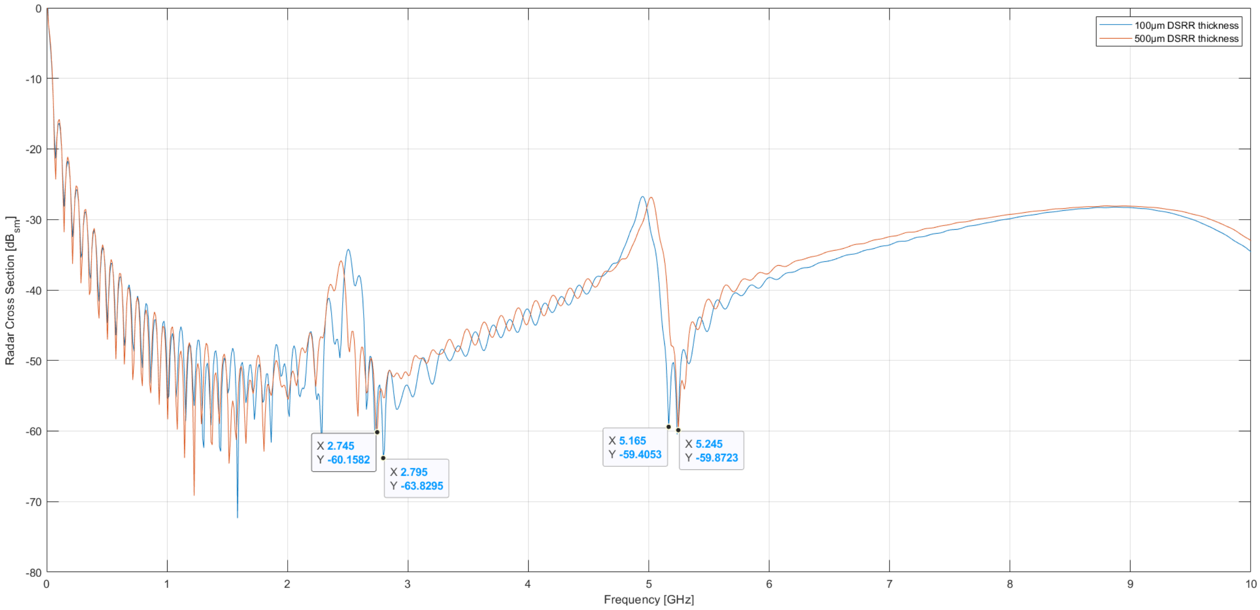

Figure 5.4: Resonance peaks of a double split ring resonator laminated into a POMAC substrate.

5.2.2 Ion Sensitive pH Detection

Here there will be reported the structure decided to simulate for the pH sensing through the employment of an ion sensitive material both on the gap and on the overall surface of the split ring resonator as also shown in Figure 3.2.

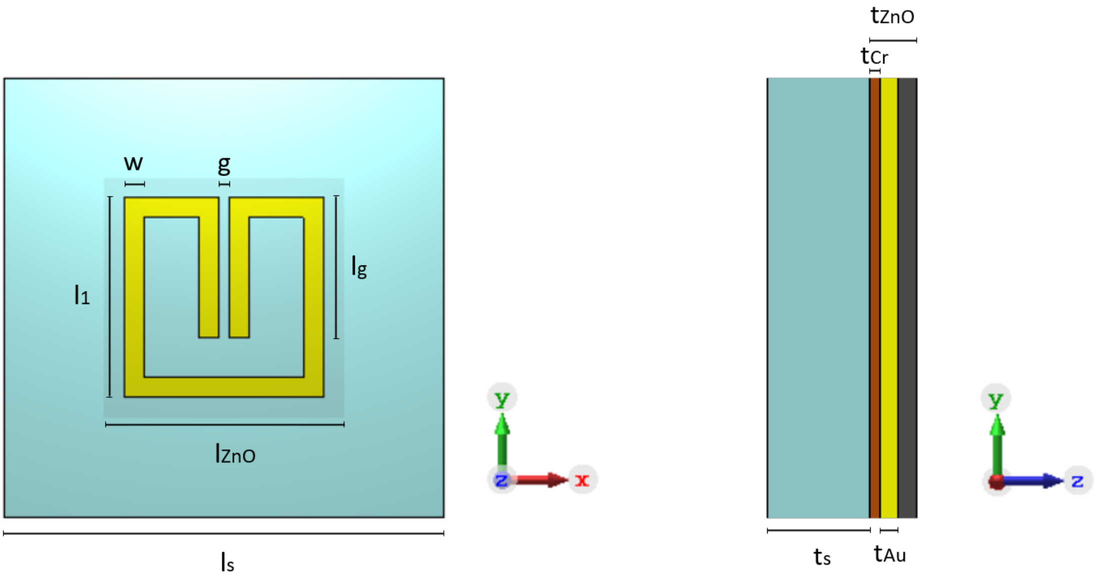

Figure 5.5: Chosen and simulated "Long Gap" ion sensitive pH sensing structure.

	l_s	l_1	l_g	l_{ZnO}	w	g	t_s	t_{Cr}	t_{Au}	t_{ZnO}
Value	22	10	7	12	1	0.5	0.1	5e-5	1e-4	3e-4

Table 5.2: Dimensions of the "long gap" for ion sensitive pH sensor, in *mm*.

Since zinc oxide nanoparticles were not present into the CST Microwave Studio software, glass has been employed as dielectric material, and its dielectric relative permittivity has been changed to the one of the ideal and bulk Zinc-oxide. From [83], ϵ_r is varying in a range from 8.17 to 9.34, so the chosen value was 8.75. In the following there are reported the simulated results for the simple split ring resonator, and for the "long gap" SRR. Only for the second will be shown the variation of the resonance frequency with and without the dielectric material.

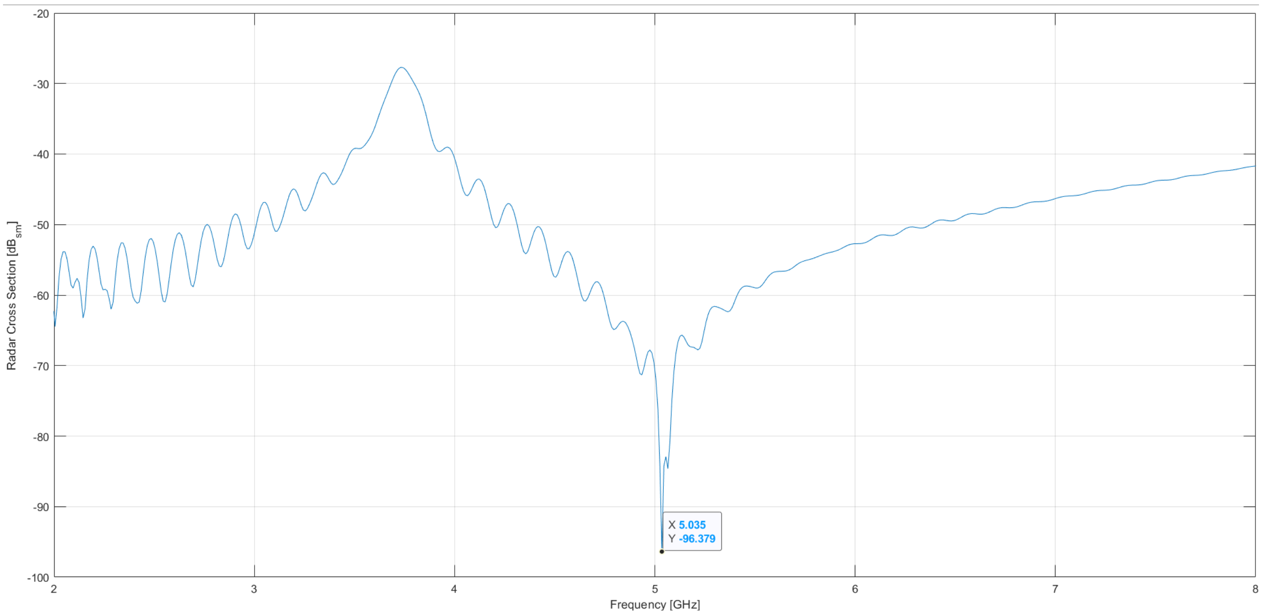

Figure 5.6: Resonance peaks of a "short-gap" single gold split ring resonator.

From the two mentioned structures shown in 3.4, the one that will mostly be taken into account is the "Long gap" structure due to the already small dependency on the resonance frequency from the zinc oxide deposition, as shown in the simulation results depicted in Figure 5.7. Both structures have been fabricated and characterized, they will be shown in the following sub-chapter.

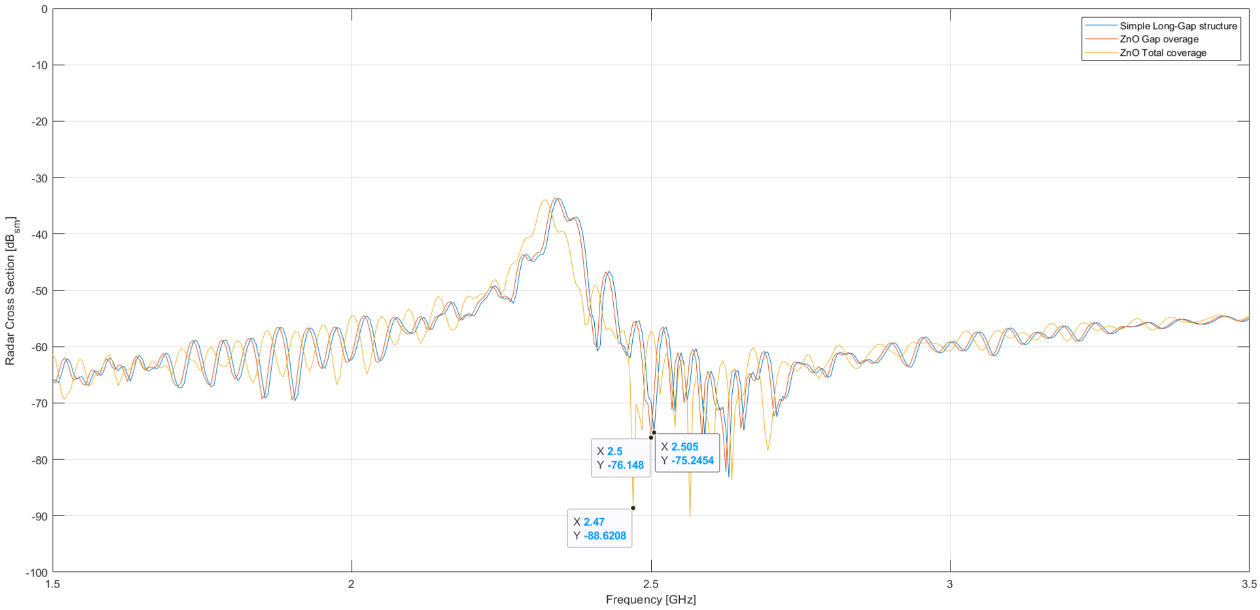

Figure 5.7: Resonance peaks of a "long-gap" single gold split ring resonator, with the a dielectric layer only in the gap and on the its overall surface.

5.2.3 Strain Detection

In Chapter 3.4, it has been shown the final structure design that have been taken in consideration for the strain sensing. The parameters of the chosen and subsequently simulated design are reported in Table 5.3, and shown also in Figure 5.8

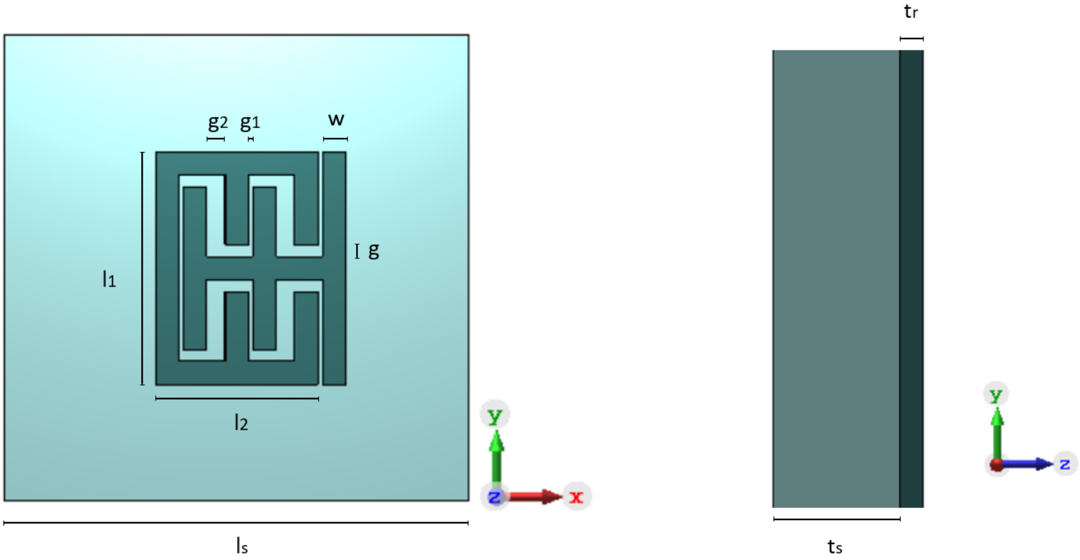

Figure 5.8: Chosen and simulated strain structure.

	l_s	l_1	l_2	w	g	g_1	g_2	t_s	t_r
Value	22	10	7	1	0.5	0.1	0.9	0.5	0.1

Table 5.3: Strain sensor dimensions, in *mm*.

To allow a correct study of the resonating frequency shift induced by the strain applied on the polymeric substrate, a COMSOL Multiphysics simulation have been performed. In the following, Figure 5.9 a), it is shown the final simulated device.

On the left of this structure a fixed constraint have been applied while on the right a sweeping force have been applied as boundary load acting along the positive x axis. The substrate material was meant to be POMAC, but since it is not pre-defined on COMSOL and since an hyperelastic module have been applied, it was harsh to gather its material and lamè parameters to perform the simulation. To have a qualitative results, PDMS, Polydimethylsiloxane, have been employed as substrate material and its lamè parameters were taken from [84]. In Figure 5.9 b) will be reported the image of the final device once the maximum simulated force will be applied.

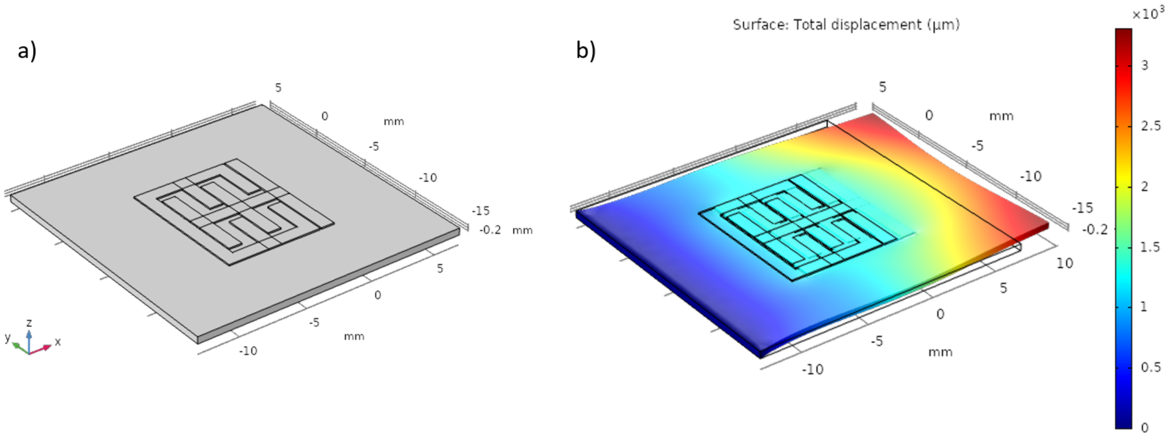

Figure 5.9: *a)* COMSOL Multiphysics simulated structure, *b)* Strain structure simulated after force is applied.

In Figure 5.10 there is reported the displacement to the applied force, and the two curves represents the displacement between the inner and outer structure of the strain sensing resonating device from their initial position. The difference between the two curves will give the total displacement that will be induced between the two structures. In the best case scenario, once a force of 25N gets applied, an overall displacement of around 90μm will be induced between the two structures.

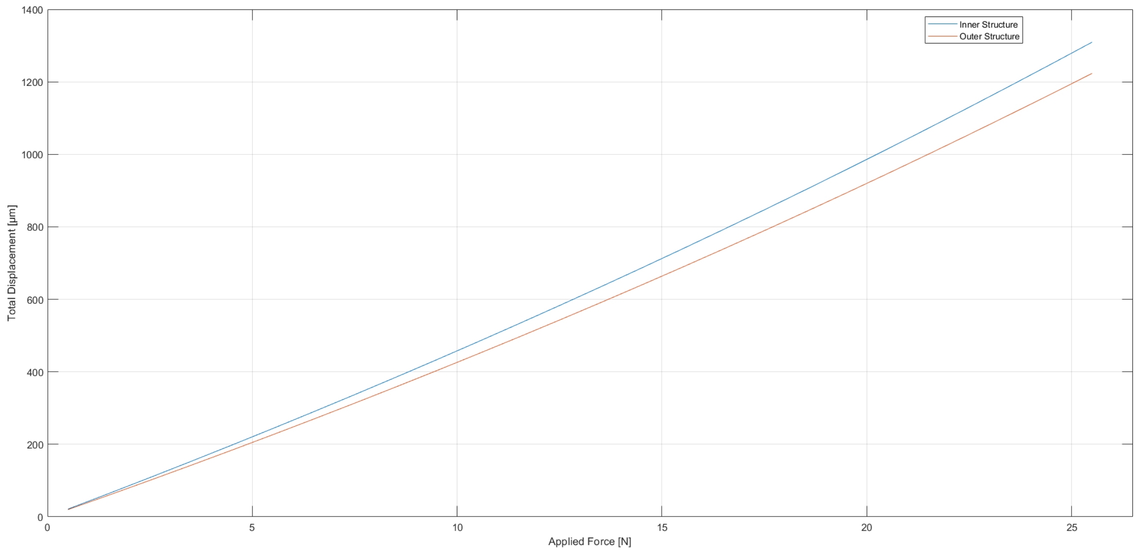

Figure 5.10: Force-Displacement relationship simulated through COMSOL Multiphysics.

Thanks to the above mentioned results it is possible to study the effect of the resonance frequency shift induced by the displacement of the two resonating structures. In the following a figure depicting the CST simulation of the strain sensing device will be reported for several applied displacements, or strains. Already a displacement of 50μm induces a shift of around 500 MHz, by considering the initial position, reported in Figure 5.8.

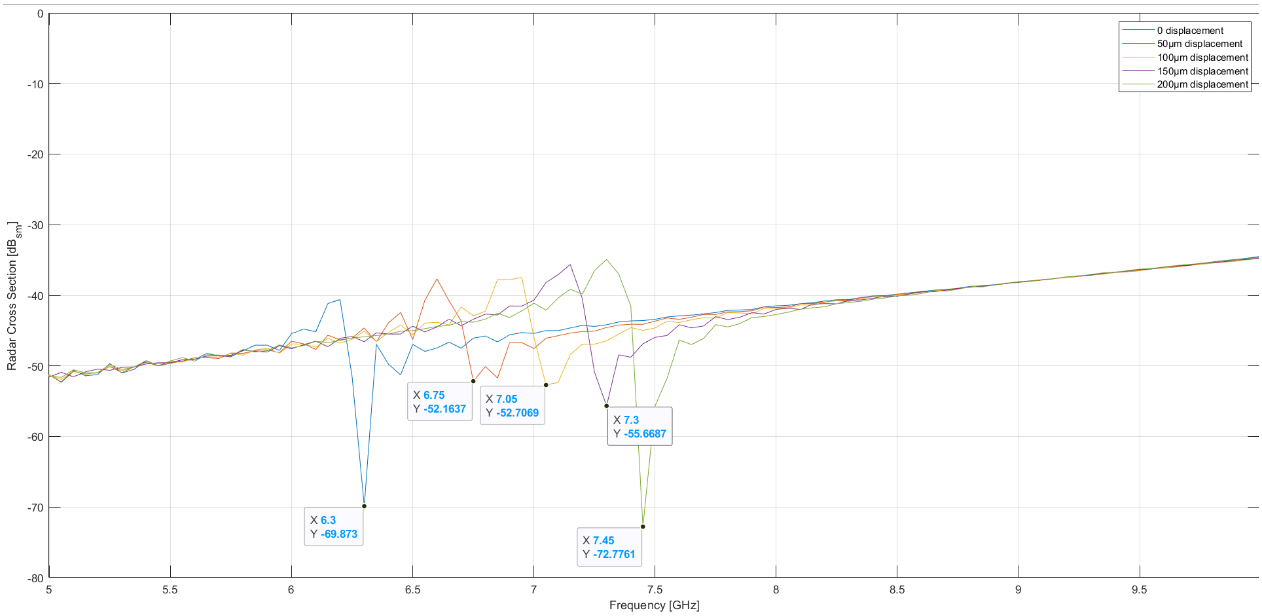

Figure 5.11: Sensor resonance peak shift induced by applied strain, considered as displacement.

5.2.4 In Human Detection

Here only a simulation consisting a double split ring resonator inserted into a layer of meat will be reported, allowing then a comparison with the results obtained in the following, and showing that ideally the resonator should be detectable once implanted.

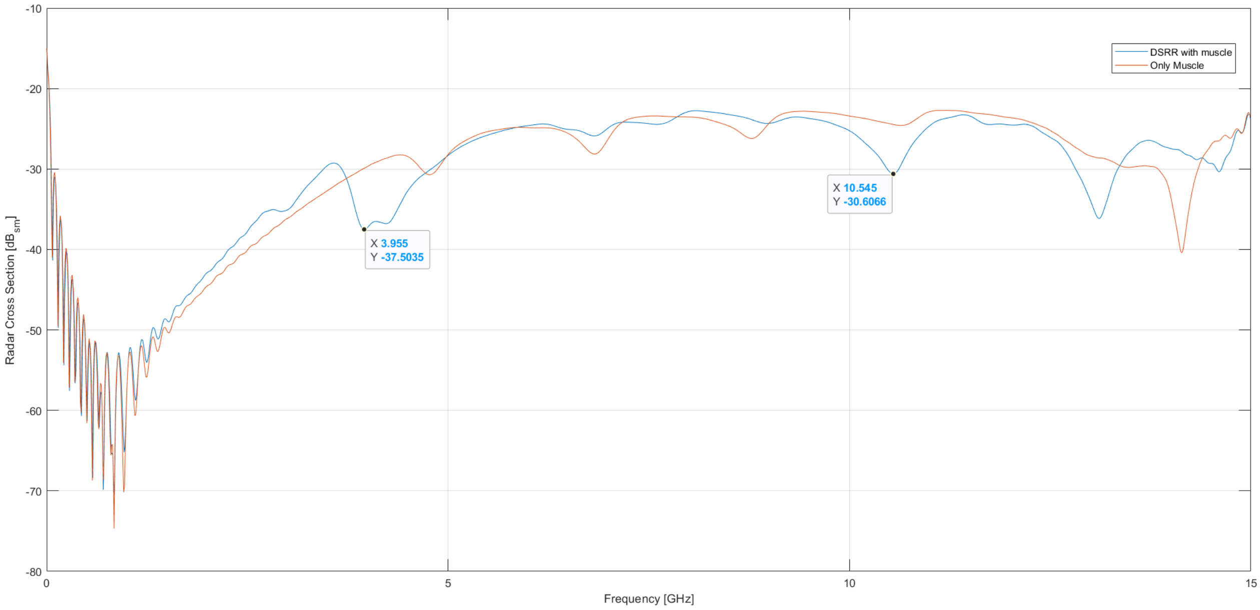

Figure 5.12: CST simulation of the double split ring resonator under a muscle layer of 3 mm in *a)*, and simulation of only the muscle to compare the EM results in *b)*.

5.3 Fabrication Results

Here will be shown the fabrication results of the final devices. Now a focus on the material and surface point of view for each one of the fabrication method will be described.

5.3.1 Blade Cutter

The blade cutter results will be shown in this sub section. In Figure 5.13 is shown the resonating device cut through the magnesium foils, for both the DSRR and the strain resonating device.

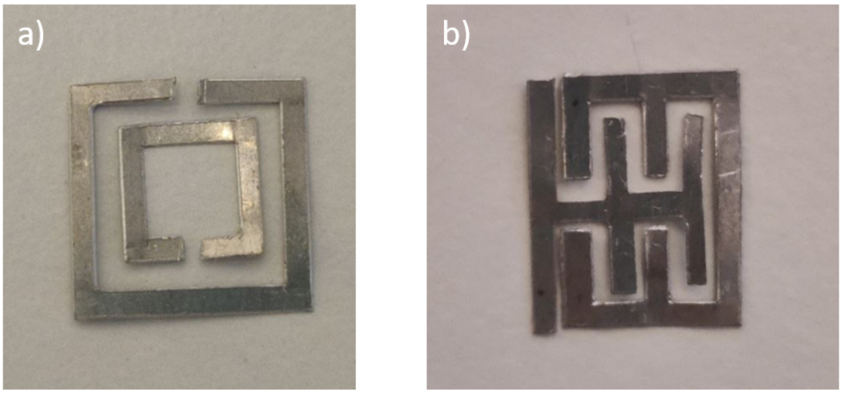

Figure 5.13: Blade Cut samples that have been employed as resonating devices.

During the cut from the magnesium foil the cut was not perfect, some scratches and some non perfect shape reproduction have occurred and are reported in Figure 5.14.

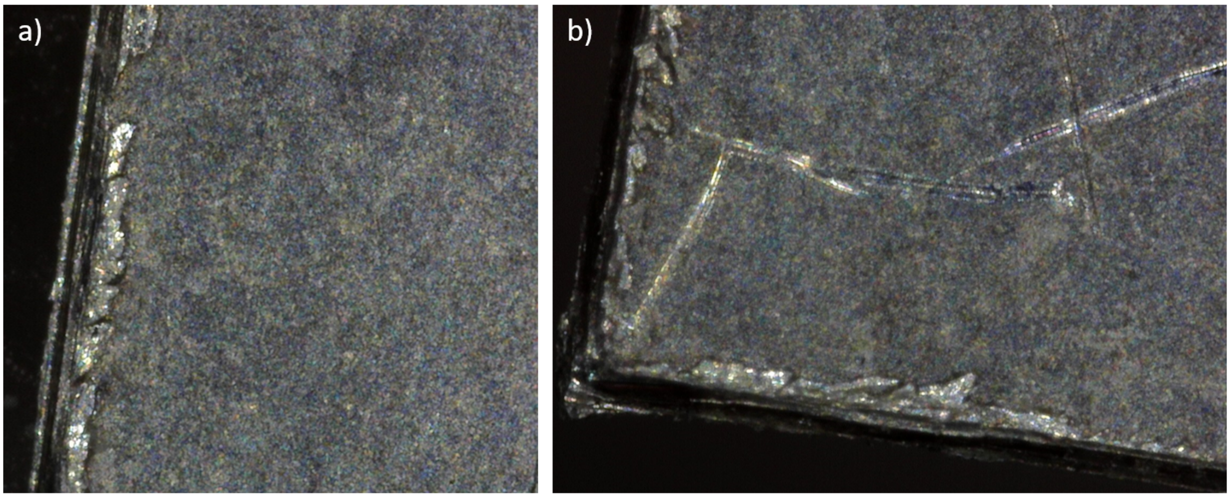

Figure 5.14: Blade Cut magnesium surface through Keyence SLM.

5.3.2 Evaporator

The fabricated Pt and Au split ring resonating devices are here reported, for the platinum, an image showing the devices still attached to the Si-wafer employed as holder, is shown. The main focus will be concerning the Au-based "Long-Gap" split ring resonator, that will be employed for the characterization of the ZnO NPs.

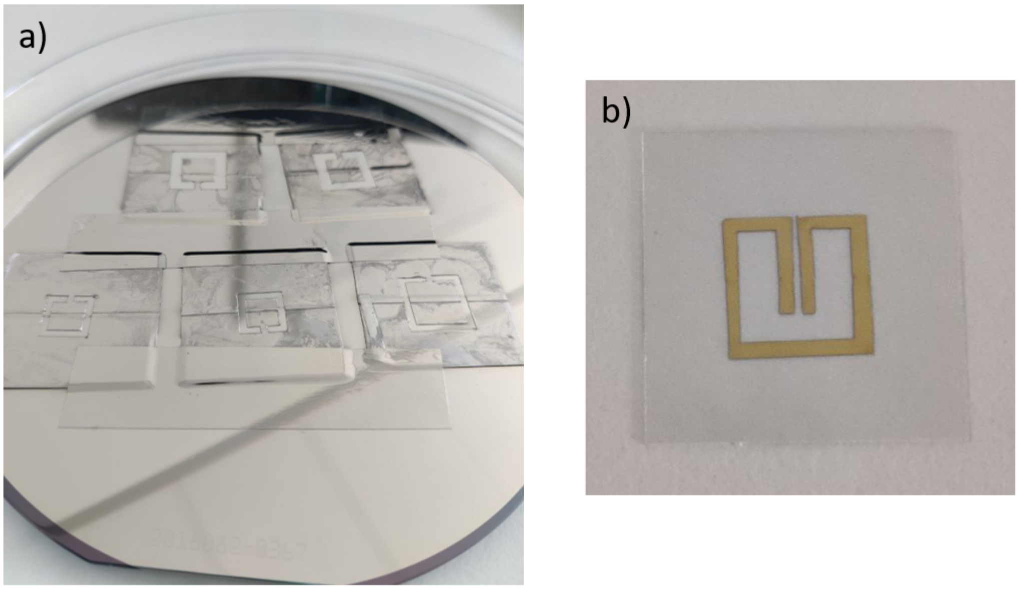

Figure 5.15: Manufactured Pt and Au split ring resonating devices.

To check the thickness of the gold layer and its width a Dektak stylus profilometer have been employed and the results are reported in Figure 5.16.

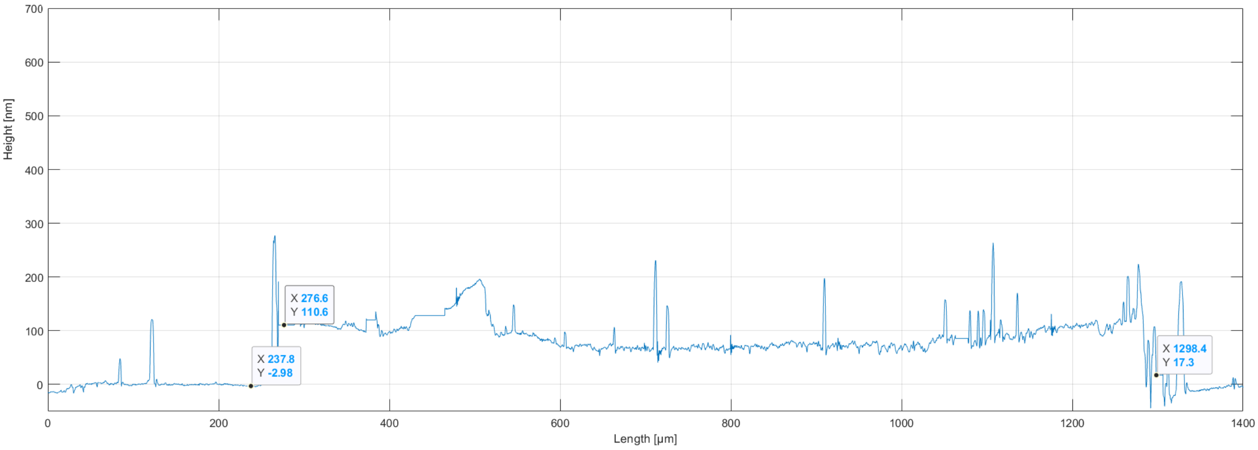

Figure 5.16: Dektak results of the gold SRR thickness and width.

5.3.3 MgZn Additive Manufacturing

First of all a study on the dimension of the magnesium-zinc powder particles have been performed and is reported in Figure 5.17. Some particles have been deposited on top of some carbon tape and inserted inside the JEOL SEM, the output image have been studied through ImageJ software to extrapolate their average diameter.

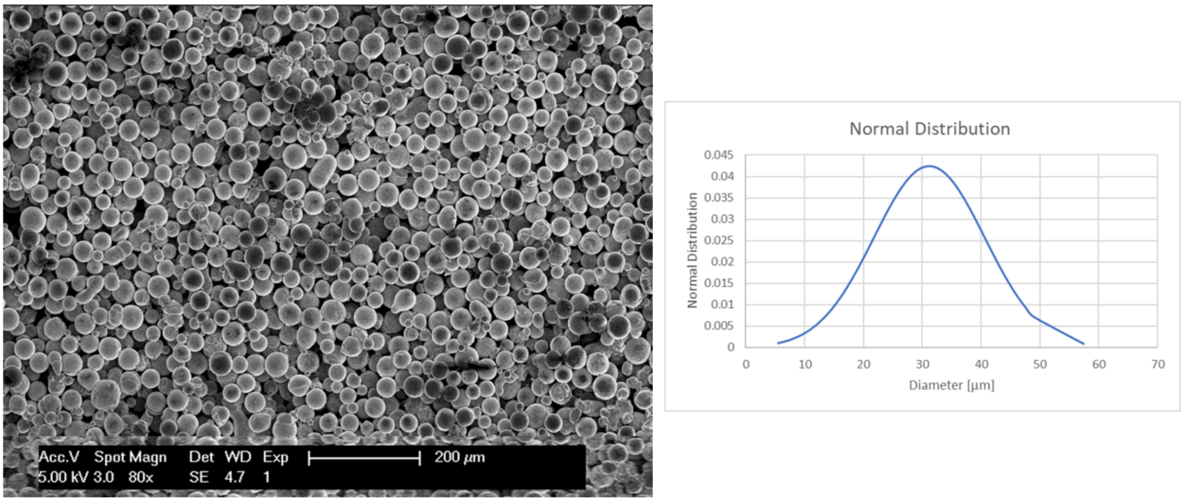

Figure 5.17: SEM Mg-Zn particle image and their diameter distribution.

For what concerns the Xerion furnace, an extremely brittle but holdable sample was manifactured. By testing its chemical composition through EDX an high carbon concentration have been found. Hence the only way to fabricate good samples was through the Carbolite Gero tube furnace. Here in the following are reported the device fabricated trough this machine, Figure 5.18. Then an EDX study have been performed before and after the sintering process to check the chemical composition variation of the resulting device.

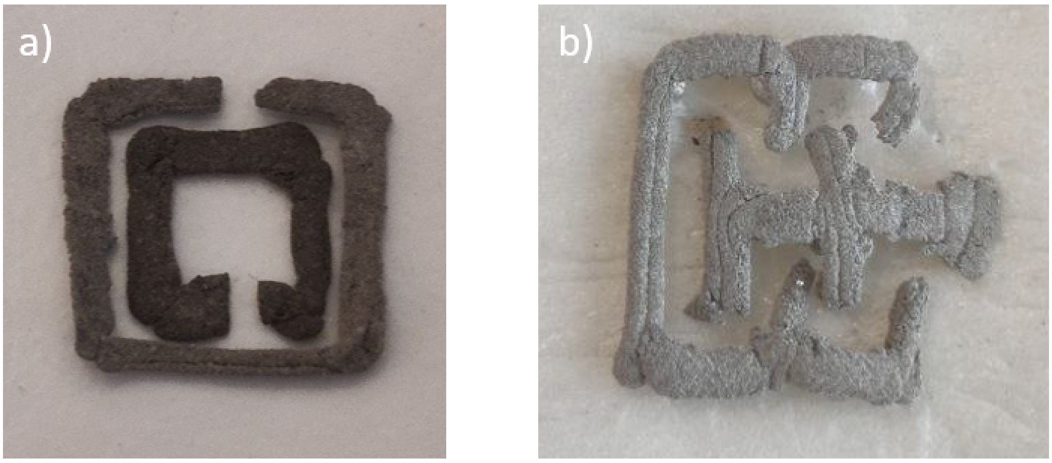

Figure 5.18: Additively Manufactured MgZn DSRR and strain resonating devices.

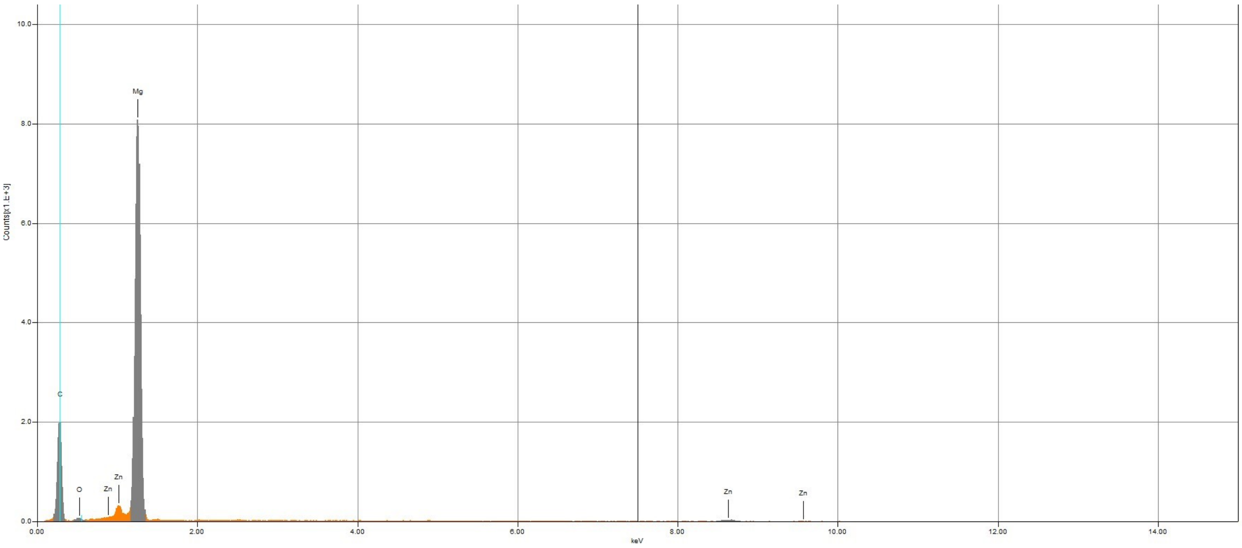

Figure 5.19: EDX results of an unsintered MgZn sample.

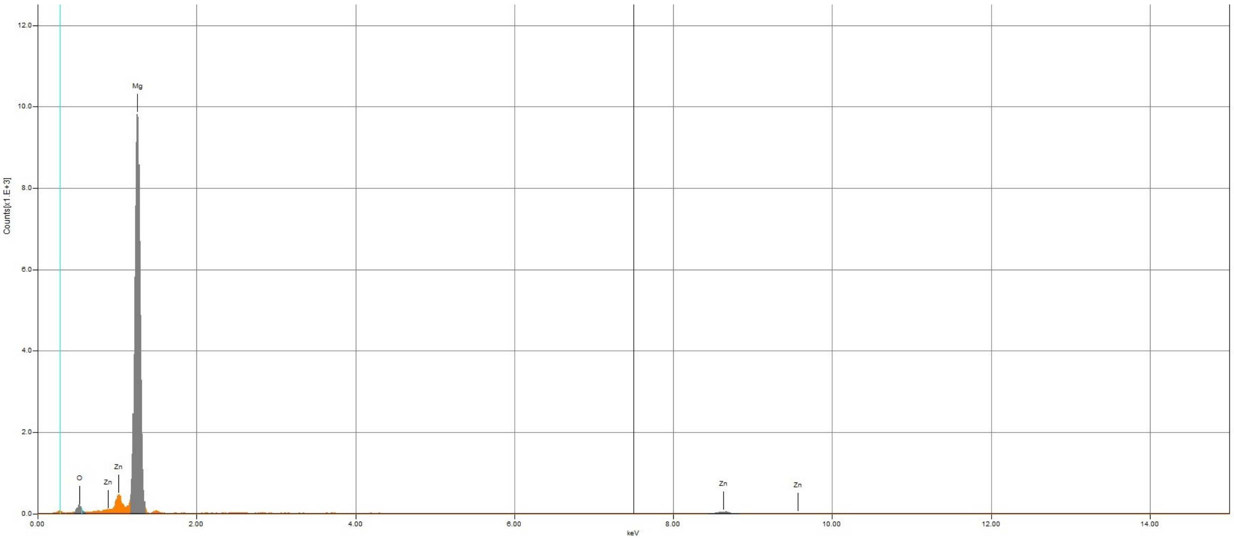

Figure 5.20: EDX results of a MgZn sample sintered through Gero machine.

SEM images will be reported to show the device structure. It is noticeable the difference between the sintered and unsintered structure that rely on the presence of some viscous material that covers the particles. Once sintering takes place only the metallic particles will remain and will bind one to another creating a conducting pathway between them.

SLM of the fabricated MgZn structure have been performed to show its 2D and 3D surface structure, which roughness will be reported in Table 5.6.

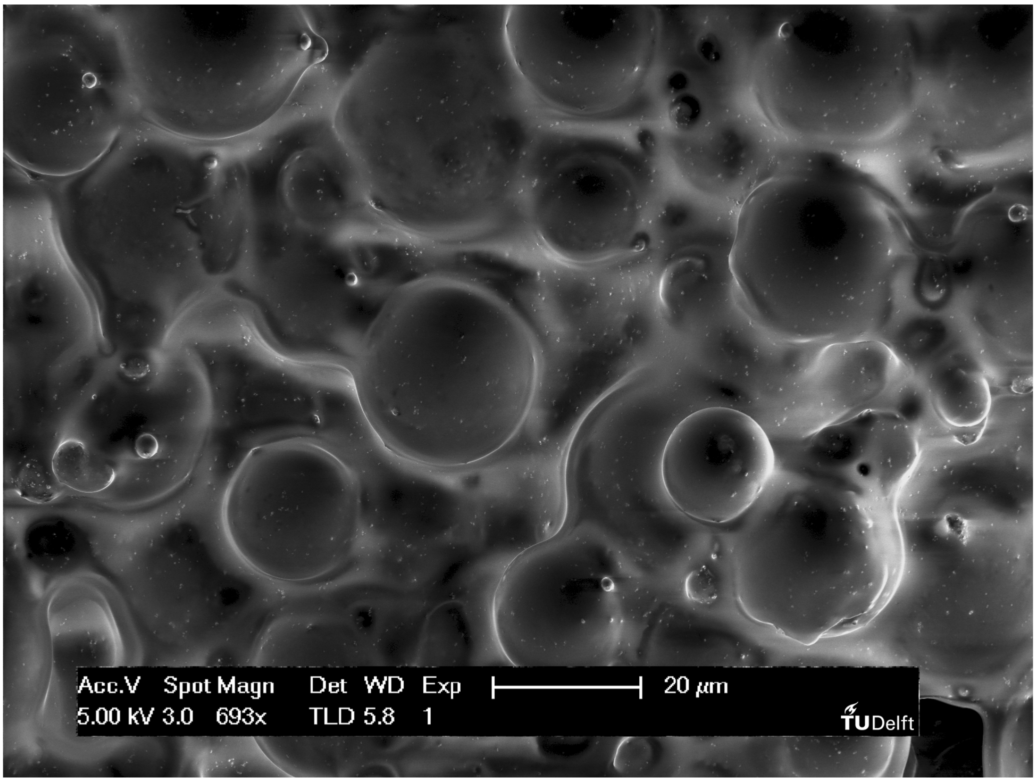

Figure 5.21: SEM image of an unsitered MgZn sample coated by HAp.

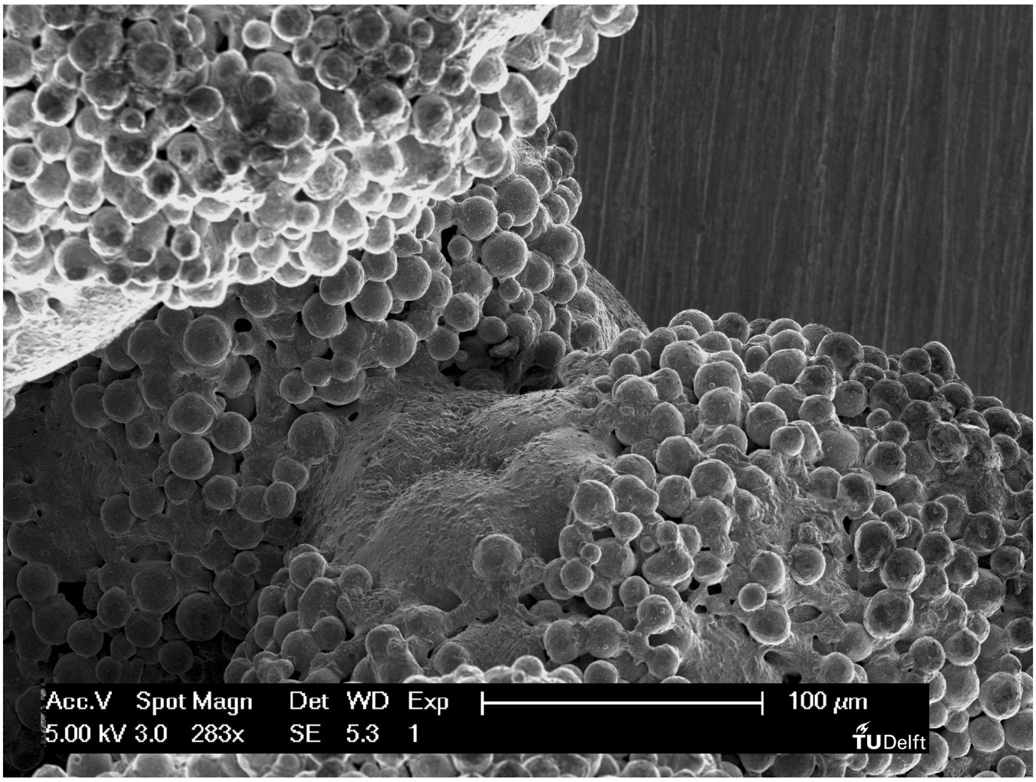

Figure 5.22: SEM image of an AM MgZn sample coated by HAp.

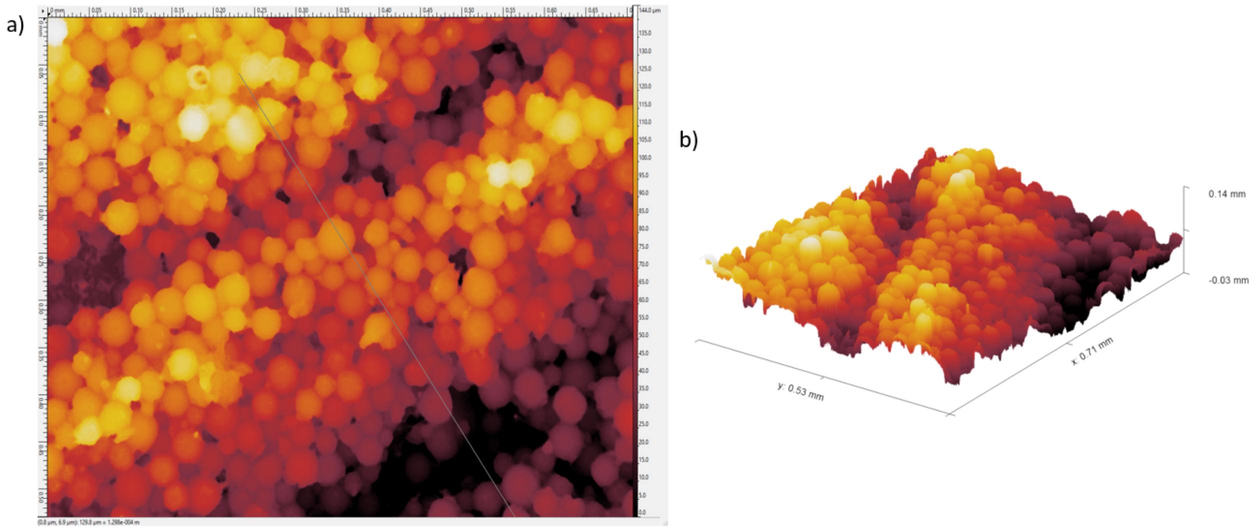

Figure 5.23: 2D *a)*, and 3D *b)* SLM analysis view of the AM Mg-Zn alloy.

A Van der Pauw clover-like structures were fabricated to perform 4-probe study to test the conductivity of the material, which resulted in a value of $\sigma = 1.23e^4 S/m$.

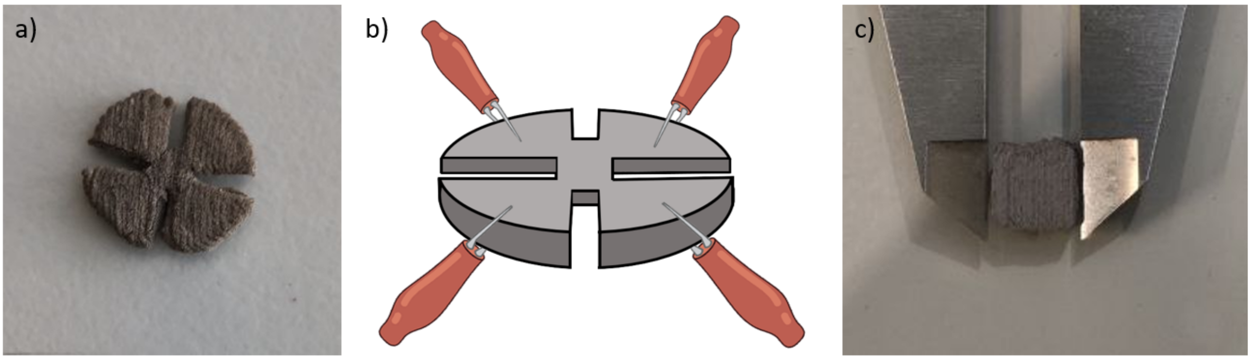

Figure 5.24: In *a)* the VdP clover shape, in *b)* sketch of the 4 probe measurement performed, in*c)* the cube structure for the density study.

Finally, a cube have been fabricated in order to show the density and dimension variation from the initial structure to the final sintered one, that will be reported in Table 5.4.

	$l(mm)$	$w(mm)$	$h(mm)$	$Wg(mg)$	$V(mm^3)$	$\rho(g/cm^3)$
MgZn designed	10	10	5	NA	500	1.7922
MgZn printed	8.95	9.25	5.2	370	430.495	**0.8595**
MgZn sintered	7.1	7.25	4.6	320	236.785	**1.35144**

Table 5.4: Dimensions of the designed cube, to the printed MgZn to the sintered structure.

5.3.4 HAp Coating

There is no huge visual variation between the uncoated to coated magnesium zinc samples, only a whiter surface would occur. Here is reported an image of the structure of the pure magnesium coated, to show its surface roughness and the effect of degradation related to the coating process.

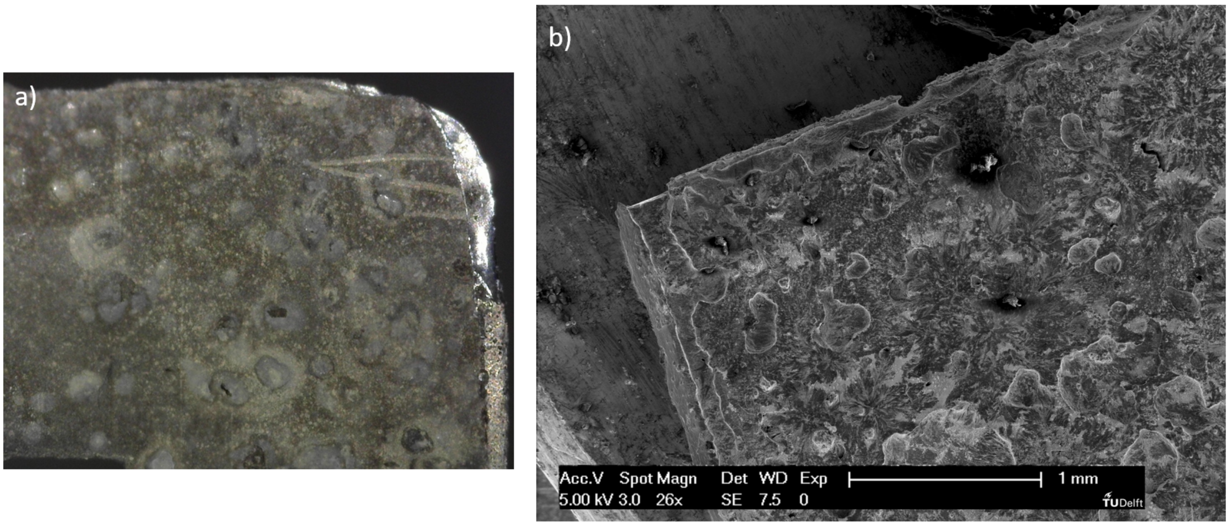

Figure 5.25: Results of HAp coating on pure magnesium sample.

Here are reported some SEM images of the HAp coating of magnesium-based samples.

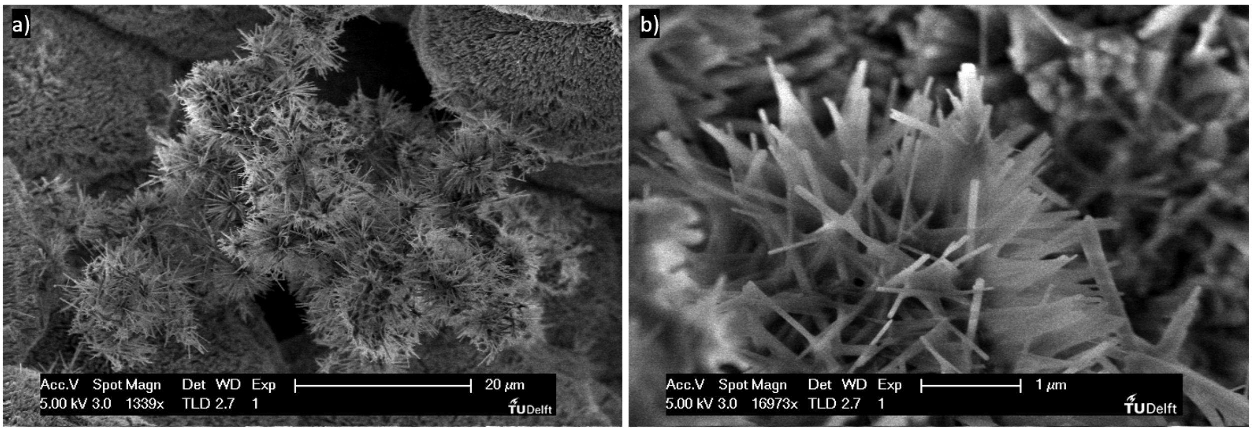

Figure 5.26: High magnification SEM images of HAp crystals.

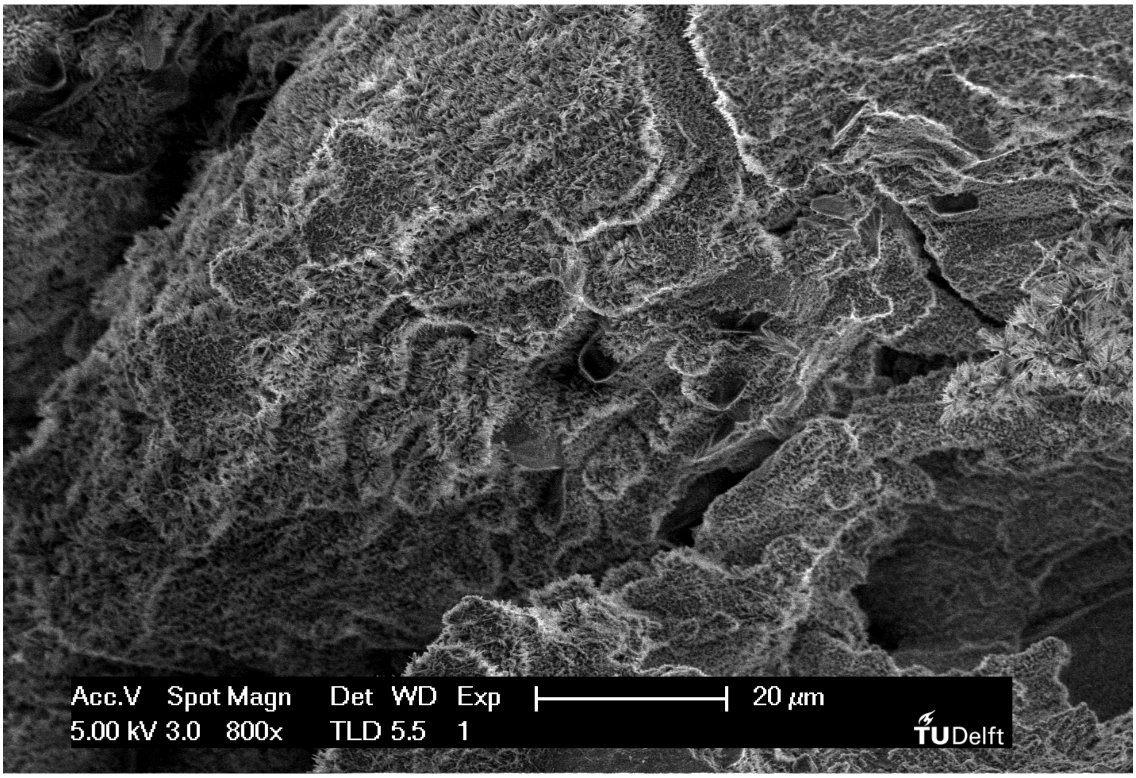

Figure 5.27: SEM image of a pure Mg sample coated by HAp.

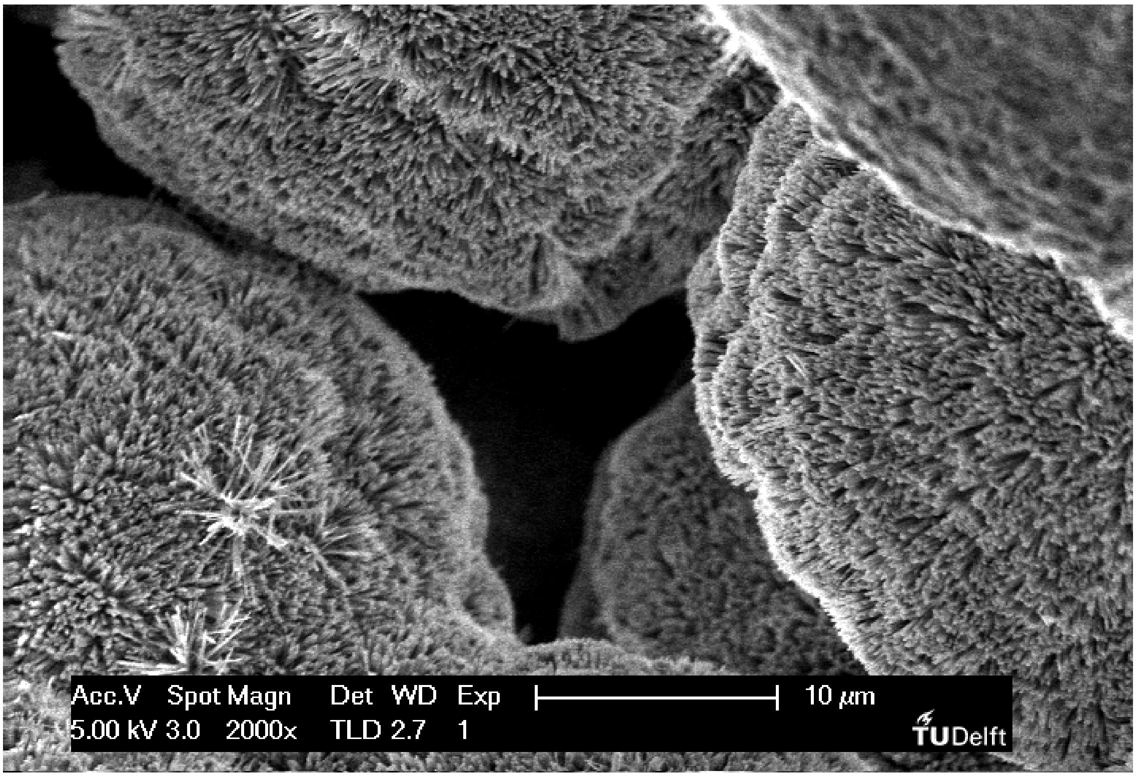

Figure 5.28: SEM image of an AM MgZn sample coated by HAp.

Now there will be shown the XRD and EDX analysis of the HAp coated samples, to demonstrate the chemical composition of the sampled materials.

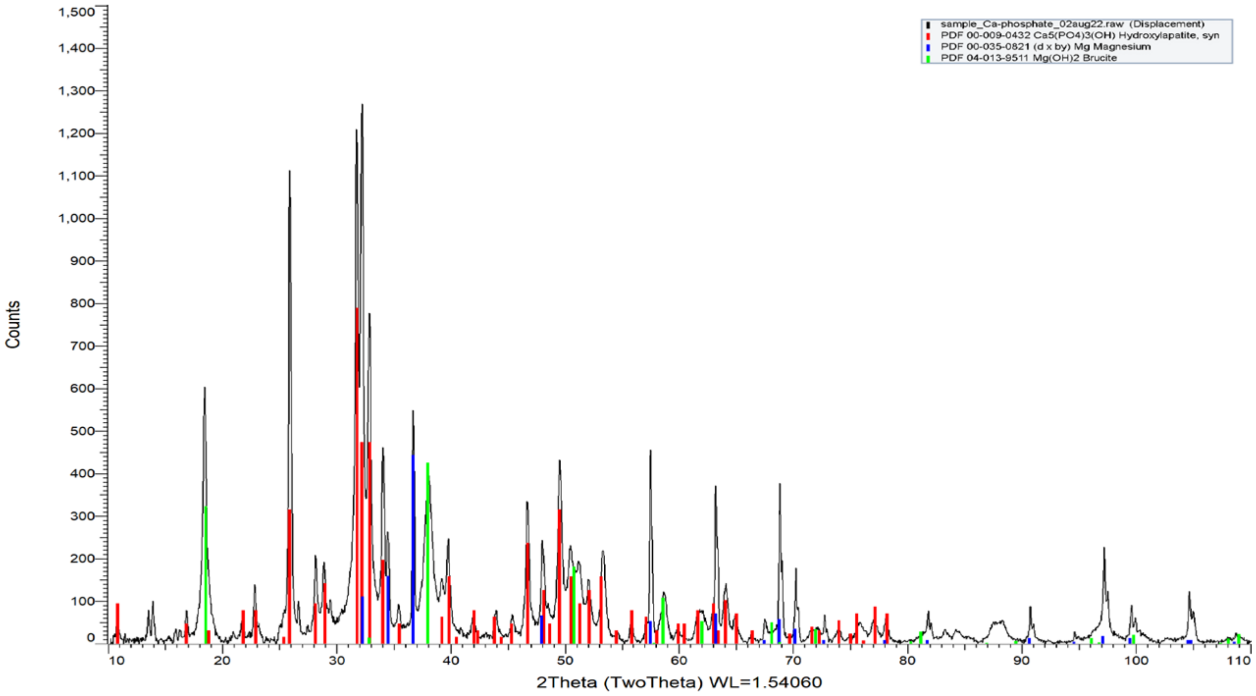

Figure 5.29: X-ray Diffraction Analysis of a MgZn sample coated by HAp.

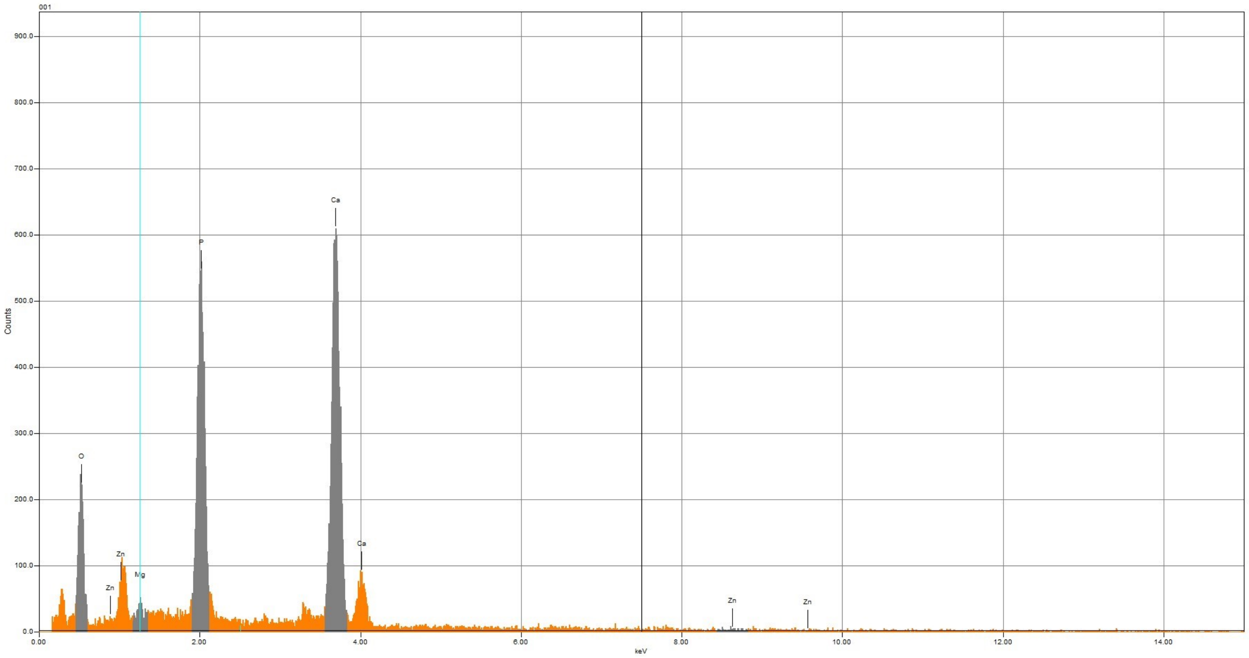

Figure 5.30: Qualitative view of the EDX analysis of an HAp coated MgZn sample.

	Mg	Zn	O	C	Ca	P
Unsint. MgZn 5.19	31.6-18.9	1.5-0.3	1.9-1.7	65.0-79.1	NA	NA
Sint. MgZn 5.20	86.7-87.8	7.0-2.6	6.3-9.6	NA	NA	NA
HAp 5.30	1.1-1.0	0.4-0.1	45.9-65.6	NA	33.2-19.0	19.4-14.3

Table 5.5: EDX qualitative analysis of the Mass% - Atom%, of Figures 5.19, 5.20, 5.30.

5.3.5 ZnO nanoparticles

Here is shown an SEM image of the ZnO nanoparticles deposited on the structures.

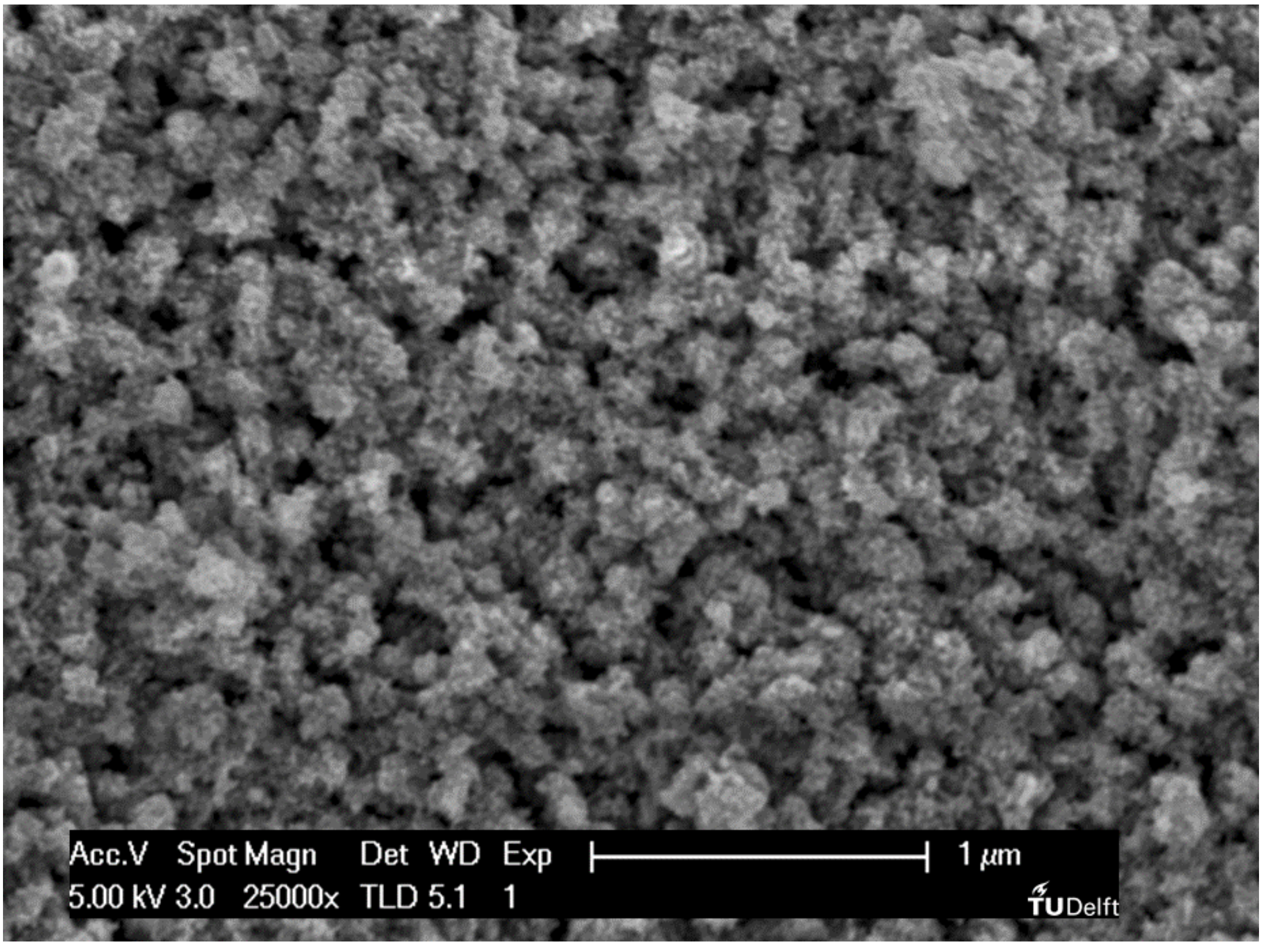

Figure 5.31: SEM image of the deposited ZnO nanoparticles on a sample.

Then the Zinc nanoparticles deposited on the gold "Long-gap" split ring resonator, only on the gap and on the overall structure in Figure 5.32 a and b, are shown. Then by annealing these particles will become transparent to visible light, as reported in Figure 5.32 c.

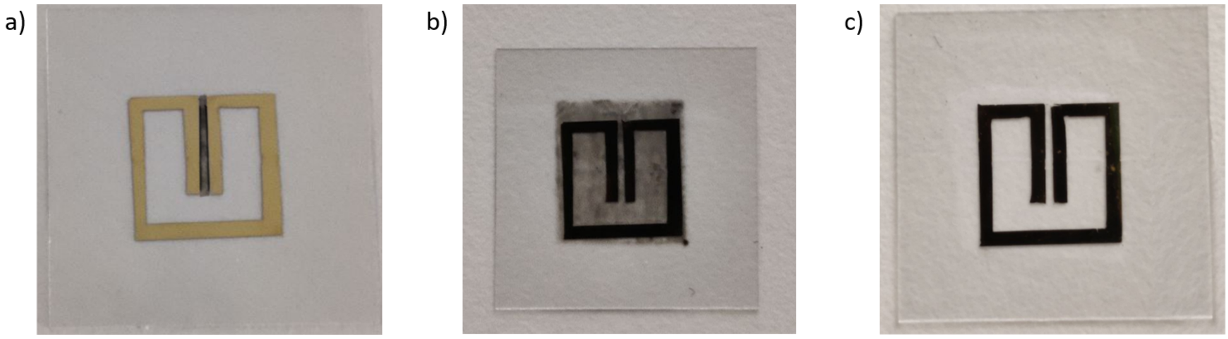

Figure 5.32: Ion sensitive pH senor device with zinc oxide deposited only on the gap, *a)*, and on the structure, *b)*. In *c)* is reported *b)* after annealing.

From the AFM measurements reported in the following figure, it was possible to extrapolate the surface roughness of this material reported in Table 5.6.

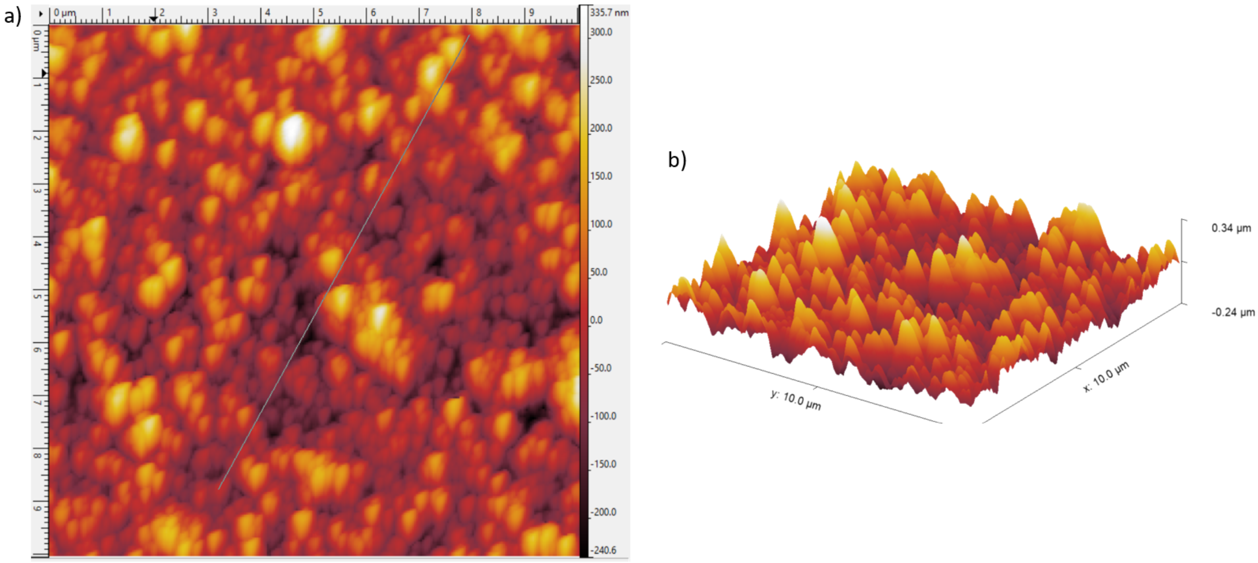

Figure 5.33: 2D *a)*, and 3D *b)* AFM analysis view of the Zinc Oxide deposited layer.

To check the average thickness of the deposited ZnO nanoparticles layer, the substrate have been tested under Dektak, and a results of 300 to 400 nanometers of overall thickness was possible to be measured.

	R_a (μm)	R_q (μm)	R_{sk}	R_{ku}	R_z (μm)	W_a (μm)	P_t (μm)
MgZn	1.085	1.637	0.08	12.9	15.74	18.62	149.6
MgZn HAp	1.489	1.865	0.087	3.022	10.73	18.62	94.52
ZnO NPs	0.011	0.015	-0.67	6.41	0.071	0.062	0.337

Table 5.6: Surface roughness of used materials through Gwyddeon of SLM and AFM data.

5.3.6 POMaC synthesis

For what concerns POMaC, it has been synthesized to be employed as lamination coating for the DSRR ion resistive pH sensor, and as substrate for the strain sensing device. In Figure 5.34 are reported the two devices in a perspective view.

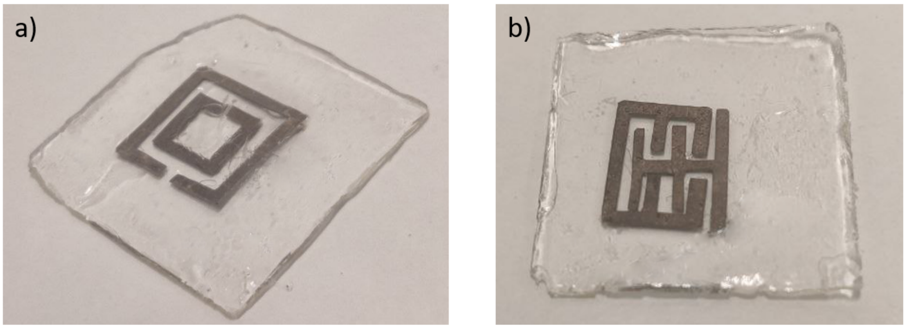

Figure 5.34: Double split ring resonator laminated into POMaC and strain resonating device onto a POMaC substrate.

5.4 Electromagnetic Results

Here will be described the electromagnetic results of the final devices described and modeled in the previous chapters. Three subsection will follow, for pH sensing device with the ion sensitive and ion resistive materials, and for the strain sensor. The distance between the antenna and the resonating device has been set to 10-15cm, making possible to consider the study in the near field region.

5.4.1 Ion Resistive pH Sensor:

As previously mentioned, the first method used to sense the pH variation relies on the double split ring resonator, one inside the other, coated by Hydroxyapatite, a pH resistive material, to allow a threshold sensing of the H^+ ions concentration.

In Figure 5.35, there is shown the pure magnesium blade cut and the AM magnesium zinc alloy double split ring resonator, respectively, fabricated and described in previous chapters.

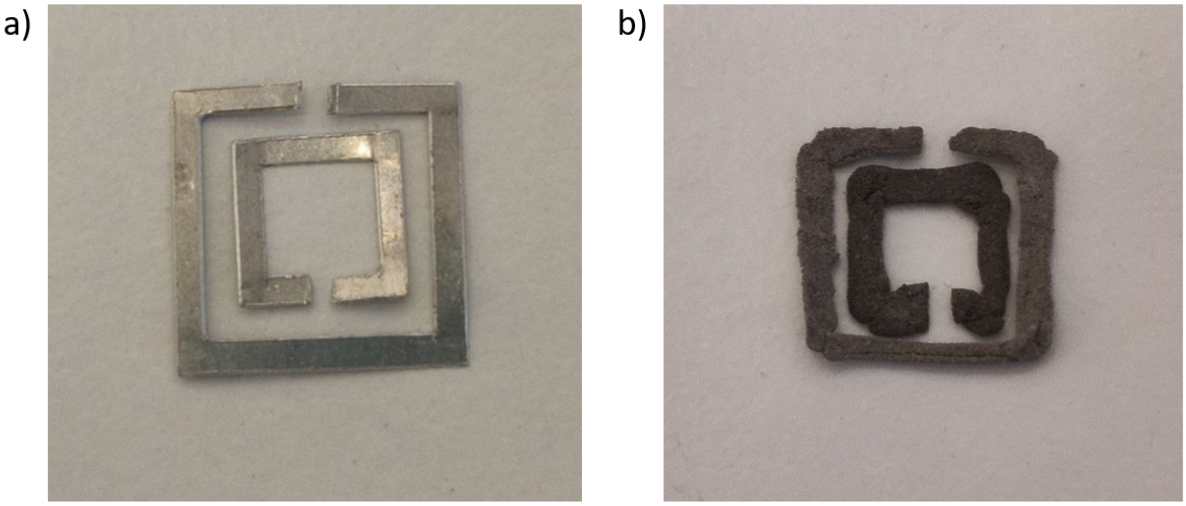

Figure 5.35: Blade Cut, BC, and Additively Manufactured, AM, double split ring resonating devices, DSRR.

Now there will be shown the resonance frequency of the two devices, starting from the blade cut sample. From the antenna setup shown in 5.1, the resonance frequency was possible to be extrapolated from the device. In Figure 5.36, it is shown the S_{11} parameter against the frequency of the pure magnesium DSRR, and its resonance frequency shift induced by the Hydroxyapatite coating. The distance chosen between the antenna and the resonating element was of around 15cm.

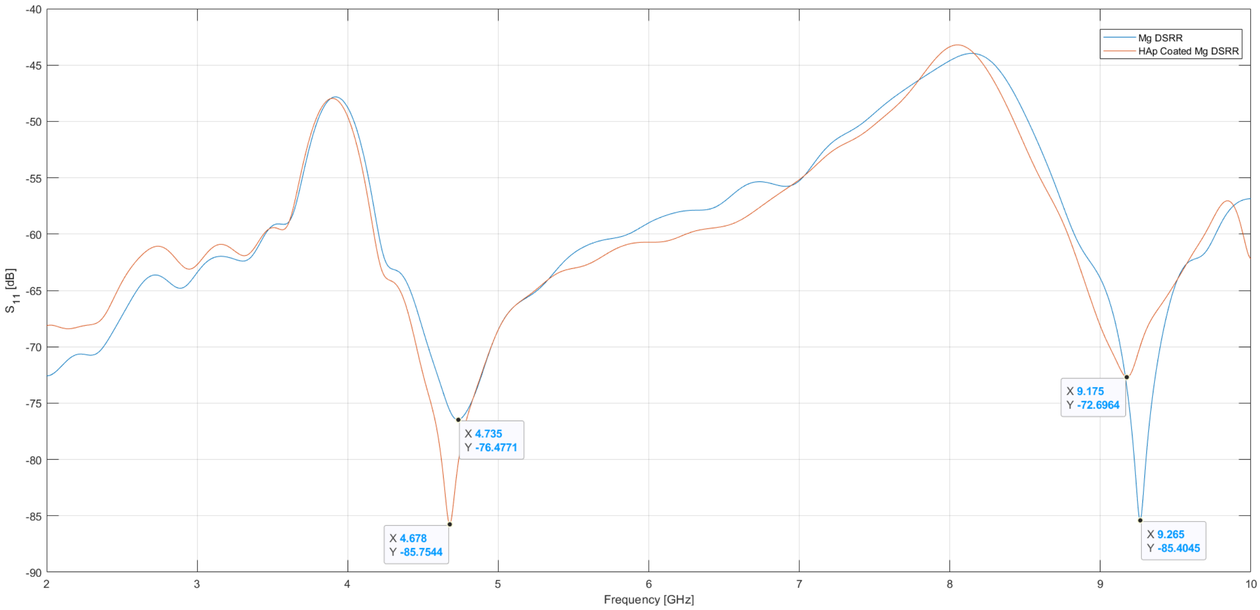

Figure 5.36: Resonance frequency of the pure magnesium double split ring resonator with and without Hydroxyapatite coating.

It has been studied also its behaviour once coated into a biodegradable substrate such as POMAC, as simulated in Chapter 5.2, and its resonance frequency variation from the only HAp coated sample will be here reported.

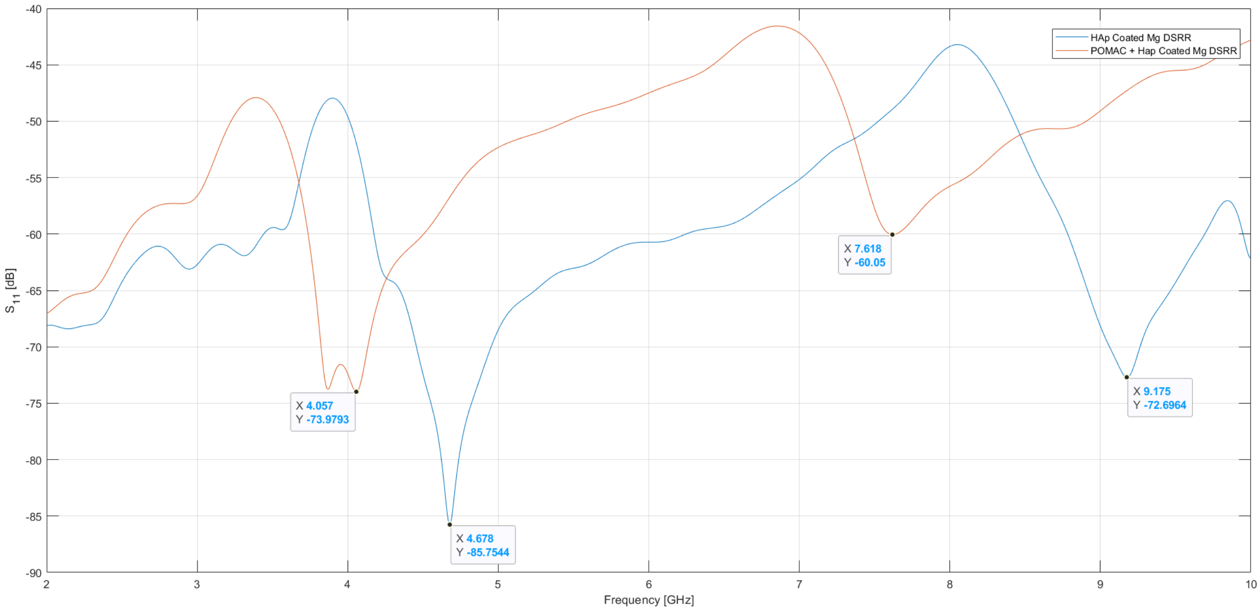

Figure 5.37: Resonance frequency of the HAp coated pure magnesium double split ring resonator with and without POMAC lamination.

Finally here will be reported the resonating behaviour of the additively manufactured magnesium-zinc alloy.

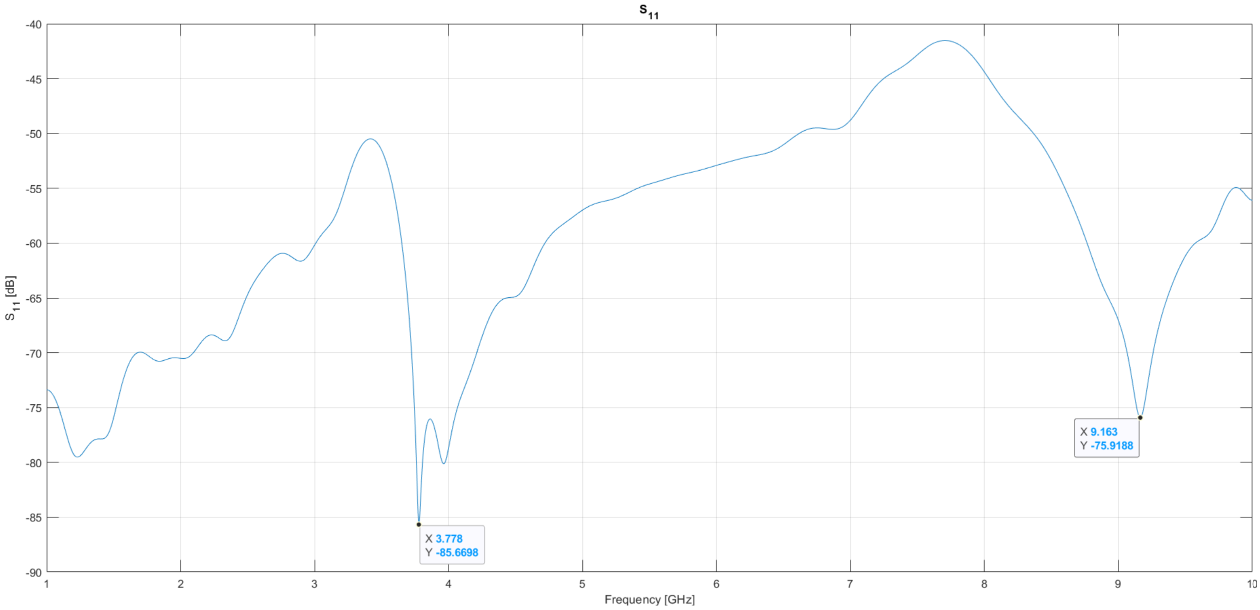

Figure 5.38: Resonance frequency of the additively manufactured double split ring resonator MgZn sample.

Then in Figure 5.39, is reported the resonance frequency of only the inner and outer rings of both the resonators shown in Figure 5.3, to allow then a comparison of its resonating frequency.

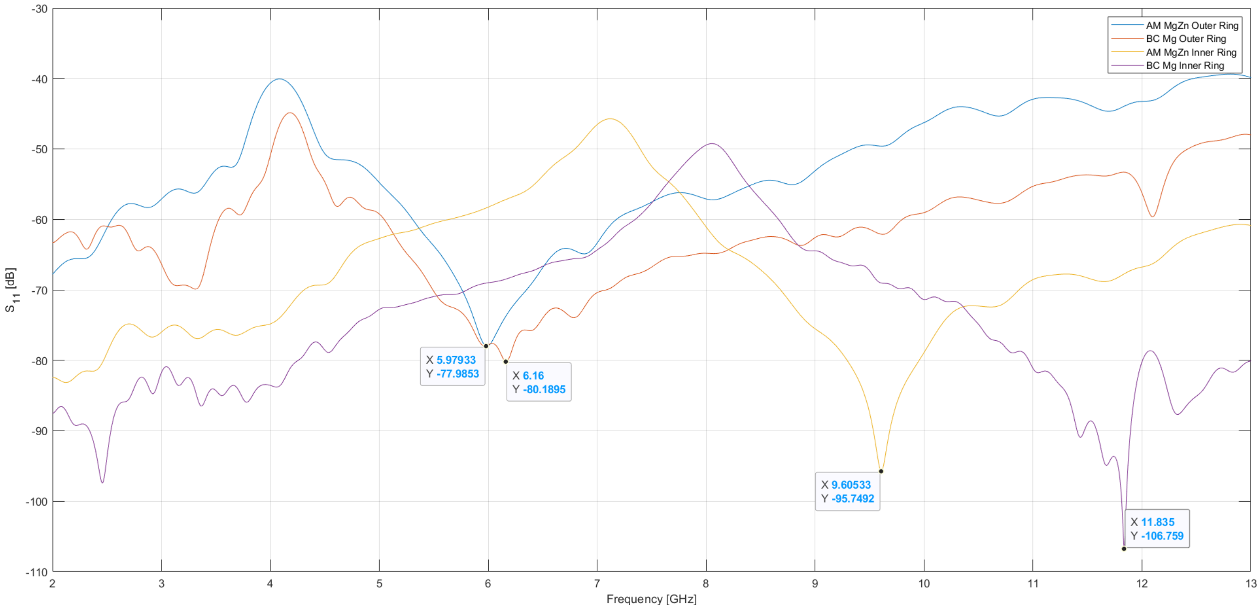

Figure 5.39: Resonance frequency of the inner and outer rings of both the AM and BC split ring resonators.

5.4.2 Ion Sensitive pH Sensor:

In this sub-chapter will be discussed the ion sensitive based pH detection method, which relies on the employment of a gold based split ring resonating devices. First the devices without the zinc oxide nanoparticles, reported in Figure , will be studied, and in Figure 5.40, will be reported their resonance frequency for both the "Short-gap" and the "Long-gap" golden split ring resonators. For the "Long-gap" case, two structures have been reported which will be needed to further describe the variation of resonance frequency induced by the deposition of ZnO NPs, described in the following

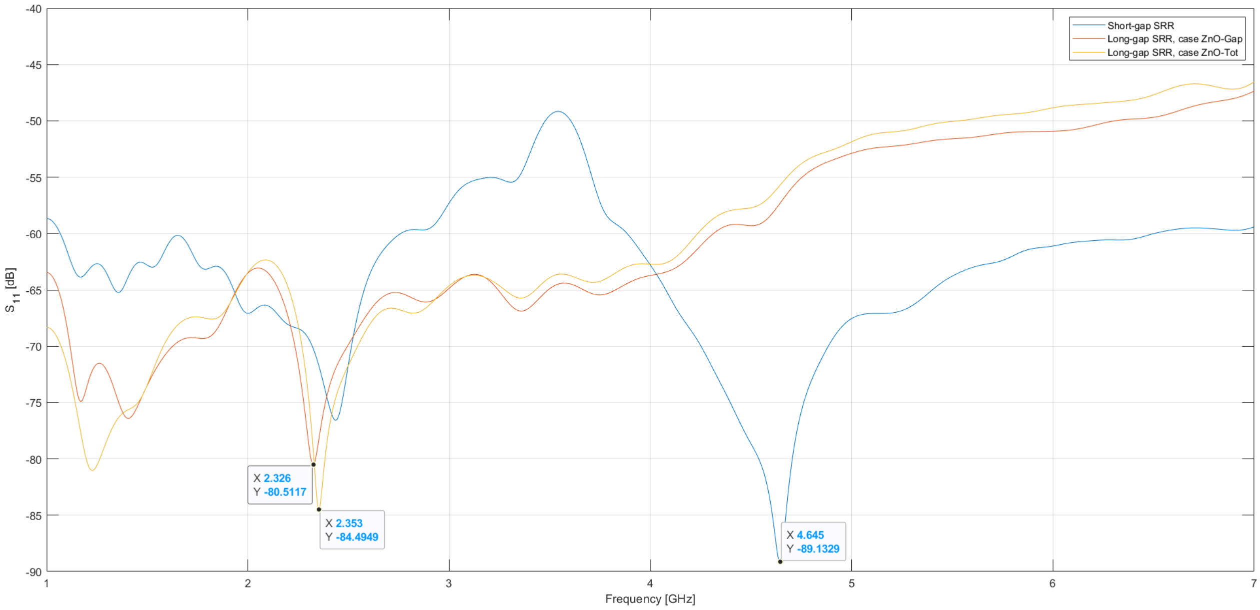

Figure 5.40: Resonance frequency of the gold based SRR with "Long" and "Short" gap.

Then the coating with Zn NPs have been performed, and the two studied structures are reported in the following, Figure 5.32, before annealing, otherwise transparent. The two structures shown, depicts the two different approaches studied for the pH detection with the deposition along only the gap of the structure or the whole resonator. For simplicity the two structures will be now defined as follows: $ZnO - Gap$ and $ZnO - Tot$, respectively.

As follows the analysis of the devices before and after the immersion into a pH 1.2 and pH 4.4 will be reported. To perform the pH study, the different pH solution, prior mixed, have been casted on top of the ZnO NPs, then after some time they would get pipetted out, and left drying in the environment. This whole process would take place below the antenna to reduce the signal variation induced by the position shift of the resonating device.

After two days the resonance frequency returned similar to the initial value of the device, only then the second pH study was performed. In Figure 5.41, it is shown the resonance frequency variation induced by the $ZnO - Gap$ device before the solution casting and after its evaporation.

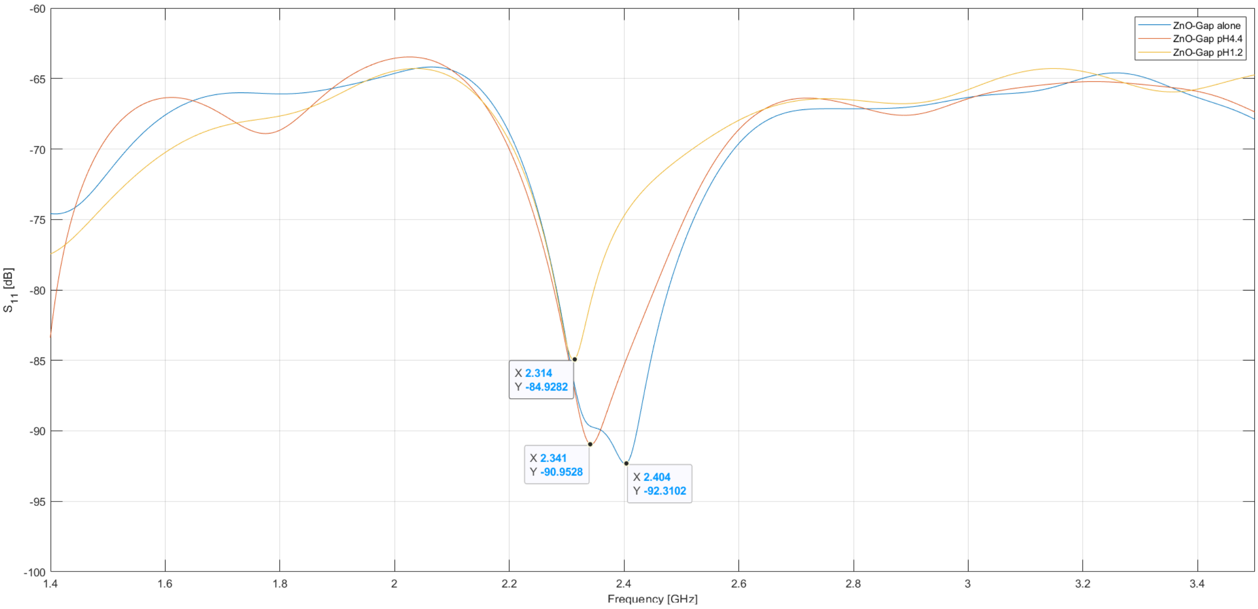

Figure 5.41: Resonance frequency of the gold SRR with ZnO NPs deposition on the gap, before and after contacting different pH solutions.

In Figure 5.42, it is shown the resonance frequency variation induced by the $ZnO - Tot$ device before the solution casting and after its evaporation.

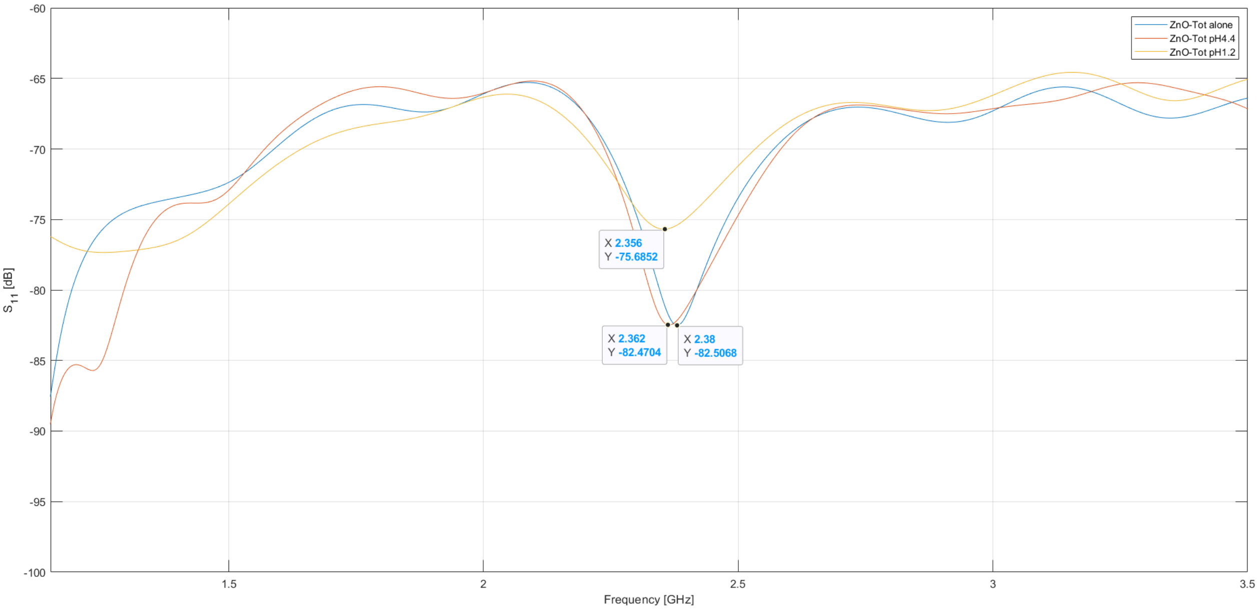

Figure 5.42: Resonance frequency of the gold SRR with ZnO NPs deposition on the whole structure, before and after contacting different pH solutions.

5.4.3 Strain Sensor:

For what concerns the strain sensing, the blade cut results are shown in the following pictures, with the gap distance similar to what shown in Figure 3.9.

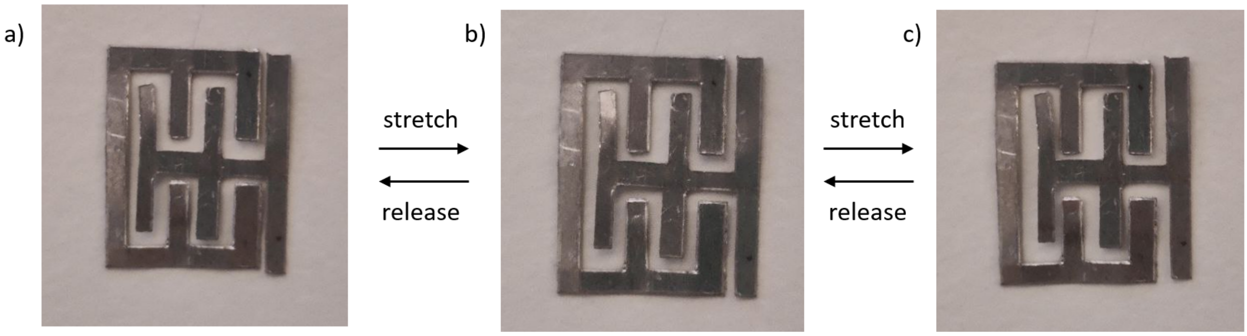

Figure 5.43: Blade cut structure of the strain sensor, a variation of resonance peak will take place due to the displacement induced by the stress.

Here the resonance frequency variation will be shown in Figure 5.44. A huge displacement have been considered since it had to be manually displaced and a small variation was mostly impossible.

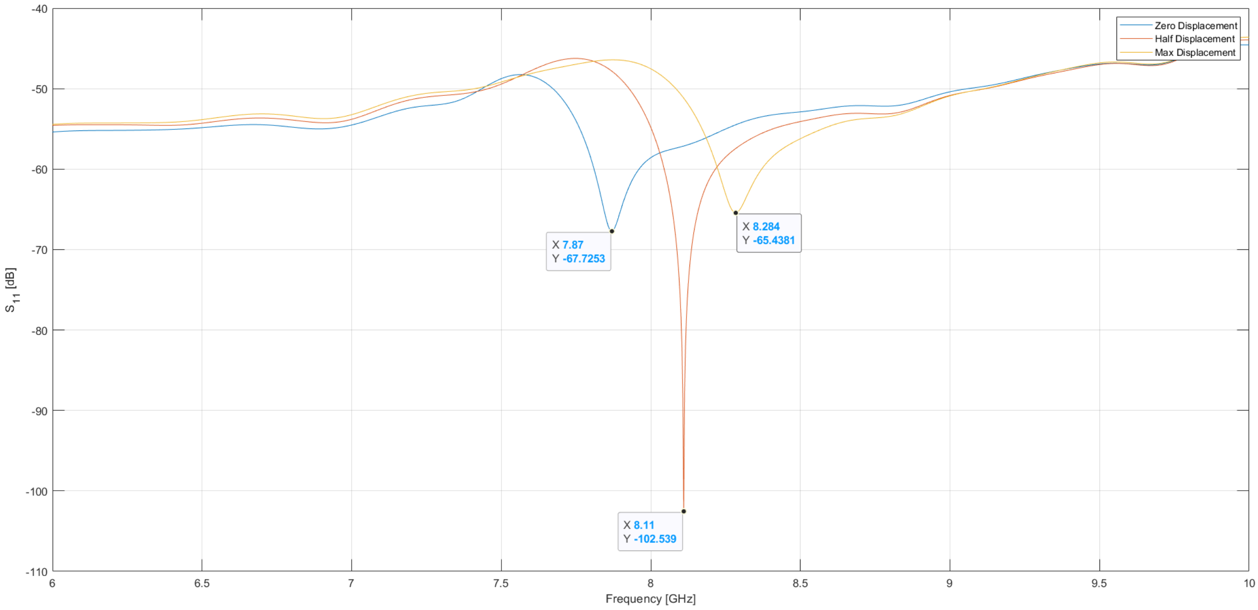

Figure 5.44: Resonance frequency of the BC strain sensor with no displacement, half total displacement and max displacement induced.

For what concerns the AM structure, during the transportation both "arms" of the inner structure were broken, its final design is reported in the following, Figure 5.45.

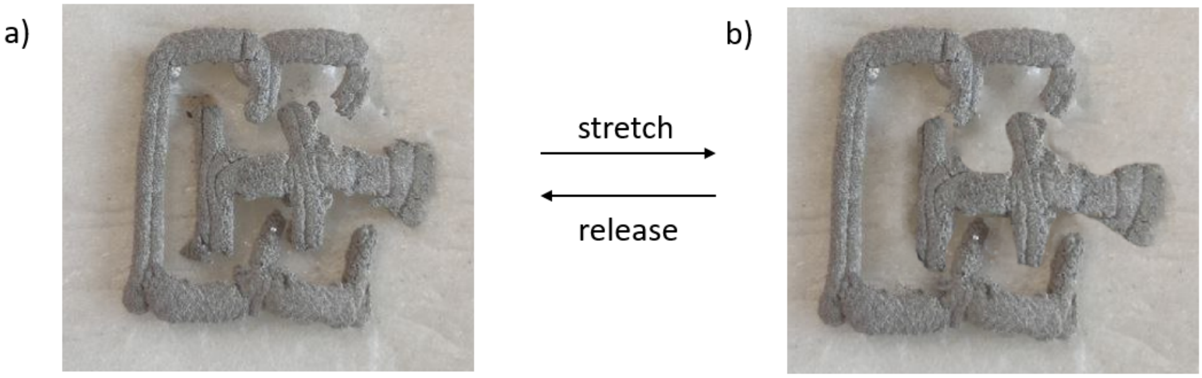

Figure 5.45: AM strain sensor, before and after the strain gets applied.

A small resonance peak shift is expected to happen due to the absence of the device structure, indeed as reported in Figure 5.46, a shift of only 500MHz occurs once the maximum displacement takes place.

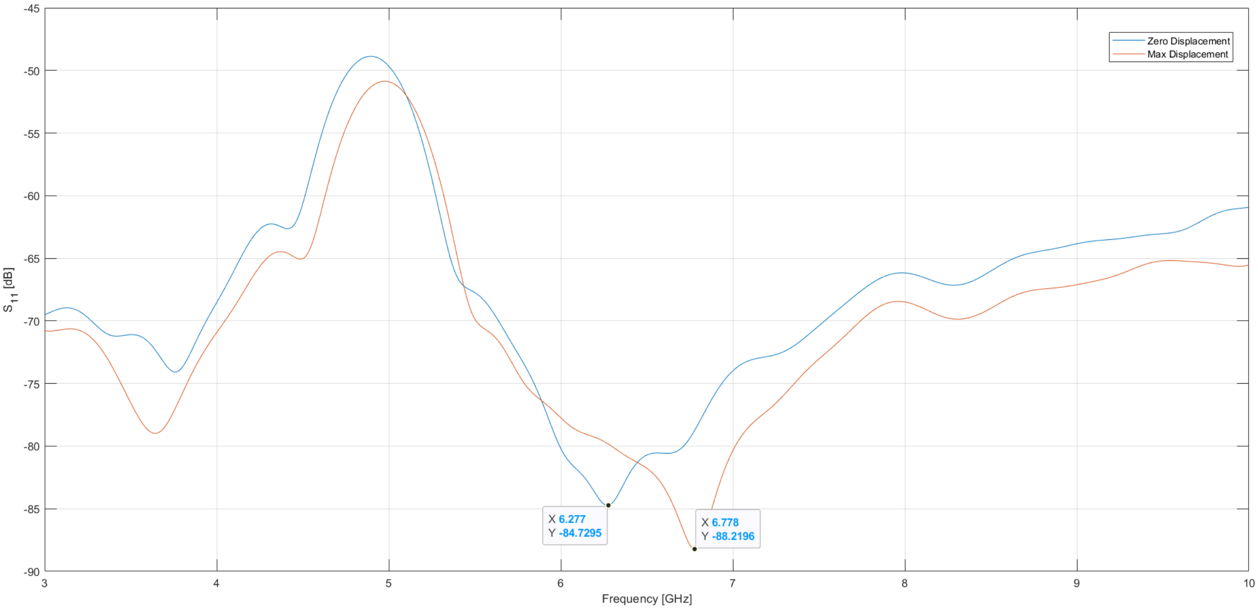

Figure 5.46: Resonance frequency of the AM strain sensor with no displacement and max displacement induced.

5.4.4 In Human Study:

To perform this study some beef meat have been employed with the dimensions of $2.5x2.5x1$ mm. An HAp coated BC DSRR have been employed for the study. The resonating structure has been placed in a plastic holder, and on top of it the meat layer have been carefully deposited to not displace the device. In Figure 5.48, is reported the resonance frequency of the DSRR before and after the positioning of the meat on top of it.

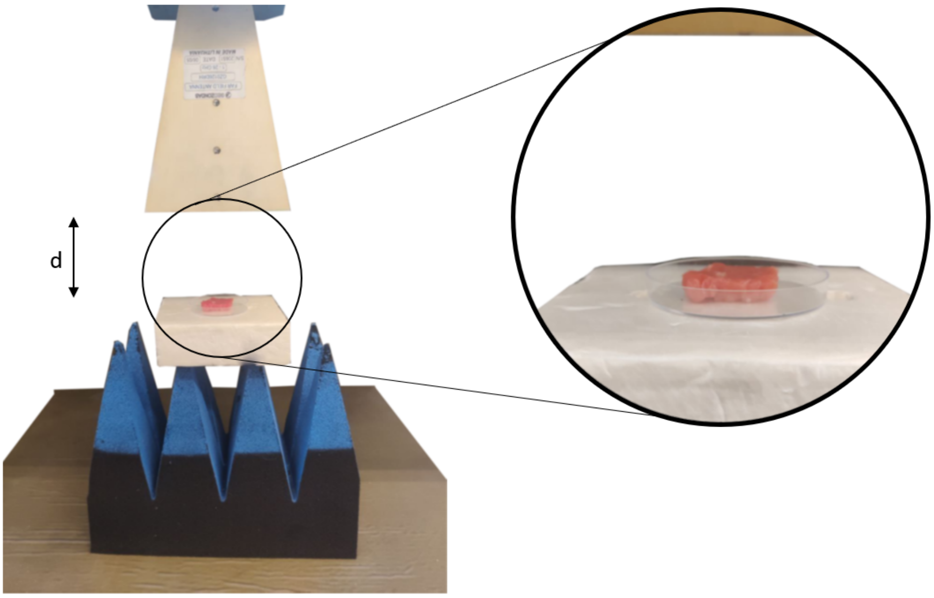

Figure 5.47: An holder containing a BC HAp coated DSRR resonator covered by a meat layer, under the antenna-setup, at a distance on the order of 15cm.

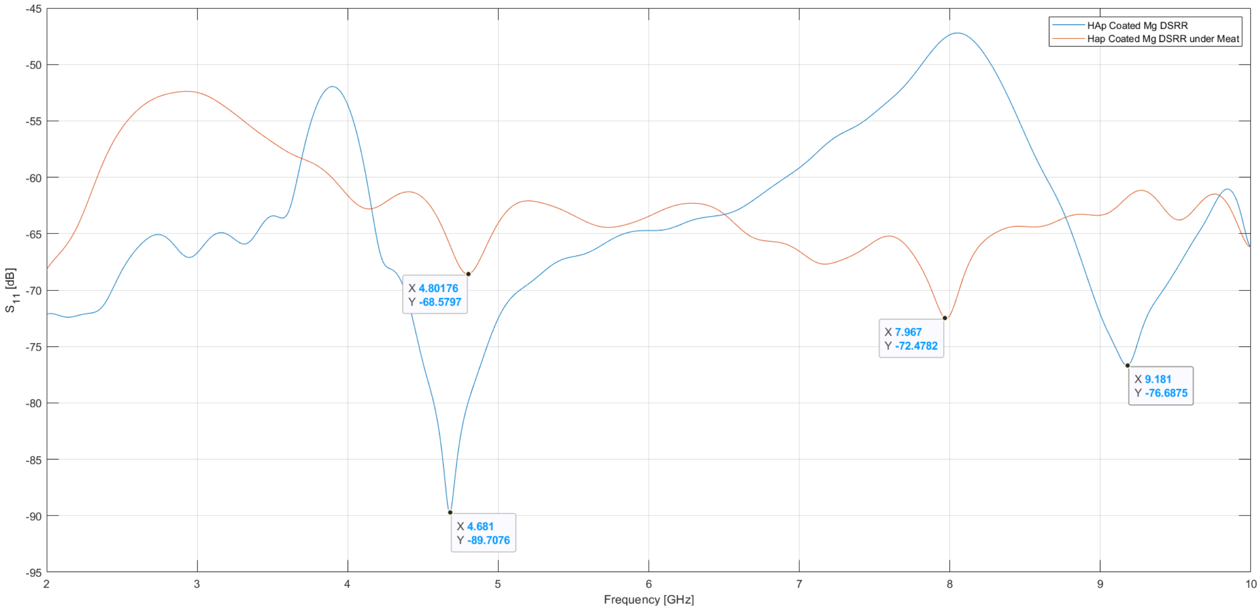

Figure 5.48: Resonance frequency of the Hap coated pure magnesium DSRR with and without meat on top of it.

5.5 Biodegradability

To perform the biodegradability test, a Phosphate-Buffered Saline solution have been fabricated. Into this solution the samples have been casted, and their weight have been measured week by week, to evaluate the degradation rate. The PBS solution is usually employed for this kind of test, since it tends to mimic the human body fluids pH, ion concentration and osmolarity. It is usually employed as a buffer solution for cell cultures.

After the PBS pallets are casted into water and fully mixed the solution gets divided into several small container. The containers, into which a different sample will be dropped, will be then placed inside an incubating machine, that will maintain the temperature constant to 37.4°C, to mimic the human body.

Every week, a sample would have been taken out of the incubating machine, and its weight would be measured, recorder and normalized over their own initial weight. In Figure 5.49 is reported a column chart containing all the different normalized weight per week.

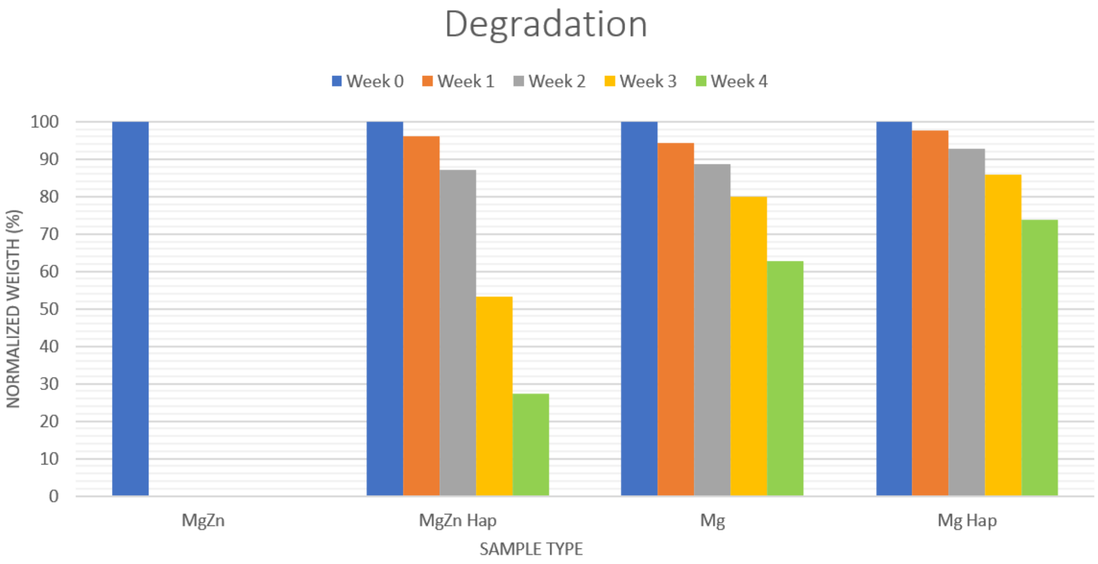

Figure 5.49: Biodegradability test effectuated on the Hydroxyapatite coated and uncoated AM MgZn and BC Mg samples.

For what concerns the bare AM Mg-Zn samples, in the first two days it's weight were increasing due to the bio-product released by its degradation, and already after four days it was fully degraded, hence its column stopped at week0.

Chapter 6

Discussion

In Chapter 5 the results obtained have been reported and will be discussed in this chapter. Here first the fabrication results will be taken into account to further discuss the electromagnetic ones comparing them to the simulations performed.

Blade cut samples have been shown in Figure 5.13, and it was possible to see how the non perfect cut would generate either some scratches on the surface or some difference in shape reproduction, reported in Figure 5.14.

Evaporated samples are reported in Figure 5.15, for both Platinum based and Gold based split ring resonators. On 5.15 a, it is shown the Pt based SRR still taped on top of a Silicon wafer, and still coated by the polyimide layer, while on b it is shown the final "Long-gap" SRR. Then in Figure 5.16, is shown the profilometer study performed on the short gap Au SRR that had an overall thickness of 115 nm and width of 1.05 mm, while 110nm and 1 mm were expected.

For AM samples a first study on the particles dimensions have been performed, reported in Figure 5.18. Starting from an SEM image it was possible to extract the normal distribution of the particles diameter, which in average is on the order of 32 μm. To show the difference between the unsintered and the sintered samples, in Figures 5.21 and 5.22, are reported two SEM images of the two structures, further an EDX study was performed to show how the chemical concentration of the samples would vary, reported in Figures 5.19 and 5.20. In Table 5.5, are reported the quantitative value of the mass % and atom % extrapolated from the EDX machine, from which it is possible to note that around the desired 4% of Zinc is composing the compound. The conductivity study have reported a value of $\sigma = 1.23e^4 S/m$ which is three orders of magnitude lower than the pure magnesium one. This is induced by the fact that the AM MgZn structure is not a bulk material but is composed by several micro-metric molecules connected each other and coated by an oxide layer, creating a porous structure. In fact in Table 5.4 is shown the density difference between the bulk MgZn and the fabricated MgZn, inducing the presence of pores inside the structure.

The HAp coating was relying on the immersion of the biodegradable magnesium structures inside a liquid solutions. It has been shown in Chapter 2.1, that part of the magnesium will be degrading during this study to allow the correct HAp formation, which is possible to notice in Figure 5.25. Some SEM images of the HAp coated BC Mg and AM MgZn structures are reported in Figure 5.28 and 5.27, showing also the difference in coating uniformity. For the BC Mg samples some cracks were present on the HAp and Mg surface showing the bulk material, further the coating was not fully uniform for these samples. Instead for the AM samples a more uniform and quasi full HAp coverage was seen, allowing the detection also of some bigger HAp crystals, Figure 5.26. To demonstrate that the deposited layer was HAp and not another CaP based ceramic, an EDX and an XRD analysis have been performed, showing the correct chemical composition of the material. The XRD in Figure 5.29 was showing peaks on HAp, Mg and $MgOH_2$ which are the main three components reported by [40] and [41]. The EDX in Figure 5.30 showed huge peaks on Ca, P, O and smaller ones on Mg and Zn, in Table 5.5 it is shown the quantitative EDX results. The roughness was more or less constant for both the MgZn samples before and after the HAp coating, as reported in Table 5.6.

For what concerns Zinc Oxide, the Au "Long-gap" devices coated by ZnO NPs are reported in Figure 5.32. An SEM image, Figure 5.31, and an AFM analysis, in Figure 5.33, have been performed to show the layer structure and its surface roughness, reported in Table 5.6. The average thickness of the ZnO NPs deposited layer was on the order of 300 to 400 nm, determined from a Dektak analysis.

Finally, in Figure 5.34 is shown the final DSRR and strain sensing devices coated into or on top of a POMaC substrate.

Electromagnetic studies were performed thanks to the resonating antenna reported in Chapter 5.1, and will be compared to the CST simulations reported in Chapter 5.2.

First the double split ring resonating device will be studied. In Figure 5.3 is reported the simulations results for the classical double split ring resonator shown in Figure 5.2, for two different thicknesses that will be then studied. In Figure 5.36 and 5.38 are reported the resonance frequency of the two manufactured BC and AM DSRR, shown in Figure 5.35. The two resonance frequencies of the two samples, induced by the presence of the double ring, are similar to the simulated results with an overall variation of around 300 MHz. It is possible to note that, as shown also by the simulation, the resonance frequency tend to decrease by increasing the thickness of the device, since an increase of the capacitance will take place.

Then, it was possible to study the sample coated by an HAp layer reported in Figure 5.36, the resonance frequency variation is of the order of 60 to 90 MHz from the uncoated device. This shift, quasi-negligible, could be induced by either the HAp material, which works as a dielectric layer, creating a variation of frequency; by the little degradation that has occurred during the coating process; or by the non perfect alignment of the two structures before and after the coating, gap misalignment or not centering of the two structures, modifying the overall resonance frequency.

Finally there is reported a figure showing the resonance frequency of only the simple split ring resonating structures without inserting one into the other, in Figure 5.39. The resonance frequency would be affected by the over-positioning of the two, but also once the inner layer of the DSRR device would be degraded, only the outer one will remain, inducing a huge f_r shift of around 2 GHz, making easy its detection. This last result, is what is expected to be measured once the device would be inserted into human body, and a pH level of 5.5 or lower gets reached.

Once coated with POMaC, a huge resonance frequency shift was expected thanks to the simulations reported in Figure 5.4, while the final device was showing a more contained shift in frequency, of around 0.8-1.1 GHz to 1.6 GHz form the uncoated device, Figure 5.37.

The one employed for the EM studies have been the golden one since the platinum based structures were too thin, and would have been harder to study the behaviour of the ZnO nanoparticles. The short and the long gap split ring resonators were also simulated in Chapter

5.2.2, from which it was possible to compare the simulation results with the characterized ones shown in Figure 5.40. It is possible to note a shift for the "Short-gap" SRR of around 400MHz and of around 200MHz for the "Long-gap", which could rely on the not perfect shape reproduction since a stencil mask was performed, which would affect the gap distance, the width and the length.

Once ZnO was deposited a shift to higher frequency was induced, opposite to the simulations, but similar to what found in literature. Here it was possible to measure a variation of the resonance frequency value depending on the pH of the solution employed. In Figure 5.41 and 5.42, a shift of around 90 MHz and 30 MHz are recorded once a pH 1.2 solution was casted on top of the resonating device. This very promising result, has to be further tested to be sure about the correct behaviour of the device.

For the strain sensor, a huge variation of frequency was expected from the simulation shown in Figure 5.11, and it was more or less respected once studied the fabricated device behaviour, in Figure 5.44 and 5.46. For the BC sample, the resonance frequency characterized was around 1.5 GHz higher than the simulated one, but it was still possible to see the variation of around 400 MHz from the min to max applied displacement. The most interesting results was obtained for the AM strain sensing device, where even if the inner structure was broken, it was still possible to sense a good variation of 500 MHz from no displacement to max displacement, making it a very promising device.

Finally the DSRR study have been performed under a meat layer, and was possible to see if it was still possible to sense the device once the background was subtracted. From both the simulation, reported in Figure 5.12, and the characterization results, in Figure 5.48, was possible to still notice the resonance behaviour of the DSRR, demonstrating its ability to be detected once positioned under a layer of meat, and possibly in the human body.

For what concerns the biodegradation test it was possible to show how fast the fabricated samples were able to get degrade into human body. From Figure 5.49, it is possible to notice how the additively manufactured samples degraded in less than a week. A day by day study have been also performed, showing that its weight was increasing the first two days, their mechanical strength would drop drastically from day three, allowing their full degradation by the end of day four. The HAp coated samples were able to withstand more immersion time, in fact after four weeks they were still present even though their mass decreased to more or less half of the initial weight. The pure Mg samples were able to withstand more immersion time in PBS, a really slow but steady degradation was present, which instead was still faster than the HAp coated ones. Hence, the coating with hydroxyapatite allowed the samples to withstand a longer immersion time than the pure material, which would reduce the release of bio-products, gas and magnesium ions, that may increase the toxicity of the implant.

Chapter 7

Conclusions

In conclusions a biocompatible, biodegradable and wireless pH and strain sensor have been fabricated in this project. The possible biodegradable materials for bone substitution were discussed and the the choice fell on Magnesium due to its bone-mimic mechanical properties and its osteogenetic effect. To increase its material biocompatibility and biomechanical properties, it has been alloyed with a 4% zinc and additively manufactured for porosity.

Pure Mg and Mg-Zn alloy resonating devices have been blade cut and additively manufactured, respectively. SEM images of the AM structures were shown and their chemical composition was demonstrated through EDX, before and after the sintering process. To show the final device idea, a biodegradable elastomer, POMaC, was synthesized and employed either as a substrate or as a lamination layer for the resonating structures.

Hydroxyapatite was chosen as ion resistive material, since its already present into human bones and due to its intrinsic ability to degrade only when a pH level of 5.5 or lower gets reached. It has been deposited on top of the magnesium based structures through hydrothermal method, and its physical and chemical proeperties were characterized through SEM, XRD and EDX. As ion sensitive material Zinc Oxide nanoparticles were fabricated through spark ablation and deposited on the electron beam evaporated gold resonators' surface, its roughness was shown through SEM images and AFM analysis.

The resonating devices have been also tested under a monostatic horn antenna to check their resonance frequency. First the ion resistive pH sensor was tested, which relied on a concentric double split ring resonator, which in the best case scenario would show a shift of the resonance frequency peak of 2GHz once the inner SRR degraded. A shift of around 50 to 90 MHz proportional to the H-ions binding on the pH sensitive materials was occurring for the second sensing mechanism. Finally, it was also possible to detect a shift of around 0.5 GHz of the resonance frequency peak once a displacement, on the two structures composing the strain device, was applied. In general the devices fabricated where having results similar to those simulated through CST Microwave Studio.

Chapter 8

Future Studies

It has been shown that the fabricated devices worked as expected but there are several optimization that can be employed to improve the results.

Some studies may be performed through cell culture to check the biocompatibility and the degradation rate of magnesium-zinc alloy once coated by HAp.

Some lithographic steps and some CVD or PVD may be employed to perfectly pattern magnesium, which would lead to a better shape reproduction and further lower resonating frequencies inducing a lower adsorption of the human tissues and skin effect. This miniaturization would lead to an higher sensitivity to the number of H^+ ions that may bind on ZnO, allowing a better and more accurate characterization of the shift in frequency dependent on the pH level. This deposition could also be effectuated on top of a biodegradable elastomer, such as POMaC or PGSA, allowing the strain sensing device to be more interdigitated and stuck on top of this material.

Studies may be focused also on the implementation of biodegradable dielectrics in between the gaps of the material, making possible a further shift in resonance frequency hence reducing the absorbance effect of the human tissues of EM waves. Further, to increase the strain sensibility of the designed sensor, a biodegradable piezoelectric material may be used, like strained PLLA or collagen.

Finally, it may be possible to study the behavior of the resonating structures by considering other materials. If other ion resistive materials are employed that degrade at different pH levels than HAp, a "two-switch" method may be employed to detect the actual acidity level of the substrate. For example, it has been shown that PMAH through iCVD have the a direct degradation rate to pH relation, being faster for higher pH levels. Further, other kinds of active ion sensitive materials may be employed which would lead to a more specific study on different kind of ions.

Acknowledgements

I'd like to thank Professor Y. Aslan for his antenna and CST simulations support, Professor J. Zhou and J. Dong for their support in 3ME department and material science and Professor C. Boutry for her constant supervising and sharing of thoughts. A thank also to R. Hendrikx for the XRD analysis, to R. Seijffers for the EDX, P. Sberna and B. Morana for cleanroom tools.

A thanks to all those people met during this master period, for their physical and mental support; to all my N17 group for our great union, our joy and our tears. Now we have finally "scavallato". A thank to SGI, shiny realizations, and to AGEBEO, angels on lane, my other families.

Mattia, Matteo and Davidone deserve some space on their own to describe how impor

My close family and friends during the nice and tough times, were always there to push me in doing better, allowing me to become the person I am now. Mom, Dad, Giandone, Stella and Mayo for their push in pursuing my dreams. Spina and Fraalbz, kings of trap music, helped me to shut my brain off during my most stressful days, best bozos I'd ever had. A huge thank to Filippo, Flavio and Cremers for the tough and the chill times.

A special thank to Silvia, who has supported me during these tough times and gave me the strength to overcome every problem; when thinking about you, thousands of km were like few μm. This thesis is to remind you that you can achieve everything in life, you are my fighter, mit smil. "Con gli occhi negli occhi, deludiamoci insieme".

Finally, I want to thank me for not giving up. I overcame 100% of my worst days.

Bibliography

[1] Reena A. Bhatt and Tamara D. Rozental. «Bone Graft Substitutes». In: *Hand Clinics* 28.4 (2012). New and Emerging Technology in the Treatment of the Upper Extremity, pp. 457–468. ISSN: 0749-0712. DOI: `https://doi.org/10.1016/j.hcl.2012.08.001` (cit. on p. 2).

[2] Landon Pryor et al. «Review of Bone Substitutes». In: *Craniomaxillofacial trauma & reconstruction* 2 (Oct. 2009), pp. 151–60. DOI: `10.1055/s-0029-1224777` (cit. on p. 2).

[3] Jan Geurts, J.J. Chris Arts, and G.H.I.M. Walenkamp. «Bone graft substitutes in active or suspected infection. Contra-indicated or not?» In: *Injury* 42 (2011). Bone Substitutes: A Comprehensive Overview, S82–S86. ISSN: 0020-1383. DOI: `https://doi.org/10.1016/j.injury.2011.06.189` (cit. on p. 2).

[4] Albrektsson T. and Johansson C. «Osteoinduction, osteoconduction and osseointegration». In: *European spine journal : official publication of the European Spine Society, the European Spinal Deformity Society, and the European Section of the Cervical Spine Research Society* 10 Suppl 2 (Nov. 2001), S96–101. DOI: `10.1007/s005860100282` (cit. on p. 2).

[5] Luke Hughes, Charalambos Charalambous, and Ahmed Aljawadi. «Engineering advances in promoting bone union». In: Jan. 2020, pp. 5–18. ISBN: 9780128197127. DOI: `10.1016/B978-0-12-819712-7.00002-4` (cit. on pp. 2, 7).

[6] Gerjon Hannink and J.J. Chris Arts. «Bioresorbability, porosity and mechanical strength of bone substitutes: What is optimal for bone regeneration?» In: *Injury* 42 (2011). Bone Substitutes: A Comprehensive Overview, S22–S25. ISSN: 0020-1383. DOI: `https://doi.org/10.1016/j.injury.2011.06.008` (cit. on p. 3).

[7] Vassilis Karageorgiou and David Kaplan. «Porosity of 3D biomaterial scaffolds and osteogenesis». In: *Biomaterials* 26.27 (2005), pp. 5474–5491. ISSN: 0142-9612. DOI: `https://doi.org/10.1016/j.biomaterials.2005.02.002` (cit. on p. 3).

[8] Valerio Monesi. *Istologia.* Piccin-Nuova Libraria, 2018 (cit. on p. 3).

[9] Vincenzo Campana, Giuseppe Milano, E Pagano, Marta Barba, Claudia Cicione, Giampiero Salonna, Wanda Lattanzi, and Giandomenico Logroscino. «Bone substitutes in orthopaedic surgery: from basic science to clinical practice». In: *Journal of materials science. Materials in medicine* 25 (May 2014). DOI: `10.1007/s10856-014-5240-2` (cit. on pp. 3, 5).

[10] Lu H.B. Wang R.Z Cui F.Z. «Synthesis of nanophase hydroxyapatite/collagen composite». In: *Journal of Materials Science Letters* 14.7 (1995), pp. 490–492 (cit. on p. 5).

[11] A.C. Lawson and Jan Czernuszka. «Production and Characterisation of a Collagen-Calcium Phosphate Composite for Use as a Bone Substitute». In: *MRS Proceedings* 550 (Jan. 2011). DOI: `10.1557/PROC-550-273` (cit. on p. 5).

[12] D. S. METSGER, M. R. RIEGER, and D. W. FOREMAN. In: *Journal of Materials Science: Materials in Medicine* 10.1 (1999), pp. 9–17. DOI: `10.1023/a:1008883809160` (cit. on pp. 5, 15).

[13] V. Sansone, D. Pagani, and M. Melato. «The effects on bone cells of metal ions released from orthopaedic implants. A review». In: *Clinical cases in mineral and bone metabolism : the official journal of the Italian Society of Osteoporosis, Mineral Metabolism, and Skeletal Diseases* 10 (Jan. 2013), pp. 34–40. DOI: `10.11138/ccmbm/2013.10.1.034` (cit. on p. 5).

[14] Mark Staiger, Alexis Pietak, Jerawala Huadmai, and George Dias. «Magnesium and its Alloys as Orthopedic Biomaterials». In: *Biomaterials* 27 (Apr. 2006), pp. 1728–34. DOI: `10.1016/j.biomaterials.2005.10.003` (cit. on pp. 5, 6, 12).

[15] Masahiro Maruyama, Claire Rhee, Takeshi Utsunomiya, Ning Zhang, Masaya Ueno, Zhenyu Yao, and Stuart B. Goodman. «Modulation of the Inflammatory Response and Bone Healing». In: *Frontiers in Endocrinology* 11 (2020). ISSN: 1664-2392. DOI: `10.3389/fendo.2020.00386`. URL: `https://www.frontiersin.org/articles/10.3389/fendo.2020.00386` (cit. on pp. 6, 8).

[16] Kristiina Rajamäki, Tommy Nordström, Katariina Nurmi, Karl Akerman, Petri Kovanen, Katariina Oörni, and Kari Eklund. «Extracellular Acidosis Is a Novel Danger Signal Alerting Innate Immunity via the NLRP3 Inflammasome». In: *The Journal of biological chemistry* 288 (Mar. 2013). DOI: `10.1074/jbc.M112.426254` (cit. on pp. 6, 7).

[17] Fernando Erra Díaz, Ezequiel Dantas, and Jorge Geffner. «Unravelling the Interplay between Extracellular Acidosis and Immune Cells». In: *Mediators of Inflammation* 2018 (2018) (cit. on p. 7).

[18] Chelsea Bahney, Robert Zondervan, Patrick Allison, Alekos Theologis, Jason Ashley, Jaimo Ahn, Theodore Miclau, Ralph Marcucio, and Kurt Hankenson. «The Cellular Biology of Fracture Healing». In: *Journal of Orthopaedic Research* 37 (Oct. 2018). DOI: `10.1002/jor.24170` (cit. on p. 7).

[19] S. Halvachizadeh and H. C. Pape. «Perren's Strain Theory and Fracture Healing». In: *Essential Biomechanics for Orthopedic Trauma: A Case-Based Guide*. Ed. by B. D. Crist, J. Borrelli Jr., and E. J. Harvey. Cham: Springer International Publishing, 2020, pp. 17–25. DOI: `10.1007/978-3-030-36990-3_2` (cit. on p. 9).

[20] Reiner Hente, Bernd Füchtmeier, U Schlegel, Antonio Ernstberger, and Stephan Perren. «The influence of cyclic compression and distraction on the healing of experimental tibial fractures». In: *Journal of orthopaedic research : official publication of the Orthopaedic Research Society* 22 (July 2004), pp. 709–15. DOI: `10.1016/j.orthres.2003.11.007` (cit. on p. 9).

[21] Melissa Tsang, Andac Armutlulu, Adam Martinez, Sue Allen, and Mark Allen. «Biodegradable magnesium/iron batteries with polycaprolactone encapsulation: A microfabricated power source for transient implantable devices». In: *Microsystems & Nanoengineering* 1 (Oct. 2015), p. 15024. DOI: `10.1038/micronano.2015.24` (cit. on p. 11).

[22] Suk-Won Hwang et al. «Biodegradable Elastomers and Silicon Nanomembranes/Nanoribbons for Stretchable, Transient Electronics, and Biosensors». In: *Nano letters* 15 (Feb. 2015). DOI: `10.1021/nl503997m` (cit. on p. 11).

[23] Yang Liu et al. «Fundamental Theory of Biodegradable Metals—Definition, Criteria, and Design». In: *Advanced Functional Materials* 29 (18 May 2019). ISSN: 16163028. DOI: `10.1002/ADFM.201805402` (cit. on pp. 11, 12).

[24] C. Hung, A. Chaya, K. L., K. Verdelis, and C. Sfeir. «The role of magnesium ions in bone regeneration involves the canonical Wnt signaling pathway». In: *Acta Biomaterialia* 98 (2019). 10th BIOMETAL2018 - International Symposium on Biodegradable Metals, pp. 246–255. ISSN: 1742-7061. DOI: `https://doi.org/10.1016/j.actbio.2019.06.001` (cit. on p. 12).

[25] D. Noviana, D. Paramitha, M.F. Ulum, and H. Hermawan. «The effect of hydrogen gas evolution of magnesium implant on the postimplantation mortality of rats». In: *Journal of Orthopaedic Translation* 5 (2016). Special Issue: Orthopaedic Biomaterials and Devices, pp. 9–15. ISSN: 2214-031X. DOI: `https://doi.org/10.1016/j.jot.2015.08.003` (cit. on p. 12).

[26] Y.F. Zheng, X.N. Gu, and F. Witte. «Biodegradable metals». In: *Materials Science and Engineering: R: Reports* 77 (2014), pp. 1–34. ISSN: 0927-796X. DOI: `https://doi.org/10.1016/j.mser.2014.01.001` (cit. on pp. 12, 13).

[27] J. Venezuela and M.S. Dargusch. «The influence of alloying and fabrication techniques on the mechanical properties, biodegradability and biocompatibility of zinc: A comprehensive review». In: *Acta Biomaterialia* 87 (2019), pp. 1–40. ISSN: 1742-7061. DOI: `https://doi.org/10.1016/j.actbio.2019.01.035` (cit. on p. 12).

[28] Catarina Fernandes and Irene Taurino. «Biodegradable Molybdenum (Mo) and Tungsten (W) Devices: One Step Closer towards Fully-Transient Biomedical Implants». In: *Sensors* 22 (Apr. 2022), p. 3062. DOI: `10.3390/s22083062` (cit. on p. 12).

[29] AZO Materials. «Density of Elements Chart». In: (). URL: `www.azom.com` (cit. on p. 12).

[30] J. Dong et al. «Extrusion-based 3D printed magnesium scaffolds with multifunctional MgF 2 and MgF 2 -CaP coatings». In: *Biomaterials Science* 9 (Sept. 2021). DOI: `10.1039/D1BM01238J` (cit. on pp. 13, 14, 55).

[31] J. Dong, N. Tümer, M.A. Leeflang, P. Taheri, L.E. Fratila-Apachitei, J.M.C. Mol, A.A. Zadpoor, and J. Zhou. «Extrusion-based additive manufacturing of Mg-Zn alloy scaffolds». In: *Journal of Magnesium and Alloys* (2021). ISSN: 2213-9567. DOI: `https://doi.org/10.1016/j.jma.2021.11.018` (cit. on p. 14).

[32] Y. Zhong, P. Godwin, Y. Jin, and H. Xiao. «Biodegradable polymers and green-based antimicrobial packaging materials: A mini-review». In: *Advanced Industrial and Engineering Polymer Research* 3.1 (2020), pp. 27–35. ISSN: 2542-5048. DOI: `https://doi.org/10.1016/j.aiepr.2019.11.002` (cit. on p. 14).

[33] Fatemeh Asghari, Mohammad Samiei, Khosro Adibkia, Abolfazl Akbarzadeh, and Soodabeh Davaran. «Biodegradable and biocompatible polymers for tissue engineering application: a review». In: *Artificial Cells, Nanomedicine, and Biotechnology* 45.2 (2017). PMID: 26923861, pp. 185–192. DOI: `10.3109/21691401.2016.1146731` (cit. on p. 14).

[34] K Van de Velde and P Kiekens. «Biopolymers: overview of several properties and consequences on their applications». In: *Polymer Testing* 21.4 (2002), pp. 433–442. ISSN: 0142-9418. DOI: `https://doi.org/10.1016/S0142-9418(01)00107-6` (cit. on p. 14).

[35] Lena Vogt, Florian Ruther, Sahar Salehi, and Aldo Boccaccini. «Poly(Glycerol Sebacate) in Biomedical Applications—A Review of the Recent Literature». In: *Advanced Healthcare Materials* 10 (Mar. 2021). DOI: `10.1002/adhm.202002026` (cit. on p. 14).

[36] R. T. Tran, P. Thevenot, D. Gyawali, J.C. Chiao, L. Tang, and J. Yang. «Synthesis and characterization of a biodegradable elastomer featuring a dual crosslinking mechanism». In: *Soft Matter* 6.11 (Jan. 2010), p. 2449. DOI: `10.1039/c001605e` (cit. on pp. 14, 58).

[37] X. Shi, Y. Ye, H. Wang, F. Liu, and Z. Wang. «Designing pH-Responsive Biodegradable Polymer Coatings for Controlled Drug Release via Vapor-Based Route». In: *ACS Applied Materials & Interfaces* 10 (2018). DOI: `10.1021/acsami.8b14016` (cit. on p. 14).

[38] R Z LEGEROS and J P LEGEROS. «16 - Hydroxyapatite». In: *Bioceramics and their Clinical Applications*. Ed. by Tadashi Kokubo. Woodhead Publishing Series in Biomaterials. Woodhead Publishing, 2008, pp. 367–394. ISBN: 978-1-84569-204-9. DOI: `https://doi.org/10.1533/9781845694227.2.367` (cit. on p. 15).

[39] Liana Maria Muresan. «Chapter 17 - Corrosion Protective Coatings for Ti and Ti Alloys Used for Biomedical Implants». In: *Intelligent Coatings for Corrosion Control*. Ed. by Atul Tiwari, James Rawlins, and Lloyd H. Hihara. Boston: Butterworth-Heinemann, 2015, pp. 585–602. ISBN: 978-0-12-411467-8 (cit. on p. 15).

[40] Masanari Tomozawa and Sachiko Hiromoto. «Growth mechanism of hydroxyapatite-coatings formed on pure magnesium and corrosion behavior of the coated magnesium». In: *Applied Surface Science* 257.19 (2011). E-MRS2010 Fall Meeting Symposium F: "10th International Symposium on Electrochemical/Chemical Reactivity of Metastable Materials", pp. 8253–8257. ISSN: 0169-4332. DOI: `https://doi.org/10.1016/j.apsusc.2011.04.087` (cit. on pp. 15, 90).

[41] Sachiko Hiromoto and Masanari Tomozawa. «Hydroxyapatite coating of AZ31 magnesium alloy by a solution treatment and its corrosion behavior in NaCl solution». In: *Surface and Coatings Technology* 205.19 (2011), pp. 4711–4719. ISSN: 0257-8972. DOI: `https://doi.org/10.1016/j.surfcoat.2011.04.036` (cit. on pp. 15, 55, 90).

[42] S. Makarychev-Mikhailov, A. S., and Eric Bakker. «CHAPTER 4 - New trends in ion-selective electrodes». In: *Electrochemical Sensors, Biosensors and their Biomedical Applications*. San Diego: Academic Press, 2008, pp. 71–114. ISBN: 978-0-12-373738-0. DOI: `https://doi.org/10.1016/B978-012373738-0.50006-4` (cit. on p. 16).

[43] K. Štulík. «ION-SELECTIVE ELECTRODES | Overview». In: *Encyclopedia of Analytical Science (Second Edition)*. Ed. by P. Worsfold, A. Townshend, and C. Poole. Second Edition. Oxford: Elsevier, 2005, pp. 493–498. ISBN: 978-0-12-369397-6. DOI: `https://doi.org/10.1016/B0-12-369397-7/00291-0` (cit. on p. 16).

[44] G. Orellana, C. Cano-Raya, J. López-Gejo, and A.R. Santos. «3.10 - Online Monitoring Sensors». In: *Treatise on Water Science*. Ed. by Peter Wilderer. Oxford: Elsevier, 2011, pp. 221–261. ISBN: 978-0-444-53199-5. DOI: `https://doi.org/10.1016/B978-0-444-53199-5.00059-2` (cit. on p. 16).

[45] P. Kielbik, J. Kaszewski, J. Rosowska, E. Wolska, B. S. Witkowski, M. A. Gralak, Z. Gajewski, M. Godlewski, and M. M. Godlewski. «Biodegradation of the ZnO:Eu nanoparticles in the tissues of adult mouse after alimentary application». In: *Nanomedicine: Nanotechnology, Biology and Medicine* 13.3 (2017), pp. 843–852. ISSN: 1549-9634. DOI: `https://doi.org/10.1016/j.nano.2016.11.002` (cit. on p. 16).

[46] P. Kielbik et al. «Preliminary Studies on Biodegradable Zinc Oxide Nanoparticles Doped with Fe as a Potential Form of Iron Delivery to the Living Organism». In: *Nanoscale Research Letters* 14 (Dec. 2019). DOI: `10.1186/s11671-019-3217-2` (cit. on p. 16).

[47] Jialin Li, Tingke Rao, Wugang Liao, Jie Jiang, Peng Yang, and Juin Liou. «Extended-gate Field Effect Transistors with Zinc Oxide as sensing film for pH Sensing». In: July 2021, pp. 1–3. DOI: `10.1109/ISNE48910.2021.9493628` (cit. on p. 16).

[48] T. Reinecke, J.-G. Walter, T. Kobelt, A. Ahrens, T. Scheper, and S. Zimmermann. «Design and evaluation of split-ring resonators for aptamer-based biosensors». In: *Journal of Sensors and Sensor Systems* 7.1 (2018), pp. 101–111. DOI: `10.5194/jsss-7-101-2018`. URL: `https://jsss.copernicus.org/articles/7/101/2018/` (cit. on p. 18).

[49] Md Shamsul Arefin, M Coskun, Tuncay Alan, Adrian Neild, Jean-Michel Redoute, and Mehmet Yuce. «A MEMS Capacitive pH Sensor for High Acidic and Basic Solutions». In: vol. 2014. Nov. 2014. DOI: `10.1109/ICSENS.2014.6985373` (cit. on pp. 18, 19).

[50] K. Hori, A. Inami, T. Kan, and H. Onoe. «Split-Ring-Shaped Biodegradable pH Sensor for Wireless and Battery-Free Monitoring of Agricultural Fields». In: *2021 21st International Conference on Solid-State Sensors, Actuators and Microsystems*. 2021, pp. 863–866. DOI: `10.1109/Transducers50396.2021.9495592` (cit. on pp. 19, 20, 38, 55).

[51] Clémentine M. Boutry, Hengky Chandrahalim, Patrick Streit, Michael Schinhammer, Anja C. Hänzi, and Christofer Hierold. «Characterization of miniaturized RLC resonators made of biodegradable materials for wireless implant applications». In: *Sensors and Actuators A: Physical* 189 (2013), pp. 344–355. ISSN: 0924-4247. DOI: `https://doi.org/10.1016/j.sna.2012.08.039` (cit. on p. 19).

[52] Hanbin Liu et al. «Flexible, Degradable, and Cost-Effective Strain Sensor Fabricated by a Scalable Papermaking Procedure». In: *ACS Sustainable Chemistry & Engineering* 6.11 (2018), pp. 15749–15755. DOI: `10.1021/acssuschemeng.8b04298` (cit. on p. 20).

[53] Z. Liu et al. «Biodegradable Polyurethane Fiber-Based Strain Sensor with a Broad Sensing Range and High Sensitivity for Human Motion Monitoring». In: *ACS Sustainable Chemistry & Engineering* 10.27 (2022), pp. 8788–8798. DOI: `10.1021/acssuschemeng.2c01171` (cit. on pp. 20, 21).

[54] S. Zhang, H. Li, Z. Yang, B. Chen, K. Li, X. Lai, and X. Zeng. «Degradable and stretchable bio-based strain sensor for human motion detection». In: *Journal of Colloid and Interface Science* 626 (2022), pp. 554–563. ISSN: 0021-9797. DOI: `https://doi.org/10.1016/j.jcis.2022.06.171` (cit. on pp. 20, 21).

[55] Clementine Boutry, Yukitoshi Kaizawa, Bob Schroeder, Alex Chortos, Anais Legrand, Zhen Wang, James Chang, Paige Fox, and Zhenan Bao. «A stretchable and biodegradable strain and pressure sensor for orthopaedic application». In: *Nature Electronics* 1 (May 2018). DOI: `10.1038/s41928-018-0071-7` (cit. on p. 21).

[56] Rohat Melik, Emre Unal, Nihan Perkgoz, Brandon Santoni, Debra Kamstock, Christian Puttlitz, and Hilmi Demir. «Nested Metamaterials for Wireless Strain Sensing». In: *Selected Topics in Quantum Electronics, IEEE Journal of* 16 (May 2010), pp. 450–458. DOI: `10.1109/JSTQE.2009.2033391` (cit. on p. 22).

[57] Meipu Li, Helei Dong, Ya Wang, Xiawen Yan, Zhuya Hao, and Qiulin Tan. «Wireless Passive Flexible Strain Sensor Based on Aluminium Nitride Film». In: *IEEE Sensors Journal* PP (Dec. 2021), pp. 1–1. DOI: `10.1109/JSEN.2021.3138786` (cit. on p. 23).

[58] J.D. Kraus. *Antennas*. Electrical engineering series. McGraw-Hill, 1988. ISBN: 9780071004824 (cit. on p. 24).

[59] Constantine A Balanis. *Antenna theory: analysis and design*. Wiley-Interscience, 2005 (cit. on pp. 24, 27, 28).

[60] Y. Rahmat-Samii, L.I. Williams, and R.G. Yaccarino. «The UCLA bi-polar planar-near-field antenna-measurement and diagnostics range». In: *IEEE Antennas and Propagation Magazine* 37.6 (1995), pp. 16–35. DOI: `10.1109/74.482029` (cit. on p. 25).

[61] UNC-Charlotte University Kathryn Leigh Smith. «Lectures on electromagnetic waves». In: () (cit. on p. 26).

[62] Safa Kasap. «Optoelectronics and Photonics : Principles and Practices / S.O. Kasap.» In: (Jan. 2013) (cit. on p. 26).

[63] A. Paraboni. *Antenne*. Collana di istruzione scientifica: Serie di elettronica. McGraw-Hill Companies, 1999. ISBN: 9788838608100 (cit. on p. 26).

[64] Universitat Politècnica de Catalunya (UPC) Juan Manuel Rius. «Lectures on radar cross section». In: () (cit. on p. 28).

[65] Niu Liqiang, Yongjun Xie, Peiyu Wu, and Chungang Zhang. «ARCS: Active Radar Cross Section for Multi-Radiator Problems in Complex EM Environments». In: *Sensors* 20 (June 2020), p. 3371. DOI: `10.3390/s20123371` (cit. on p. 29).

[66] D.M. Pozar. *Microwave Engineering, 4th Edition*. Wiley, 2011. ISBN: 9781118213636 (cit. on p. 30).

[67] F.W. Grover. *Inductance Calculations: Working Formulas and Tables*. Dover phoenix editions. Dover Publications, 2004. ISBN: 9780486495774 (cit. on pp. 33, 35).

[68] Andrea Vallecchi, Ekaterina Shamonina, and Christopher J. Stevens. «Analytical model of the fundamental mode of 3D square split ring resonators». In: *Journal of Applied Physics* 125.1 (2019), p. 014901. DOI: `10.1063/1.5053482`. eprint: `https://doi.org/10.1063/1.5053482` (cit. on p. 33).

[69] Oleksiy Sydoruk, E. Tatartschuk, E. Shamonina, and Laszlo Solymar. «Analytical formulation for the resonant frequency of split rings». In: *Journal of Applied Physics* 105 (Feb. 2009), pp. 014903–014903. DOI: `10.1063/1.3056052` (cit. on p. 34).

[70] J. D. Jackson. «Charge density on thin straight wire, revisited». In: *American Journal of Physics* 68.9 (2000), pp. 789–799. DOI: `10.1119/1.1302908`. eprint: `https://doi.org/10.1119/1.1302908` (cit. on p. 34).

[71] Bruno Sauviac, Constantin Simovski, and SA Tretyakov. «Double Split-Ring Resonators: Analytical Modeling and Numerical Simulations». In: *Electromagnetics* 24 (July 2004), pp. 317–338. DOI: `10.1080/02726340490457890` (cit. on p. 35).

[72] Fred Gardiol. *Traité d'électricité, volume 3 : Electromagnétisme*. Dunod Université, France, 1987 (cit. on p. 35).

[73] Y. T. Lo and S. W. Lee. *Antenna handbook: Theory, applications, and design.* New York: 405 Van Nostrand Reinold Co., Chap. 7., 1988 (cit. on p. 36).

[74] R. W. P. King. *The loop antenna for transmission and reception.* Antenna theory, Part 1, ed. R. E. Collin and F. J. Zucker. New York: McGraw Hill, 1969 (cit. on p. 36).

[75] journal=Journal of Biomedical Engineering and Technology volume=2 number=3 pages=29–33 year=2014 doi=10.12691/jbet-2-3-1 publisher=Science and Education Publishing Mohammed, Yessar E. and Saber, Ali G. title=Estimation of E-Field inside Muscle Tissue at MICS and ISM Frequencies Using Analytic and Numerical Methods. In: () (cit. on p. 41).

[76] EMF-PORTAL. «Radio frequency (10 MHz–300 GHz)». In: (). URL: `https://www.emf-portal.org/en/cms/page/home/effects/radio-frequency` (cit. on p. 41).

[77] Silhouette America. «Silhouette Cameo 4 Blade Cutter». In: (). URL: `www.silhouetteamerica.com` (cit. on p. 46).

[78] Yoon Lee, Jeonghyun Kim, Yerim Kim, Jean Kwak, Younghee Yoon, and John Rogers. «Room Temperature Electrochemical Sintering of Zn Microparticles and Its Use in Printable Conducting Inks for Bioresorbable Electronics». In: *Advanced Materials* 29 (Aug. 2017), p. 1702665. DOI: `10.1002/adma.201702665` (cit. on p. 49).

[79] Analytik.co.uk. «BIOSCAFFOLDER 3D BIOPRINTER SERIES». In: (). URL: `https://analytik.co.uk/product/3d-bioprinter-bioscaffolder/` (cit. on p. 51).

[80] Anuj Kumar, Saeid Kargozar, Francesco Baino, and Sung Soo Han. «Additive Manufacturing Methods for Producing Hydroxyapatite and Hydroxyapatite-Based Composite Scaffolds: A Review». In: *Frontiers in Materials* 6 (Dec. 2019), p. 313. DOI: `10.3389/fmats.2019.00313` (cit. on p. 51).

[81] T.V. Pfeiffer, J. Feng, and A. Schmidt-Ott. «New developments in spark production of nanoparticles». In: *Advanced Powder Technology* 25.1 (2014), pp. 56–70. ISSN: 0921-8831. DOI: `https://doi.org/10.1016/j.apt.2013.12.005` (cit. on p. 57).

[82] Boyang Zhang et al. «Biodegradable scaffold with built-in vasculature for organ-on-a-chip engineering and direct surgical anastomosis». In: *Nature materials* 4 (Mar. 2016). DOI: `10.1038/nmat4570` (cit. on p. 58).

[83] Sahitya Vegesna, Heidemarie Schmidt, Ilona Skorupa, Danilo Buerger, Oliver Schmidt, Jan Dellith, and Vinayak Bhat. «Increased static dielectric constant in ZnMnO and ZnCoO thin films with bound magnetic polarons». In: *Scientific Reports* 10 (Apr. 2020). DOI: `10.1038/s41598-020-63195-1` (cit. on p. 63).

[84] F E Hizir, Hussain M. Al-Qahtani, and David E. Hardt. «Deformation of Stamp Features with Slanted Walls During Microcontact Printing». In: 2014 (cit. on p. 65).